LANCASTER UNIVERSITY

SCHOOL OF ENGINEERING

Defect chemistry of bulk and nanoscale PuO_2

Author:
William D. Neilson

Supervisor:
Dr. Samuel T. Murphy

A thesis submitted for the degree of Doctor of Philosophy

November 2022

Abstract

The management of large stockpiles of Pu, separated from spent nuclear fuel or nuclear weapons programmes and stored as the oxide PuO_2, requires an understanding of the material's aging behaviour during interim storage. This includes characterising the effect of radiogenic impurities that accumulate at significant concentration over storage time periods, as well as insight into the segregation of both radiogenic and non-radiogenic species between accommodation as defects in the oxide powder or in the storage container headspace above it.

Point defects play a crucial role in the properties of crystalline materials. Modern first principles atomistic simulation techniques, such as density functional theory (DFT), are now widely employed for the simulation of point defects of both intrinsic and extrinsic origin. However, it is only through the careful use of thermodynamics that the defect energies obtained in these simulations can be exploited to provide a realistic description of a system under specific operating conditions, such as those present in PuO_2 storage containers.

This thesis has developed the Defect Analysis Package (DefAP), an open-source Python code that is designed to combine DFT data with established thermodynamic relationships to provide new insight into the defect chemistry of materials. Aided by DefAP, PuO_2 under interim storage conditions has been studied.

The results show that the intrinsic defect chemistry of $PuO_{2\pm x}$ is dominated by oxygen vacancies and interstitials and that PuO_{2+x} is thermodynamically very unfavourable. Radiogenic Am occupies Pu sites in $(Pu,Am)O_{2\pm x}$ with an evolving ratio of the +III and +IV oxidation states, dependent upon temperature, oxygen partial pressure, and the concentration of the Am itself. It is observed that even small concentrations of Am(III) impact significantly on the material's properties: it promotes a reducing environment and acts as a p-type dopant, elevating the concentration of holes in the valence band leading to increased electrical susceptibility and a postulated increase in surface reactivity. He from alpha-decay was found to be preferentially accommodated in $PuO_{2\pm x}$ on the interstitial site, but that the impact of Am is large enough to, under certain conditions, alter this accommodation mechanism to an oxygen vacancy. The reproduction of the available experimental data lends confidence to the model's accuracy.

In the final part of the thesis, it is explored whether simulations of nanoparticles — instead of the bulk material — may offer a better representation of the stored PuO_2 powder. Whilst the simulated nanoparticles display many bulk-like features, it was seen that unique characteristics are present as a consequence of the under-coordinated atoms located at the particle's surface. Surface configurations promoting reduced Pu or oxidised O ions have been observed and with thermodynamic relationships the environmental conditions where these differing surface configurations become favourable were predicted.

The improved scientific understanding of PuO_2 presented in the thesis is essential information in the long-term move towards its storage and will inform future disposition programmes. An improved understanding also has the potential to reduce some of the pessimisms built into stores' safety cases.

Declaration

The work presented in this thesis is my own and all else is appropriately referenced. It has not been submitted in support of an application for another degree at this or any other University. Chapters containing published work are clearly identified.

Acknowledgments

I am extremely grateful to my PhD supervisor, Dr Samuel Murphy, for his excellent mentorship as well as the encouragement and support for my future career.

I am thankful to Dr Helen Steele, my industrial supervisor, for her expertise and support for the duration of the PhD that I have valued greatly.

A special thanks to Dr James Pegg for his collaboration early on that catalysed this PhD.

A huge thank you to my friends and colleagues in the Murphy Materials Modelling Group — I've enjoyed working together and especially thank you for making our overseas group trip a highlight.

This thesis has used the High End Computing facility at Lancaster University. I am grateful to Mike Pacey for his technical support.

Lastly, I thank my friends and family for their years of unwavering support.

This PhD was funded as part of EPSRCs TRANSCEND project.

Contents

List of Figures

List of Tables

Chapter 1

Introduction

The element plutonium (Pu) lies at the heart of the nuclear fuel cycle owing to its production in nuclear reactors. Pu isotopes are produced when uranium (U) atoms — predominantly U-238 — capture neutrons, with the quantity produced dependent on factors including the reactor type, the fuel enrichment, and the burn up [1]. The first reactors to operate in the UK were designed with the primary purpose of producing weapons grade Pu [2]; the Calder Hall Magnox reactor and its sister plant at Chapelcross were the first to serve a dual commercial and military purpose. Reactors developed in later years improved the thermodynamic efficiency in order to focus on supplying electricity, containing smaller but still significant quantities of Pu in the spent nuclear fuel.

The outcome of the spent nuclear fuel is subject to intense debate and difficult decision making, with policies varying across the globe. Policy making on spent nuclear fuel involves complex factors for governments to consider, including the inter-generational impact, and the huge capital cost of infrastructure projects that usually accompany such decisions. Strategies must also account for proliferation concerns, fluctuations in the price of U, and public opinion. In simple terms, there are two main options for spent nuclear fuel. The first is to reprocess the fuel, recovering and recycling the usable portion, or alternatively, the long-term storage of the unprocessed spent fuel with eventual final disposal.

Naturally, the reprocessing and recycling of the spent nuclear fuel is an attractive option as it treats the spent nuclear fuel as a potential economic asset and reduces the total volume of waste (reprocessing results in a 75% reduction in the volume of high level waste (HLW) [1]). Reprocessing can be summarised as the chemical separation of the Pu, U, and additional radioactive waste from the spent nuclear fuel. In reprocessing operations, fuel elements are disassembled in the head-end before a series of dissolution, separation, and purification steps in the process-area.

In the UK, the reprocessing of nuclear fuels was a central policy and commitment for many decades although reprocessing will shortly come to an end after 50 years of operations at Sellafield, Cumbria [3]. For the first fleet of nuclear reactors in the UK, the Magnox design, the fuel type demanded reprocessing. This was as a consequence of the decision to store Magnox fuels in wet storage that meant the fuels metallic cladding would corrode [2]. Later, the oxide fuels used by the next generation of reactors used in the UK were reprocessed in the purpose-built Thermal Oxide Reprocessing Plant (ThORP), which also served to reprocess spent nuclear fuels from foreign customers. Reprocessing presented commercial opportunities and offered Britain a place in global fuel cycle with motivation to compete with France, a country heading towards commanding position in the worldwide fuel cycle in the 1980s [4]. A belief that large quantities of Pu would be required for fast-breeder reactors (FBR), expected by many scientists to become the dominant reactor by the end of the 20th century, also served as strong justification to pursue reprocessing [5].

The FBR revolution never materialised, and the UK cancelled its own development programme in 1994 [6]. With reprocessing well underway, the Pu stockpile continued to expand. At the end of reprocessing operations, which are soon to conclude, the UK is forecast to possess a Pu stockpile of 140 tons, of which 23 tons is foreign-owned [7, 8]. The UK government, working with the Nuclear Decommissioning Authority (NDA), has shortlisted two options for the fate of the separated Pu: it should either be reused as Mixed Oxide Fuel (MOX) in nuclear reactors, followed by disposal in a geological disposal facility (GDF), or alternatively, immobilised, followed by disposal in a GDF. The current preferred policy of the UK government is to re-use Pu as fuel in nuclear reactors, only immobilising and disposing the Pu that is unsuitable for conversion to MOX fuel [3]. A new MOX fuel fabrication facility, which blends Pu and U oxides, would be necessary to pursue this strategy. Worldwide, six fabrication facilities have at one time operated, by far the most successful being the MELOX facility in France with an average annual production of 125 tons of heavy metal manufactured between 2014 and 2017 [9]. Research is still required to ensure that the new facility is compatible with the characteristics presented by the UK Pu. MOX fuel has successfully powered commercial light water reactors (LWRs) in France and Japan [10], however suitable reactors would need to be constructed in the UK as well as agreements from operators to use the fuel. The alternative option (immobilisation and disposal) also requires research and development and a GDF will not be available for at least several decades [3]. It can be therefore said that irrespective of the decision to reuse or immobilise, the separated plutonium will require several decades of continued, interim storage.

At Sellafield, separated Pu is stored as calcined PuO_2 powder contained within a series of nested canisters. It is imperative that engineers and scientists can be confident in the procedures in place used to store PuO_2; an improved knowledge of the chemistry and aging characteristic of PuO_2 is of importance to build long-term storage safety cases. One of the most serious fault scenarios that requires an improved scientific understanding is the pressurisation of a storage canister caused by the stored material generating gas — this has been observed in a selection of canisters.

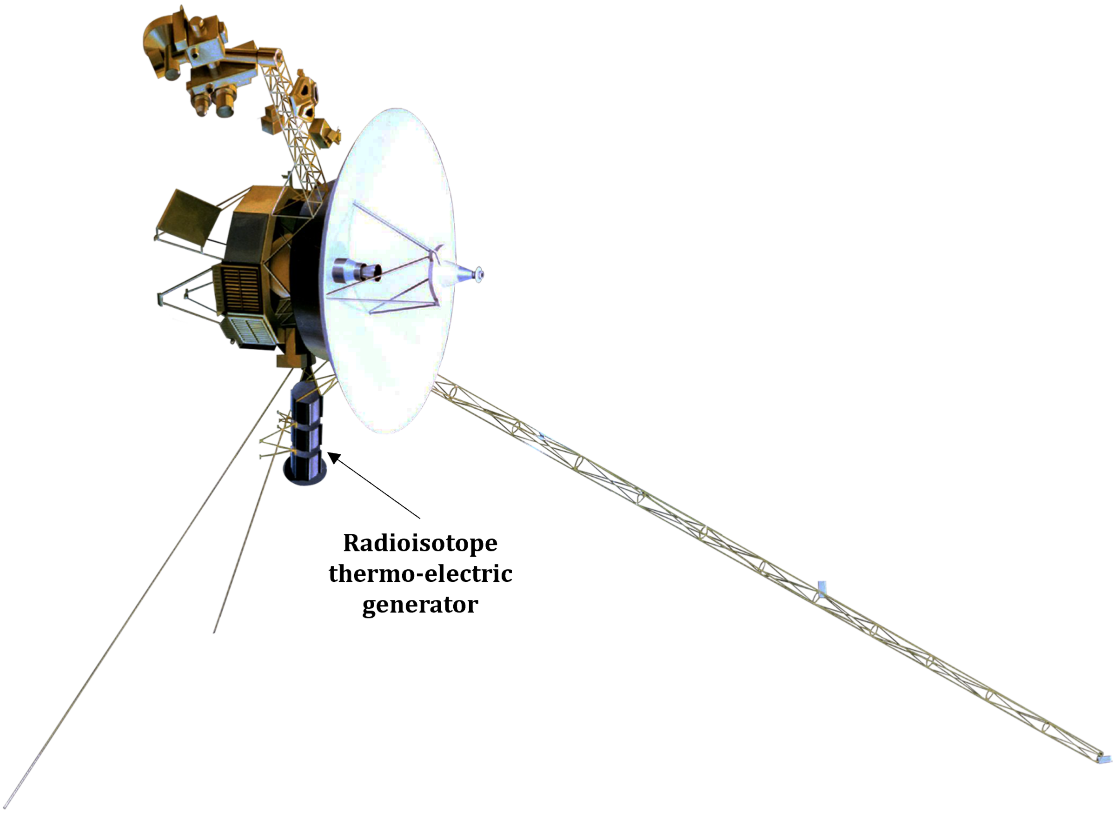

Figure 1.1: Artist's rendering, from NASA, of the design employed by the twin Voyager 1 and Voyager 2 spacecraft.

Outside of the nuclear fuel cycle, a practical, albeit small-scale use of PuO_2 is as the fuel source of radioisotope heating units (RHUs) and radioisotope thermo-electric generators (RTGs). $^{238}PuO_2$ is the most commonly used isotope in RTGs and RHUs for space applications [11]. The absorption of the decay products from the alpha decay of ^{238}Pu produces heat that can be used to generate electricity. RTGs are extremely reliable, compact, and lightweight devices: three very favourable traits for a spacecraft. The most distant man-made object is the Voyager 1 space probe, launched in 1977 and powered by a $^{238}PuO_2$ RTG. As of July 31, 2022 the probe has reached a distance of 156.61 AU (23.429 billion km; 14.558 billion mi) from Earth . The RTGs have powered Voyager 1 and its twin, Voyager 2, for 45 years, but with the power output decreasing by about four watts a year the slow shutdown of the spacecrafts' systems will finally culminate in the coming years [12].

Whether in a deep underground GDF, or in interstellar space, PuO_2 will, like all crystalline materials, contain imperfections that have the ability to modify the properties of the material. A “defect” can be considered to be any localised disruption to the perfect crystal lattice and are typically categorised according to their dimensionality, i.e. point defects (0D), dislocations (1D), surfaces/grain boundaries (2D) and bubbles/voids (3D). Despite their small size, point defects play a crucial role in the properties of PuO_2; this includes the electrical conductivity, oxygen potential, oxygen diffusion, heat capacity and thermal conductivity. Point defects also play a crucial role in the incorporation of radiogenic species. The incorporation of foreign atoms into a material can produce dramatic changes to a material’s characteristics. Americium (Am) is likely to make a considerable impact: it is produced by ^{241}Pu decaying into ^{241}Am and accumulates quickly due to the short half life of ^{241}Pu (14.4 years).

The dramatic increase in computational processing power together with the development of sophisticated algorithms and programs allows for the investigation of material chemistry with computational simulation. This is of particular help and importance in the study of PuO_2 due to the experimental challenges that include strict regulation, the difficulty in preparing and handling samples, and the continuous crystal lattice damage and transmutation of Pu due to self-irradiation [13].

PuO_2 can be studied by harnessing the power of density functional theory (DFT). DFT is a quantum mechanical (or *ab initio*) technique that can be applied to solving the Schrödinger equation that describes the quantum behaviour of atoms and molecules. DFT is built around (and takes its name from) the theorems of Hohenberg and Kohn [14], the first of which proved that: *The ground-state energy from Schrödinger’s equation is a unique functional of the electron density*. PuO_2 is a crystalline material, meaning that it arranges its atoms in a periodic array of identical structural units, or unit cells. It is this symmetry that is exploited when studying crystalline solids with DFT; it would be infeasible to study the electronic structure of a system with no underlying symmetry (e.g. an amorphous solid). DFT has become a phenomenally successful approach used by huge numbers of researchers across many disciplines [15]. Calculations are recognised as a highly accurate and often predictive [15, 16].

Using DFT, complementary atomistic simulation techniques, and purpose-built thermodynamic post-processing tools, this thesis aims to provide new insight into the properties and aging characteristics of PuO_2. By studying the material's point defect chemistry, the mechanisms of non-stoichiometry ($PuO_{2\pm x}$), as well as the ingrowth and impact of radiogenic species can be predicted. The defect analysis tools built to study PuO_2 will be general-purpose and open-source, enabling the analysis of point defects in a wide array of crystalline solids.

The results presented in this thesis can be split into three categories:

(i) In Chapter 3 a program is designed to facilitate the defect chemistry of crystalline materials to be explored. This chapter serves as the methodology section of this thesis.

(ii) Chapters 4, 5 & 6 employ the program to investigate the defect chemistry of bulk PuO_2, considering both intrinsic and radiogenic defects.

(iii) In Chapter 7 a theoretical analysis of the properties of PuO_2 nanoparticles is performed, providing new insight on the characteristics of PuO_2 possessing a high surface to volume ratio.

Chapter 2

Literature review

2.1 Plutonium

Element number 94 in the periodic table was named in 1942 for Pluto — the dwarf-planet that, until 2006, was classified as a planet — following its isolation a year earlier by Seaborg, Kennedy, and Wahl at the University of California, Berkeley. The momentous achievement was quickly taken advantage of; it was to set into motion the Manhattan Project — which was to deliver the first nuclear weapons — and, at the conclusion of the war, the Atomic Age in which atomic power was developed and harnessed.

In the U-based nuclear reactors that vastly dominate the entire history of the nuclear power market, five Pu isotopes are present in spent fuel: their generation pathways are depicted in Figure 2.1. The Pu isotopes 239-242 originate from neutron capture in U-238, whilst Pu-238 owes its origins to U-235 that does not fission following neutron capture. The isotopic mixture of Pu in spent fuel is heavily dependent on the reactor type, fuel enrichment, burn-up, and operating conditions; Table 2.1 demonstrates this, recording, for different production routes, the typical Pu isotopic content at fuel discharge.

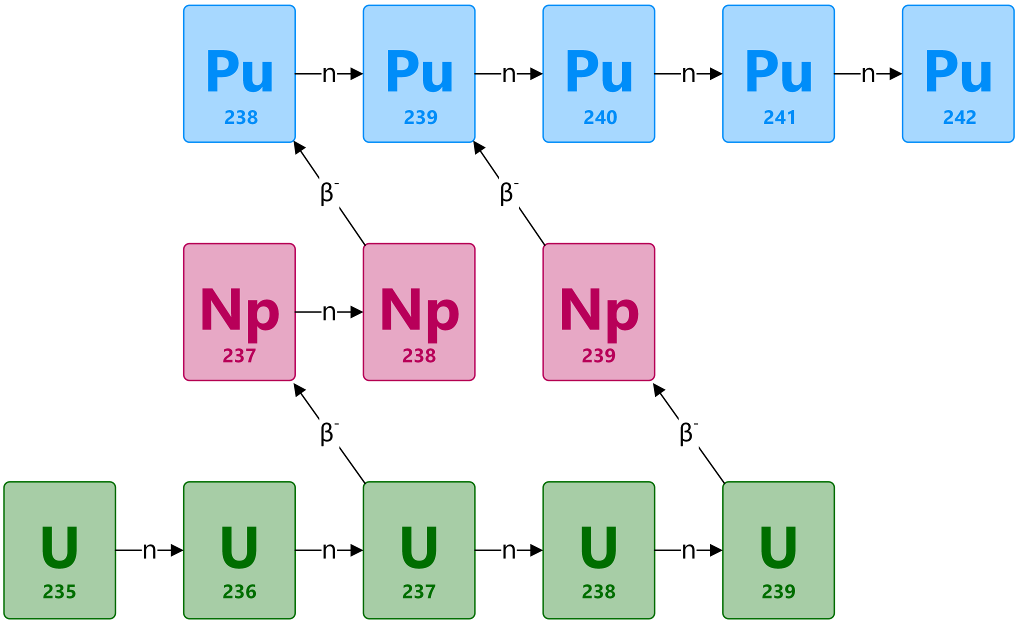

Figure 2.1: Formation of plutonium isotopes from uranium-based nuclear fuel.

Table 2.1: The typical plutonium isotopic composition produced in different reactor-types at varying burn-ups [17].

Reactor type	Mean burn-up (MWd/t)	Percentage of Pu isotopes at discharge					Fissile content (%)
		Pu-238	Pu-239	Pu-240	Pu-241	Pu-242	
Magnox	3000	0.1	80	16.9	2.7	0.3	82.7
	5000	N/A	68.5	25.0	5.3	1.2	73.8
CANDU	7500	N/A	66.6	26.6	5.3	1.5	71.9
AGR	18000	0.60	53.7	30.8	9.9	5.0	63.6
BWR	27500	2.6	59.8	23.7	10.6	3.3	70.4
	30400	N/A	56.8	23.8	14.3	5.1	71.1
PWR	33000	1.3	56.6	23.2	13.9	4.7	70.5
	43000	2.0	52.5	24.1	14.7	6.2	67.5
	53000	2.7	50.4	24.1	15.2	7.1	65.6

CANDU: CANada Deuterium Uranium, AGR: Advanced Gas-cooled Reactor, BWR: Boiling Water Reactor, PWR: Pressurised Water Reactor.

Pu-239 is the most common isotope produced in all reactor types. Pu that contains Pu-240 exceeding 19% of the isotopic content is defined as reactor-grade; the Magnox reactors were designed to produce military Pu, as such, they contain a very high percentage of Pu-239. Table 2.1 shows how increasing the burn-up results in a spent fuel containing a higher percentage of the heavier Pu isotopes, a consequence of an increased number of the successive neutron captures illustrated in Figure 2.1. As Pu-238 originates from U-235, reactors that use low enriched U produce very small quantities of the isotope — the Magnox and CANDU reactor types demonstrate this in Table 2.1.

Of the five Pu isotopes present in spent fuel, two have a half-life under 100 years. Pu-238 undergoes α decay to U-234 with a half-life of 88 years — its production of alpha particles crucial in making it suitable for usage in RTGs and RHUs – and Pu-241 undergoes β^- decay to Am-241 with a half-life of 14.4 years. As a consequence, Pu stored for several years becomes contaminated with Am; the impact of this on the properties of PuO_2 is investigated in Chapter 5. Pu-240 is the isotope with the third shortest half-life at 6560 years.

Pu is often considered to be the most complex element in the periodic table [18]. Its position between the early actinide elements (Th-Np), where the 5*f* electrons are delocalised and thus contribute to bonding, and later elements of the series (Am and beyond), where they are well localised, places it at the transition between two well-understood limits, resulting in Pu having the highest number of allotropic phases — some of which have dramatically different atomic volumes [19]. Figure 2.2 shows the experimental phase diagram of Pu, highlighting how the change in atomic volume between the phases can exceed 25%. At room temperature and below, Pu is in the low symmetry, very dense, α-phase. As it is heated at atmospheric pressure to its melting point (where it contracts), Pu exists in six distinct crystal structures. These phases behave uniquely and the transition between phases can be dramatic, with sudden density changes. The transition in

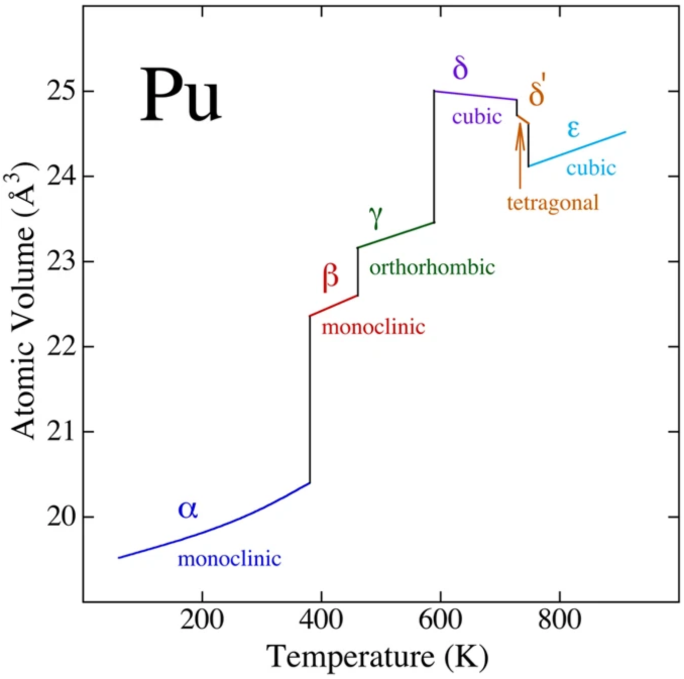

Figure 2.2: The experimental phase diagram for plutonium metal. Redrawn by [21] after [22].

the role of the 5*f* electrons occurs between these metallic phases and explains the huge variation in properties: the 5*f* electrons contribute to bonding in the phases stable at low temperatures, whilst they become increasingly localised in the phases stable at elevated temperatures — this is evidenced by the formation of structures with increasing symmetry. Another result of this complex chemistry is that even identification of formal oxidation states is a work in progress, with the +II state only being added to the six other confirmed states in 2017 [20].

2.2 Plutonium oxides

2.2.1 Pu-O phases

PuO_2 is the compound of choice used to handle, store, and transport Pu. The introduction also outlined the compound's technological importance in applications that include its use as a component of MOX fuel or as the fuel source in RHUs and

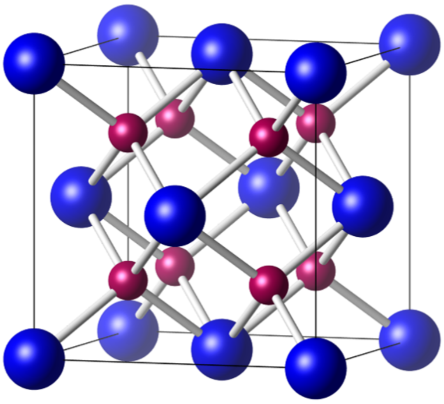

Figure 2.3: The unit cell of $Fm\bar{3}m$ PuO_2, with plutonium and oxygen atoms depicted with blue and red spheres respectively.

RTGs. Pu metal reacts with air at room temperature to form plutonium oxides; alternatively, the dioxide is synthesised by calcination or pyrolysis of the oxalate, nitrate, or peroxide. The crystal structure of PuO_2 is equivalent to other actinide dioxides and is a face centred cubic (FCC) structure, with a crystal symmetry described by the $Fm\bar{3}m$ (No. 225) space group. The unit cell of PuO_2 is illustrated in Figure 2.3: the Pu(IV) cations are in 8-fold coordination to their neighbouring O^{2-} anions. The unit cell consists of eight oxygen-occupied tetrahedral sites, and four empty octahedral sites.

The Pu-O phase diagram (Figure 2.2) is complex; it includes hypo-stoichiometric $PuO_{2\text{-x}}$ existing at a wide composition range reported to be from 61.3 to 66.7 at.% O [23], the bcc oxide $PuO_{1.67}$ existing across a small composition range of approximately 61.7 to 63.0 at.% O, and another bcc oxide, $PuO_{1.52}$, that exists at an even smaller composition range at around 60.3 at.% O. The most reduced oxide is the trivalent sequioxide Pu_2O_3; again, this phase has a narrow composition range at around 60 at.% O.

The value of x in $PuO_{2\text{-x}}$ has been studied by several authors; it can be determined using experimental measurements of the oxygen potential. The context of these studies is to understand the variation of the oxygen potential in MOX fuel, which

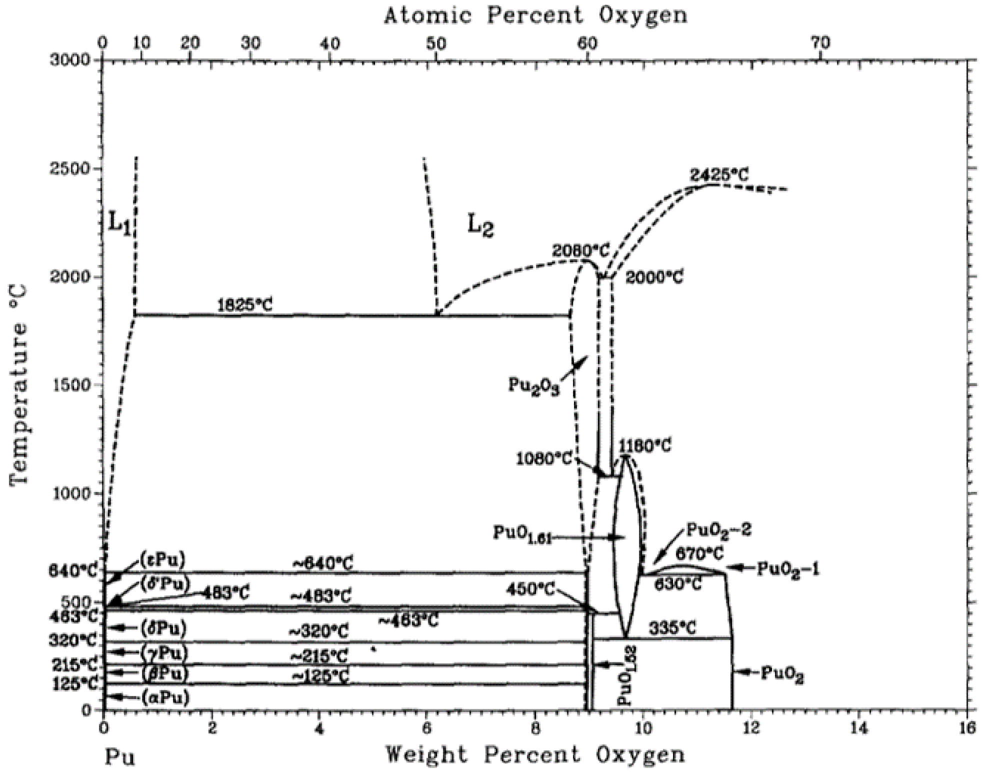

Figure 2.4: The assessed Pu–O phase diagram from Wriedt [23].

consists of a blend of UO_2 and PuO_2. The oxygen potential of nuclear fuel directly affects the fuel oxidation state which in turn influences crucial performance characteristics such as the diffusion of fission products [24]. The measured oxygen potential data can be used to establish the relationship between x in PuO_{2-x} and the oxygen partial pressure, $\mathrm{P_{O_2}}$. Equation 2.1 describes the idealised relationship for an oxygen deficient oxide:

$$x \propto \mathrm{P}_{\mathrm{O}_2}^{-\frac{1}{n}} \tag{2.1}$$

Atlas and Schlehman [25] measured the variation in the oxygen content of PuO_{2-x} from 1045°C to 1545°C using either a gas analysis or gravimetric method; the analysis found that n varied between 4.15 and 3.22 in the temperature range. Swanson [26], who measured the oxygen potential from 800°C to 1300°C with a controlled-atmosphere thermogravimetry procedure, reported that n varies between 3.6 and 5.45 in this range; however, if just considering the data between 900°C and 1300°C, n is very near to 5 in all cases. This is in close agreement to the reported results of Woodley [27] whose data was also obtained using thermogravimetric techniques from 1000°C to 1200°C, with a independent method — a galvanic cell technique — confirming the results. In much more recent work, Komeno *et al.* [28] report that n equals 4. This is based on data obtained from 1200°C to 1600°C by a gas equilibrium method using thermogravimetry/differential thermal analysis (TG/DTA) — this work produced no data in the near-stoichiometric region.

When the relationship in Equation 2.1 is correct, n can be used to identify the defect type and charge that is responsible for the the deviation in x (this identification process will be explained and demonstrated in later chapters). It is clear from this review of experimental data that, judging from the variation of n, there is uncertainty in the defect processes that are responsible for the deviation, x, in PuO_{2-x}.

In contrast to the sub-oxides, the existence of higher oxides (i.e. PuO_{2+x}) is the subject of considerable debate. As such, they do not appear on the phase diagram. The search for plutonium oxides higher than PuO_2 dates back to the Atomic Age, but a wide belief that the dioxide is the highest valent oxide was in place by the late 1980s. In addition to scientific curiosity, the search is motivated by a need to fully understand the behavior of the material in long-term storage: their existence could necessitate a reconsideration of current procedures. At the turn of the century, Haschke *et al.* [29] sparked a resurgent interest in the search, reporting the observation of oxides up to $PuO_{2.27}$ formed by a reaction with water. It has been proposed that the hyper-stoichiometry is accommodated by oxygen interstitials located at the octahedral site: Petit *et al.* [30] described the interstitial oxygen as O^{2-}, in contrast to Prodan *et al.* [31] who concluded that the interstitial oxygen was best described as O^{-}. Korzhavyi *et al.* [32] report that reactions of PuO_2 with either O_2 or H_2O to form PuO_{2+x} are endothermic; the production of PuO_{2+x} via the reaction of PuO_2 and the radiolysis products of water was found to be exothermic, however the PuO_{2+x} formed existed only as an intermediate product. Additional work supports the finding that a binary oxide higer than PuO_2 likely exists only as an intermediate product, with multiple authors proposing that hyper-stoichiometric Pu oxides are better described as $PuO_2(OH)_x$ [33, 34, 35].

2.2.2 PuO_2 interim storage

At the UK's Sellafield site, the 140 ton stockpile of Pu is stored as a PuO_2 powder within a series of nested stainless steel or aluminium cans with storage integrity maintained with a screw topped, or welded, outer layer. The design has changed and adapted over the course of time; Figure 2.5 depicts a design used to store Pu originating from Magnox reactors which includes a polymer bagging layer. For approximately 5% of the canisters storing Magnox derived Pu, this bagging layer was fabricated from polyvinyl chloride (PVC) [36]. This material has undergone

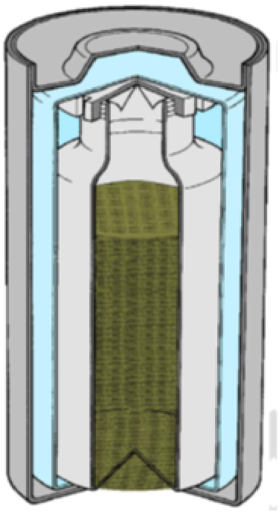

Figure 2.5: Cutaway diagram depicting a multiple barrier containment Magnox storage canister. In this example, the green PuO_2 material is surrounded by a light-grey aluminium canister, a blue polymer bagging layer, and a dark-grey stainless steel outer canister.

radiolytic degradation, resulting in chlorine-contaminated PuO_2. The other major source of PuO_2 is that originating from the ThORP which reprocesses spent oxide fuels from UK Advanced Gas Cooled reactors or foreign light water reactors.

One of the most serious hazards analysed in the creation of current and future packaging designs is the possible occurrence of pressurisation within the sealed containers. The hazard analysis must also understand the composition of generated gases to determine whether the formation of an explosive mixture is a feasibility. Several mechanisms may combine to cause pressurisation in a sealed PuO_2 canister:

- Temperature effects: heat generated from the radiocative decay of the stored material will cause expansion of the fill gas. Other sources of thermal input may exist; for example, the canister's external environment.
- Helium generation: alpha decay of Pu will produce significant quantities of He over storage time periods. The extent to which the He generated will contribute to any pressurisation will be dependent on the amount retained

in the PuO_2 lattice.

- Desorption: The increased temperarures that occur after packing can cause some adsorbed species to desorb and vapourise. Of most significance will be the desorption of any water from the hygroscopic PuO_2 as steam.
- Radiolysis: When irradiated, some compounds are vulnerable to dissociation. In the storage canister, water adsorbed on PuO_2 can produce H_2 when subjected to radiolysis. Additional consideration must be given to the small number of canisters holding Magnox derived Pu that include a PVC bagging layer: production of gaseous products due to the radiolysis of this polymeric material has been observed.
- Chemical reactions: A number of reactions could occur between a variety of reactants co-existing in the sealed canisters. A large aim of the packaging design and procedures is to limit the reactions that could occur. The most important to consider is a reported moisture enhanced corrosion reaction that produces H_2 and PuO_{2+x}.
- Ignition: the potential deflagration or detonation of a canister with a combustible atmosphere (not of high concern for reasons detailed below).

The production of H_2, possible via multiple mechanisms according to the above list, evokes concern for the integrity of the storage canisters. However, analysis has shown that, provided excessive moisture adsorption between calcination and packaging is avoided, a combustible atmosphere will not exist. The process that ensures this can be explained in its most simplified form by the two following reactions [37]:

If O_2 present:

$$\mathrm{PuO_{2(s)}} + \frac{x}{2}\mathrm{O_2} + \mathrm{H_2O} \longrightarrow \mathrm{PuO_{2+x(s)}} + \mathrm{H_2O_{(ads)}} \tag{2.2}$$

If O_2 *not* present:

$$\mathrm{PuO_{2(s)}} + x\mathrm{H_2O_{(ads)}} \longrightarrow \mathrm{PuO_{2+x(s)}} + x\mathrm{H_2} \tag{2.3}$$

These reactions imply that O_2 is depleted prior to H_2 production. Additionally, the reverse reaction of Equation 2.3 is favorable at moderate H_2 pressures, and if H_2 and O_2 do co-exist, they will quickly recombine to produce water [38]. Uncertainty and debate around these processes and mechanisms does exist, motivating and warranting further studies. In particular, the existence and role of PuO_{2+x} is a very important topic.

A package surveillance programme monitors the PuO_2 stored at Sellafield. The Magnox packages surveyed have, regardless of age (packages tested ranged in age from six months to 43 years old), been found to be at sub-atmospheric pressure; this is despite the presence of radiogenic He gas [39]. The mechanism of this depressurisation has been attributed to the radiolysis of N_2 and O_2 to NO_x, as well as thermal and radiolytic reactions of the polyethylene bagging material that adsorb O_2 [40]. ThORP packages differ quite significantly: the PuO_2 is stored under argon and without the polymer bagging. They are also thermally hotter and generate more He — a consequence of the material's higher specific activity. The characterisation of these canisters' gas composition has reported that no O_2 or H_2 is present [39].

This discussion has centred around PuO_2 stored at the UK's Sellafield site, but remains largely relevant and applicable to PuO_2 stored worldwide. For example, the arrangements and procedures used by the Department of Energy to store US PuO_2 are very similar [40, 41].

2.3 Density functional theory

2.3.1 Overview

As stated in the introduction, the first theorem of Hohenberg and Kohn [14] proved that: *The ground-state energy from Schrödinger's equation is a unique functional of the electron density*. The significance of this is enormous: the electron density is a function of only three coordinates, whilst the full wave function solution to Schrödinger's equation is a function of 3*N* coordinates (where *N* is the total number of electrons). The second Hohenberg-Kohn theorem unlocks the path to defining the functional: *The electron density that minimises the energy of the overall functional is the true electron density corresponding to the full solution of Schrödinger's equation*. In other words, with the 'right' functional, the electron density could be varied until the energy from the functional is minimised. DFT has been developed with the formulation of Kohn and Sham [42], where the correct electron density is found by solving a set of single electron equations. The electron density at a particular position in space, $n(\mathbf{r})$, is evaluated using Equation 2.4, where the summation extends over all single-particle wave functions, $\psi_i(\mathbf{r})$.

$$n(\mathbf{r}) = \sum_i |\psi_i(\mathbf{r}_i)|^2 \tag{2.4}$$

The single-particle wave functions are found using Equation 2.5, with a Hamiltonian consisting of the electron kinetic term and the effective potential functional, $v_{\text{eff}}(\mathbf{r})$.

$$\left[-\frac{\hbar^2}{2m}\nabla_i^2 + v_{\text{eff}}(\mathbf{r})\right]\psi_i(\mathbf{r}) = \varepsilon_i\psi_i(\mathbf{r}) \tag{2.5}$$

$v_{\text{eff}}(\mathbf{r})$ is a functional of the electron density; it can be broken down into three potentials:

$$v_{\text{eff}}(\mathbf{r}) = V(\mathbf{r}) + V_H(\mathbf{r}) + V_{\text{XC}}(\mathbf{r}) \tag{2.6}$$

V defines the interaction between an electron and the collection of atomic nuclei. V_H is the Hartree potential, it describes the Coulomb repulsion between the electron under consideration and the total electron density of the system:

$$V_H(\mathbf{r}) = e^2 \int \frac{n(\mathbf{r'})}{[\mathbf{r} - \mathbf{r'}]} d^3r' \tag{2.7}$$

The electron under consideration is included in the total electron density necessitating the use of a correction to cancel the self-interaction energy, this forms a part of V_{XC}, the exchange and correlation potential. V_{XC} also includes the quantum mechanical effects not included in the other potentials. The formal definition of V_{XC} is that it is a functional derivative of the exchange-correlation energy:

$$V_{\mathrm{XC}}(\mathbf{r}) = \frac{\delta E_{\mathrm{XC}}(\mathbf{r})}{\delta n(\mathbf{r})} \tag{2.8}$$

The simplest approximation for E_{XC} is the local density approximation (LDA) which sets E_{XC} at each position from the exchange-correlation potential of the uniform electron gas (which is known) at the electron density calculated at that position. The LDA functional for the exchange-correlation energy can be written as:

$$E_{\mathrm{XC}}^{\mathrm{LDA}}(n(\mathbf{r})) = \int n(\mathbf{r})\varepsilon_{\mathrm{XC}}(n(\mathbf{r}))dr \tag{2.9}$$

where $\varepsilon_{\mathrm{XC}}$ is the exchange-correlation energy per particle of the uniform electron gas with a charge density $n(\mathbf{r})$. The total exchange-correlation energy is described as individual exchange (E_{X}) and correlation (E_{C}) components:

$$E_{\mathrm{XC}}(n(\mathbf{r})) = E_{\mathrm{X}}(n(\mathbf{r})) + E_{\mathrm{C}}(n(\mathbf{r})) \tag{2.10}$$

with a corresponding equation in terms of the single particle terms; the one-electron exchange energy (ε_{X}), and one-electron correlation energy (ε_{C}):

$$E_{\mathrm{XC}}(n(\mathbf{r})) = \int n(\mathbf{r})\varepsilon_{\mathrm{X}}(n(\mathbf{r}))dr + \int n(\mathbf{r})\varepsilon_{\mathrm{C}}(n(\mathbf{r}))dr \tag{2.11}$$

The exchange potential is given by the Dirac functional [43]:

$$\varepsilon_{\mathrm{X}}(n(\mathbf{r})) = -\frac{3}{4}\left(\frac{3}{\pi}\right)^{\frac{1}{3}} n(\mathbf{r})^{\frac{1}{3}} \tag{2.12}$$

An exact expression for the correlation term does not exist, however accurate values for ε_{C} have been determined from interpolation of Quantum Monte Carlo (QMC) calculations to provide an analytic form for ε_{C} [44, 45]. A fairly good result for E_{XC} is achievable, especially when $n(\mathbf{r})$ has a very low spatial variation. In an attempt to improve upon the LDA, the general gradient approximation (GGA) also incorporates the local gradient in the electron density in order to account for the non-homogeneity of the true electron density. GGA functionals have the following form:

$$E_{\mathrm{XC}}^{\mathrm{GGA}}(n(\mathbf{r})) = \int n(\mathbf{r})\varepsilon_{\mathrm{XC}}(n(\mathbf{r}), \nabla n(\mathbf{r}))dr \tag{2.13}$$

where $\varepsilon_{\mathrm{XC}}$ depends not just on the value of the density at a point but also on its gradient. Many subdivisions of the GGA exist, differing in the incorporation approach of the gradient in the electron density.

Self-interaction error

The self-interaction error (SIE) arises when the self-interaction energy — the Coulombic energy associated with the interaction of each electron with its own density within the entire electron density — is improperly cancelled by the selected exchange-correlation functional. This error is prominently found in systems with a ground state that is characterised by strongly localised electrons. The SIE results in an over delocalisation of these electrons, an effect felt by the $5f$ electrons in actinide dioxides. As a result, in conventional DFT PuO_2 is described as conducting when in fact PuO_2 is classified as a charge-transfer insulator [46]. The over delocalisation of these electrons is caused by an incorrect account of the exchange and correlation interactions in the E_{XC} functional that consequently fails to cancel out the self-interaction included in the Hartree term. This spurious self-interaction now acts on portions of the charge density associated with these electrons, causing a repulsive effect that induces the excessive delocalisation.

An alternative method to DFT is the Hartree-Fock (HF) method which focuses on wave functions and orbitals and ignores the electron correlation. The self-interaction energy is exactly cancelled by the contributions to the energy from exchange in the HF method. Hybrid DFT functionals blend a portion of the exact HF exchange energy with the GGA exchange to offer (at the very least) a reduced SIE:

$$E_{\mathrm{XC}}^{\mathrm{Hybrid}} = E_{\mathrm{XC}}^{\mathrm{GGA}} + \alpha \left(E_{\mathrm{X}}^{\mathrm{HF}} - E_{\mathrm{X}}^{\mathrm{GGA}} \right) \tag{2.14}$$

In this equation $E_{\mathrm{X}}^{\mathrm{HF}}$ and $E_{\mathrm{X}}^{\mathrm{GGA}}$ are the HF and GGA exchange energies, respectively. α is the mixing parameter. It has been demonstrated that hybrid functionals can offer significantly improved descriptions of band gaps, especially in small- to medium- gap systems ($<$ 5 eV) [47], with several studies adopting the approach to study PuO_2, with good experimental replication achieved [31, 48]. These two alternatives are, compared to conventional DFT, much more computationally intensive methods. At the time of writing, these methods cannot be feasibly deployed to study defect-containing supercells.

A method used extensively to correct the SIE that requires only a marginally larger computational effort than conventional DFT is the DFT + U method. The basic principle of the method is to describe the strongly correlated electrons separately using a Hubbard model, whilst the remaining valence electrons are described using a conventional DFT functional. In actinide dioxides the Hubbard model is applied to the $5f$ electrons and past studies have demonstrated a successful correction of the SIE, yielding good reproduction of the ground-state electronic properties seen in actinide dioxides [46, 49]. The DFT + U total energy can be summarised as:

$$E_{\mathrm{DFT+U}}(n(\mathbf{r})) = E_{\mathrm{DFT}}(n(\mathbf{r})) + E_{\mathrm{Hub}}(\hat{n}(\mathbf{r})) - E_{\mathrm{dc}}(\hat{n}(\mathbf{r})) \tag{2.15}$$

where $E_{\mathrm{DFT}}(n(\mathbf{r}))$ is the DFT total energy of the system and the $E_{\mathrm{Hub}}(\hat{n}(\mathbf{r}))$ term contains the Hubbard model that describes the correlated states. Because these two terms are summed, the states described by $E_{\mathrm{Hub}}(\hat{n}(\mathbf{r}))$ are counted twice. The double-counting term, $E_{\mathrm{dc}}(\hat{n}(\mathbf{r}))$, aims to model and remove the contribution of the correlated electrons from $E_{\mathrm{DFT}}(n(\mathbf{r}))$. A unique definition of $E_{\mathrm{dc}}(\hat{n}(\mathbf{r}))$ does not exist, resulting in several variants of the DFT + U method that that vary based upon their calculation of $E_{\mathrm{dc}}(\hat{n}(\mathbf{r}))$.

Two variants widely used are the formulism's of Liechtenstein *et al.* [50] and Dudarev *et al.* [51]. In packages that perform DFT + U calculations execution of the method requires the selection of two adjustable variables. These are the on-site Coulombic (U) and exchange interaction (J) parameters, which remain independent in the Liechtenstein *et al.* formulism or construct $U_{\mathrm{eff}} = U$ - J in the Dudarev *et al.* formulism. When $J = 0.0$ eV, the two formulisms are equivalent.

In past studies of PuO_2, the U and J parameters have been obtained by fitting to structural and electronic properties of PuO_2 [48, 49, 52, 53, 54, 55]. Reproduction of the electronic band gap is seen as a strong metric of success. Most previous DFT + U studies of PuO_2 fit U and J to reproduce the bandgap McNeilly *et al.* [56] reported in the 1960s (1.8 eV), however the much more recent experimental study of McCleskey *et al.* [57] in 2013 reports a higher band gap of 2.8 eV. The variation has grown even further with the very recent reporting (2021) of a band gap of between 3.92 eV and 4.1 eV by Roussel *et al.* [58, 59]. This large discrepancy in the experimental bandgap for PuO_2 poses significant questions for determination of the appropriate values for U and J.

Dispersion correction

It is now well established that conventional Kohn-Sham DFT approximations fail to describe long-range London dispersion interactions correctly. Dispersion interactions can be empirically defined as the attractive part of the van der Waals interaction between atoms and molecules that are not directly bonded [60]. These interactions are asymptotically governed by the relation:

$$E_{\mathrm{disp}} \propto -\frac{C_6}{R^6} \tag{2.16}$$

which shows that, at long range — where the electron density of two atoms or molecules negligibly overlap — the dispersion energy, E_{disp}, depends on the internuclear distance, R, with C_6 being the sixth-order dispersion coefficient [60]. There exists several different approaches to solve the dispersion problem that arises in conventional DFT; in later chapters this thesis will use the DFT-D approach — a method considered robust due to its rigorous testing and implementation in thousands of different systems [61]. The DFT-D approach is based on additive corrections to the Kohn-Sham DFT energy that — depending on the variant used — can be solely pairwise in nature or can also contain many body terms; Goerigk [62] reviews the variants in the DFT-D method. As the calculated dispersion correction is an add-on term it contributes to the forces acting on the atoms — resulting in a different geometry optimisation with the correction applied — but does not alter the electronic structure. This represents the main drawback to the DFT-D approach, but the effects are small, or often negligible, in the majority of practical applications [61].

2.3.2 Plane-wave DFT

To study periodic structures — that is, structures invariant in certain directions with respect to translations of a unit cell length — plane-wave DFT is very widely used. Bloch's theorem states that the wave function of an electron, $\psi_k(\mathbf{r})$, within a periodic potential can be defined in terms of the periodicity of the system:

$$\psi_k(\mathbf{r}) = \exp(i\mathbf{k}\cdot\mathbf{r})u_{\mathbf{k}}(\mathbf{r}) \tag{2.17}$$

$u_{\mathbf{k}}(\mathbf{r})$ shares the same periodicity as the lattice, the functions $\exp(i\mathbf{k}\cdot\mathbf{r})$ are referred to as plane waves — giving the method its name. Whilst the space of vectors **r** is the real space, the space of vectors **k** is referred to as the reciprocal, or k, space. Using the reciprocal space within the mathematical operations of DFT becomes very practical — several features of this space are important to mention:

- Increasing the lattice vectors in real space corresponds to a decrease in the lattice vectors in reciprocal space.
- The Brillouin zone is the name given to a primitive cell defined in reciprocal space, where the primitive cell — or more precisely, the Wigner-Seitz cell — is the volume that encloses all points in space that are closer to a given lattice point than any other.
- Positions in the Brillouin zone with high symmetry are of significance, and are named critical points. The most important critical point is the Γ-point, located at the centre of the Brillouin zone.

Integrating over the Brillouin zone is a key operation performed in any plane-wave DFT code. To practically do so, the integrals are approximated by a sum, which is then evaluated over a finite number of k-point samples in the Brillouin zone. Due to the computational effort associated with evaluating these integrals, the selection of the k-points in the Brillouin zone necessitates careful consideration. A regularly spaced grid of k-points is frequently used; the method developed by Monkhorst and Pack [63] falls into this category. To use the Monkhorst-Pack method requires only the specification of the number of k-points in each direction of reciprocal space. For cubic systems, it is sensible to use the same number (N) of k-points in each direction, resulting in the commonly seen labelling of a $N \times N \times N$ k-point mesh.

Equation 2.17 informs that $\psi_k(\mathbf{r})$ can be expressed as the product of a plane wave and $u_{\mathbf{k}}(\mathbf{r})$, a function with the same periodicity of the lattice. This periodicity allows $u_{\mathbf{k}}(\mathbf{r})$ to be expanded in terms of a Fourier series:

$$u_{\mathbf{k}}(\mathbf{r}) = \sum_{\mathbf{G}} c_{\mathbf{G}} \exp(i\mathbf{G} \cdot \mathbf{r}) \tag{2.18}$$

where $c_{\mathbf{G}}$ are plane wave expansion coefficients and the sum extends over the reciprocal lattice vectors. Combining Equations 2.17 & 2.18 gives:

$$\psi_k(\mathbf{r}) = \sum_{\mathbf{G}} c_{\mathbf{k}+\mathbf{G}} \exp(i(\mathbf{k} + \mathbf{G}) \cdot \mathbf{r}) \tag{2.19}$$

This expression implies that there is an infinite number of allowed **G** values at each point in k-space. Fortunately, as $|\mathbf{G}|^2$ becomes larger, the $c_{\mathbf{k}+\mathbf{G}}$ coefficient decreases in magnitude. A cut-off energy is therefore defined; plane waves are included only if they have energies less than this cut-off:

$$E_{\text{cut}} = \frac{\hbar^2}{2m}|\mathbf{G}|^2 \tag{2.20}$$

This discussion has introduced two parameters to be defined in a DFT calculation: E_{cut} and the number of k-points. It must be ensured that both are sufficiently high to give accurate results; this can be achieved by exploring the convergence of the DFT calculations with respect to the two parameters. In practice, this means increasing E_{cut}, or the number of k-points, until the relationship between these parameters and the total energy is independent.

Pseudopotentials

Regions of space where the wave function varies — or oscillates — very quickly possess very large **G** components. This occurs when the potential is very attractive; the tightly bound core electrons in atoms experience this most. As a result, a calculation that considers each electron in an atom explicitly — a so-called all-electron calculation — would need to set a high E_{cut} value. To avoid this high computational burden, pseudopotentials are used. In essence, pseudopotentials replace the electron density of a select number of core electrons with a smoothed density that matches important properties of the true ion core; this is named the frozen-core approximation. The method is depicted in Figure 2.6. Adoption of a pseudopotential allows a smaller E_{cut} value as the wave functions now oscillate less near the nucleus. This approach is acceptable owing to the fact that core electrons are not notably important in defining the chemical, mechanical or electronic properties of materials; it is the valence electrons that largely control these properties. Methods in defining pseudopotentials vary. Particular pseudopotentials are associated with minimum cut-off energies. 'Hard' pseudopotentials require high cut-off energies; 'soft' pseudopotentials can be used with low cut-off energies.

2.3.3 Electronic & structural relaxation

The second Hohenberg-Kohn theorem, stated at the beginning of this section, makes clear the path that can be taken to find the ground state electron density. Figure 2.7 generalises how this is done in practice by DFT packages, with the use of an iterative procedure. The inner loop is named the Self-Consistent Field (SCF) method; the problem of efficiently updating the charge density in each iteration has generated a considerable volume of work, with numerous mixing algorithms developed. The outer, ionic relaxation loop requires the force exerted on each ion to be calculated; the Hellmann-Feynman theorem enables these forces to be cal-

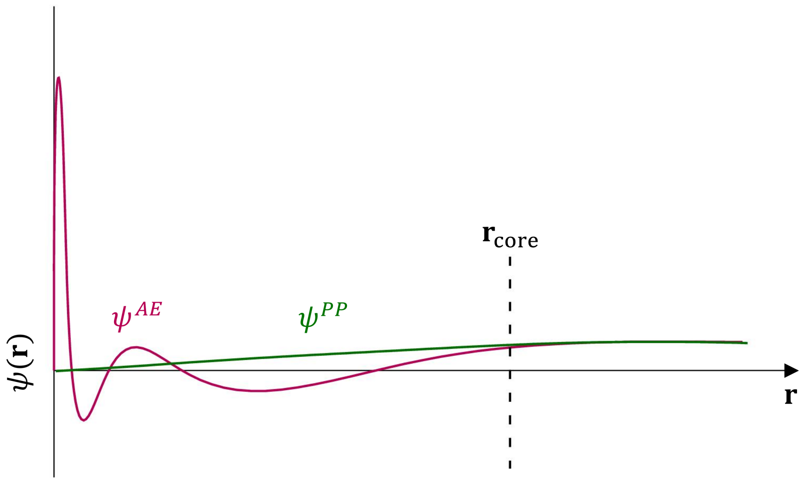

Figure 2.6: Illustration of pseudopotential methods. ψ^{AE} represents the all-electron form of the wave function, whilst ψ^{PP} is the pseudo wave function that replaces the potential within the core region ($\mathbf{r}_{\text{core}}$). Beyond the core region both the pseudo and all-electron wave functions should be identical.

culated using solely the wave functions calculated in the SCF cycle. The force on ion j is the partial derivative of Kohn Sham energy with respect to the position of the ion, $\mathbf{R}_j$:

$$\mathbf{F}_j = -\frac{\partial E}{\partial \mathbf{R}_j} \tag{2.21}$$

The atomic perturbations applied to the ions in each iteration is another optimisation problem that a multitude of algorithms have been developed for. Two of the most successful are the conjugate-gradient and quasi-Newton RMM-DIIS algorithms; these two algorithms have been deployed in this thesis to relax the structures studied.

2.4 Bulk PuO$_2$: previous studies

2.4.1 Equilibrium properties

DFT has now been employed to study PuO$_2$ across many studies. Due to the decisions that must be made when setting up a DFT simulation of PuO$_2$, the resulting

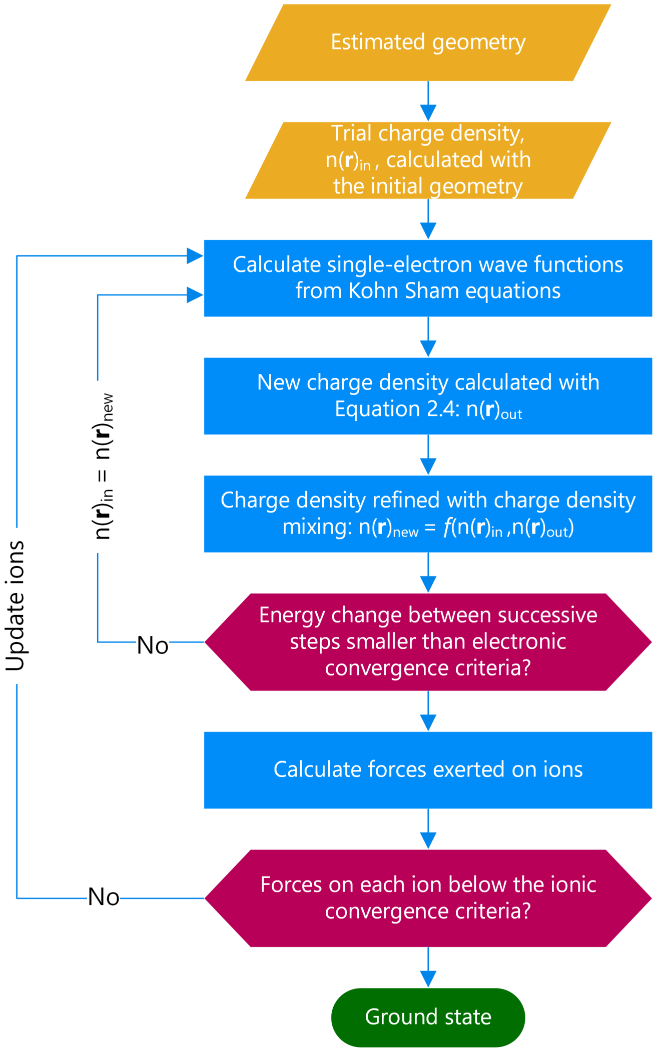

Figure 2.7: Summary of the iterative method used by DFT packages to find the ground state.

equilibrium properties are seen to vary across these studies. Table 2.2 attempts to highlight this: it displays the lattice constant and band gap of PuO$_2$ reported by previous studies, that differ based upon the DFT input parameters selected. Looking first at the DFT + U studies, a trend can be observed based upon the type of exchange-correlation used. When LDA is selected, the lattice constant is under the experimental value; when GGA is selected the lattice constant is above the experimental value. Note that Perdew-Burke-Ernzerhof (PBE) [64] and PBE revised for solids (PBEsol) [65, 66] are subsets of GGA. It can be seen that it is popular to use a *U* value between 4.0 and 4.7 eV, with *J* set between 0.7 and 0.75 eV. Studies that adopt these values produce a band gap that closely resembles the experimentally reported band gap of 1.80 eV (McNeilly 1964 [56]) with the exception of the study by Jomard *et al.* [67] which obtained a band gap of 2.1-2.2 eV. Pegg *et al.* [48] used a higher *U* value of 6.0 eV and matched exactly the more recent experimentally reported band gap of 2.80 eV (McCleskey *et al.* 2013 [57]). Hybrid DFT is seen to best reproduce the experimental lattice constant value, whilst predicting a band gap in the region of the experimental band gap reported more recently, 2.80 eV. In addition to being a lower energy ground state, Pegg *et al.* [48] report that the longitudinal 3k-antiferromagnetic (AFM) state results in an increased band gap (regardless of *U* choice), compared to the 1k-AFM state used in the other studies discussed here — the magnetic properties of PuO_2 are introduced in much greater detail in the next section, Section 2.4.2.

It has been seen that DFT + U calculations can lead to several metastable solutions. A consequence of using DFT + U is that it imposes orbital degrees of freedom that are not present in conventional DFT; this can result in multiple self-consistent solutions, each of which can vary by several electron volts per formula unit [68]. This could result in an incorrect prediction of the ground state, which would not necessarily be easily detectable by inspection of physical properties. If convergence were to occur in one of the numerous metastable states it could invalidate predictions made using this method. A method to ensure the correct ground state is reached is proposed by Meredig *et al.* [68]. The method ramps *U* (beginning at $U = 0$) by 0.1 eV at a time, updating either the occupational matrix or alternatively, the previous wave functions and charge density. This method was employed by Ghosh *et al.* [52], with results from this study reported in Table 2.2. An alternative approach would be to simulate each possible occupational matrix and observe which the lowest energy state is. This method was employed by Jomard *et al.* [67] to calculate the ground state of PuO_2: results are reported in Table 2.2. A drawback to this approach is the high computational cost required to do an exhaustive search; Dorado *et al.* [69], using the method to study UO$_2$, required 61 DFT + U simulations when off-diagonal occupational matrices were included. Additionally, not all DFT simulation software offers the functionality to manually change the occupational matrix. The Vienna *ab initio* Simulation package (VASP) [70, 71, 72, 73] has been used to perform U ramping and occupational matrix control (OMC) with collinear PuO$_2$ magnetic states. However, it has been found that VASP is unable to read the results from previous non-collinear calculations, seemingly prohibiting the use of both U ramping and OMC when studying non-collinear magnetic states of PuO$_2$.

2.4.2 Magnetism

An important aspect in correctly simulating PuO$_2$ is the selection of an accurate description of its magnetic ground state. Figure 2.8 illustrates a collection of magnetic structures that can be considered for PuO$_2$. Identifying the correct magnetic ground state for PuO$_2$ has proven difficult. In fact, all actinide dioxides are subject to debate and challenges regarding their magnetic properties. For example, in NpO$_2$ the effective magnetic moment of the ground state has eluded detection; the odd number of electrons in the Np(IV) ion should result in a magnetic moment [77]. For PuO$_2$, experimental and theoretical studies have indicated differing ground states: A singlet diamagnetic (DM) ground-state is indicated from experimental observations [76] whereas ferromagnetic (FM) or AFM ground states have in the past been predicted from theory [31, 48, 55, 78].

As shown in Figure 2.8, AFM states are subject to subdivision based upon the directions of the magnetic moments exhibited by the ions. This is denoted by the magnetic moments being described by either one wave-vector (1k), two independent wave-vectors (2k), or three independent wave-vectors (3k): the latter two representing non-collinear behaviour. A further subdivision exists to distinguish the phase of the AFM state: either longitudinal or transverse. Many studies select

Table 2.2: Collection of results from previous studies of PuO$_2$ with key simulation parameters recorded.

	Authors	Method	U (eV)	J (eV)	Magnetic structure	SOC	Lattice constant (Å)	Band gap (eV)
DFT+U	Sun *et al.*	LDA	4.0	0.75	1k-AFM	No	5.36	1.7
	2008 [55]	GGA	4.0	0.75	1k-AFM	No	5.47	1.7
	Jomard *et al.*	LDA	4.0	0.7	1k-AFM	No		2.1
	2008 [67]	PBE	4.0	0.7	1k-AFM	No		2.2
	Zhang *et al.* 2010 [54]	LDA	4.0	0.75	1k-AFM	No	5.362	1.5
	Yang *et al.* 2014 [74]	PBE	4.0	0.75	1k-AFM	Yes	5.466	1.6
	Pegg *et al.* 2018 [48]	PBEsol	6.0	0.0	3k-AFM	Yes	5.415	2.80
	Ghosh *et al.* 2019 [52]	PBE	4.7	0.7	1k-AFM	No	5.460	1.6
Hybrid DFT	Prodan *et al.* 2005 [31]	PBE0	-	-	1k-AFM	No	5.385	3.4
	Prodan *et al.* 2006 [75]	HSE	-	-	1k-AFM	No	5.396	2.64
	Pegg *et al.* 2018 [48]	HSE06	-	-	3k-AFM	Yes	5.379	3.04
Exp.					DM[a]		5.398[b]	1.80-4.1[c]

[a] Reference [76]

[b] Reference [29]

[c] References [56, 57, 59, 58]

1k AFM ordering to describe PuO$_2$ [31, 52, 55, 67, 79, 80]. In their comprehensive study of magnetic order in PuO$_2$, Pegg *et al.* [48] found that 1k AFM states produce an incorrect crystal structure (the correct structure as indicated by experimental results is $Fm\overline{3}m$ crystal symmetry [81]) and that the choice of AFM phase (longitudinal or transverse) had a significant impact on the electronic and structural properties of PuO$_2$. This is a key finding, as most studies do not consider the AFM phase to be important. Pegg *et al.* [48] propose a longitudinal 3k AFM ground-state. Of all the magnetic configurations tested, this was the lowest in energy, was able to retain $Fm\overline{3}m$ crystal symmetry and replicated well the physical properties of PuO$_2$.

The study of Pegg *et al.* [48] was the first to consider relativistic effects through use of spin orbit interaction (SOI) and non-collinear magnetism. SOI refers to the interaction of an electron's spin motion with its orbital motion; it couples the lattice and magnetic structures. Not including SOI resulted in a different magnetic ground state being obtained, highlighting the importance of its inclusion. The discrepancy in results between theory and experiment are perhaps a consequence of the aforementioned experimental challenges that accompany the handling and examination of PuO$_2$. Further, it is possible that current experimental resolution cannot identify an ordered magnetic state for a small-moment material and/or an AFM-DM transition could be occurring outside of the temperature ranges investigated [48]. Additionally, the finding that this predicted ground state retains the $Fm\overline{3}m$ crystal symmetry could also have helped it avoid detection.

2.4.3 Electronic structure

As the actinide (An) series is crossed, the density of states (DOS) of AnO$_2$ has been shown to evolve; most notably due to the respective positions of the An 5*f* and O 2*p* bands. The study of Wellington *et al.* [82] demonstrated this: the DOS plots of UO$_2$, NpO$_2$, and PuO$_2$ in Figure 2.9 are taken from this work. Moving across

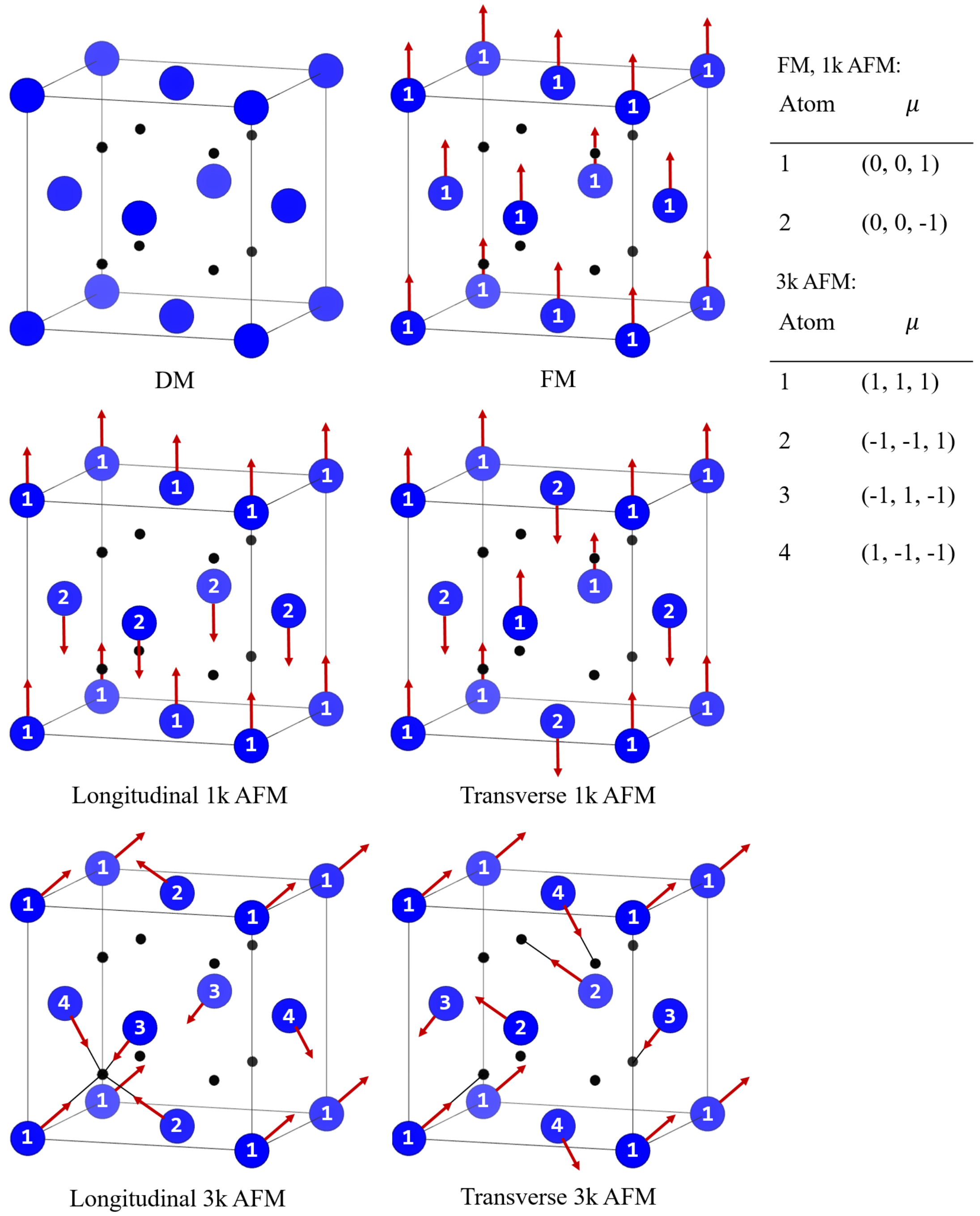
DM FM

Longitudinal 1k AFM Transverse 1k AFM

Longitudinal 3k AFM Transverse 3k AFM

FM, 1k AFM:

Atom	μ
1	(0, 0, 1)
2	(0, 0, -1)

3k AFM:

Atom	μ
1	(1, 1, 1)
2	(-1, -1, 1)
3	(-1, 1, -1)
4	(1, -1, -1)

Figure 2.8: Diamagnetic (DM), ferromagnetic (FM) and antiferromagnetic (AFM) structures of PuO$_2$, with AFM structures also differentiated by either the longitudinal or transverse domain. Plutonium and oxygen atoms are depicted with blue and black spheres, respectively. The direction of the effective magnetic moment (μ) on each plutonium ion is shown by an arrow and the μ = (a,b,c) wave-vector matrix key.

the series, the An 5*f* electrons become stabilised; they are brought into closer energetic proximity to the O 2*p* electrons. This results in the contribution of the O 2*p* bands to the valence band increasing and the oxides classification changing from a Mott-Hubbard to a charge-transfer insulator. The point of this transition in the series occurs at PuO_2. According to the results of Wellington *et al.* [82], in PuO_2 the occupied Pu 5*f* bands now overlay the occupied O 2*p* bands — they hybridise. As the top of the valence band has O 2*p* character, the material is a charge-transfer insulator. The work of Chen *et al.* [83] that modelled AmO_2 and CmO_2 predicts that the trend continues.

In a separate study that also employed the PBE0 functional, Prodan *et al.* [31] compare their computed total DOS to experimental data [84] (see Figure 2.9). Whilst the experimental data cannot provide robust insight regarding the positioning of the individual orbitals, the authors were encouraged that the features of this data — a weak peak at the Fermi level, followed by stronger peaks at -2.5 eV and -4.5 eV — were reflected in the theoretical result.

2.5 Point defects

2.5.1 Background

Broadly speaking, solid materials can be split into two classifications, based upon the arrangement of their constituent atoms. In an amorphous solid, the atoms arrange in no particular order, whilst in a crystalline solid, the atoms arrange in a repeating pattern. In a crystalline solid, the smallest group of atoms that can be used to form the repeating pattern is denoted as the unit cell of the structure. In this description the crystalline solid is treated as perfect; in reality, a crystalline solid will contain imperfections, or, defects. Various types of defects exist. If the defect involves only a single atom (a lattice point), or sometimes a very small set

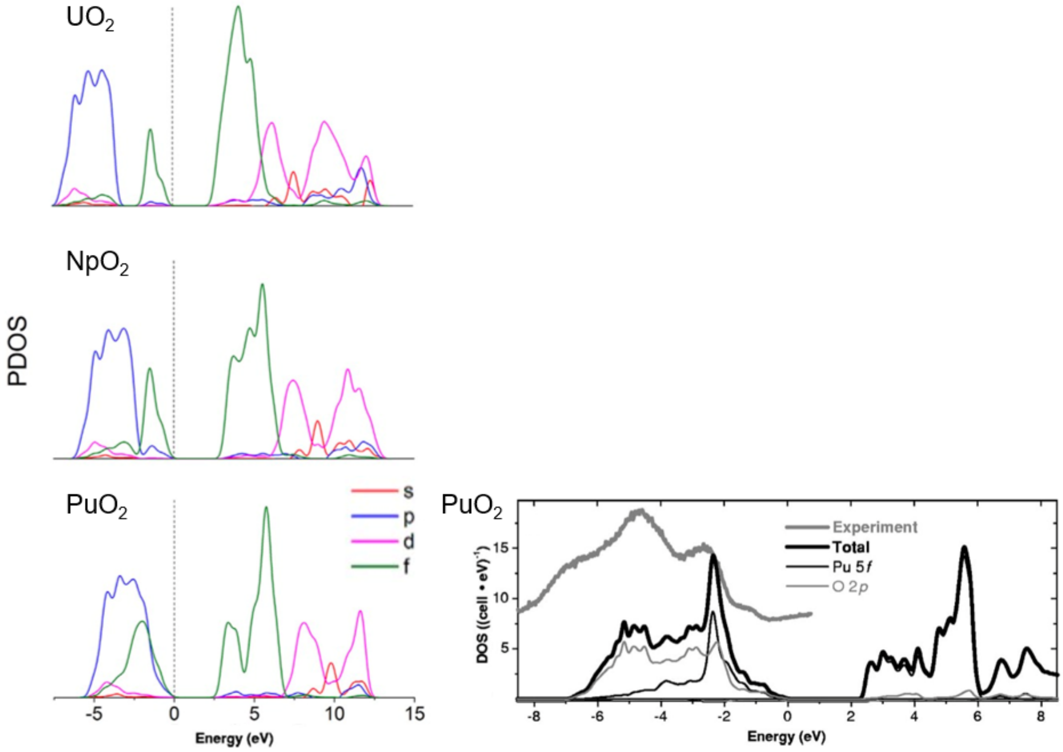

Figure 2.9: The density of states (DOS) of selected actinide oxides from literature. Left: the study of Wellington *et al.* [82] reporting the partial DOS of bulk AnO_2 (An = U, Th, or Pu) computed for $Pu_{16}O_{32}$ clusters with the periodic electrostatic embedded cluster method and the PBE0 functional. Right: the study of Prodan *et al.* [31] reporting the DOS of PuO_2 computed with the PBE0 functional with comparison made to experimental thin-film photoemission data measured at 77 K [84], (shifted upwards).

of localised atoms, it is referred to as a point defect. A line defect is restricted to a row of lattice points, whilst a plane defect involves an entire plane of lattice points. Defects formed within a material that do not involve foreign atoms are known as intrinsic defects. Conversely defects that incorporate a foreign atom (or atoms) are referred to as extrinsic defects. The rest of this section, and thesis, will discuss and investigate point defects.

An understanding of the underlying point defect processes responsible for the macroscopic properties of materials is fundamental to the development of higher performance materials. For example, point defects play a crucial role in the conductivity of semiconductors, the efficiency of solar cells and related optoelectronic devices, and, as most relevant in this thesis, the oxygen-to-metal ratio and ageing characteristics in metal oxide nuclear fuels.

Figure 2.10 illustrates the position the possible intrinsic point defects occupy within the PuO_2 unit cell. Pu- and O- vacancies are formed by the removal of an atom from its usual site. Pu- and O- interstitials are formed if an atom occupies a void space that under ordinary circumstances is unoccupied. In PuO_2, the unit cell shows that there will only be one favourable void space per formula unit: the octahedral interstitial site, named as such because the space is found in the interstices between six Pu atoms that form an octahedra. Another type of intrinsic point defect is the antisite defect, where atoms of a different type exchange positions. This defect is not illustrated (or studied) owing to its unfeasibility in PuO_2.

For PuO_2 extrinsic defects are a significant factor, owing to the materials radioactive decay. In a study focused on point defects, the decay products are considered extrinsic defects and can exist on the same lattice sites discussed for the intrinsic defects, shown in Figure 2.10. If a foreign atom sits on the regular site of a Pu or O atom, it is called a Pu- or O- substitutional. Alternatively it may occupy the interstitial site.

Figure 2.10 also aims to demonstrate the method by which point defects are simulated using DFT: the supercell methodology. This methodology places a point defect in a relatively small simulation cell (a 2 × 2 × 2 expansion of the PuO_2 unit cell, named the supercell, is shown Figure 2.10) which is repeated infinitely through space using periodic boundary conditions. This means that the point defect is repeated periodically, resulting in an undesirable interaction between the defect's periodic image that impacts upon the defect formation energy calculated, particularly if the defect is charged. These interactions include Coulombic interactions between the defect and its periodic image as well as with the background charge. The result is that defect formation energies exhibit a strong dependence on the size of the supercell used and this must be corrected for. Various methods of correction exist, and will be introduced in later chapters.

To describe the lattice position and electric charge of point defects, this thesis will follow convention and use Kröger-Vink notation [85], with modifications:

$\mathbf{D}_{\mathbf{S}}^{\mathbf{C}}$

D The defect species. Can be atoms, carriers (electrons or holes), or a vacancy (V).

S The lattice site. Can be an atomic site, or an interstice (i).

C The charge of the species, relative to the site it occupies. Displayed as a integer value, unless no charge, which is indicated by: ×.

2.5.2 Defect equilibria

Defect equilibria can be studied with thermodynamics by treating a compound with point defects as a solid solution where the point defects are dissolved in the solid. The formation (or removal) of a point defect is accompanied by a change

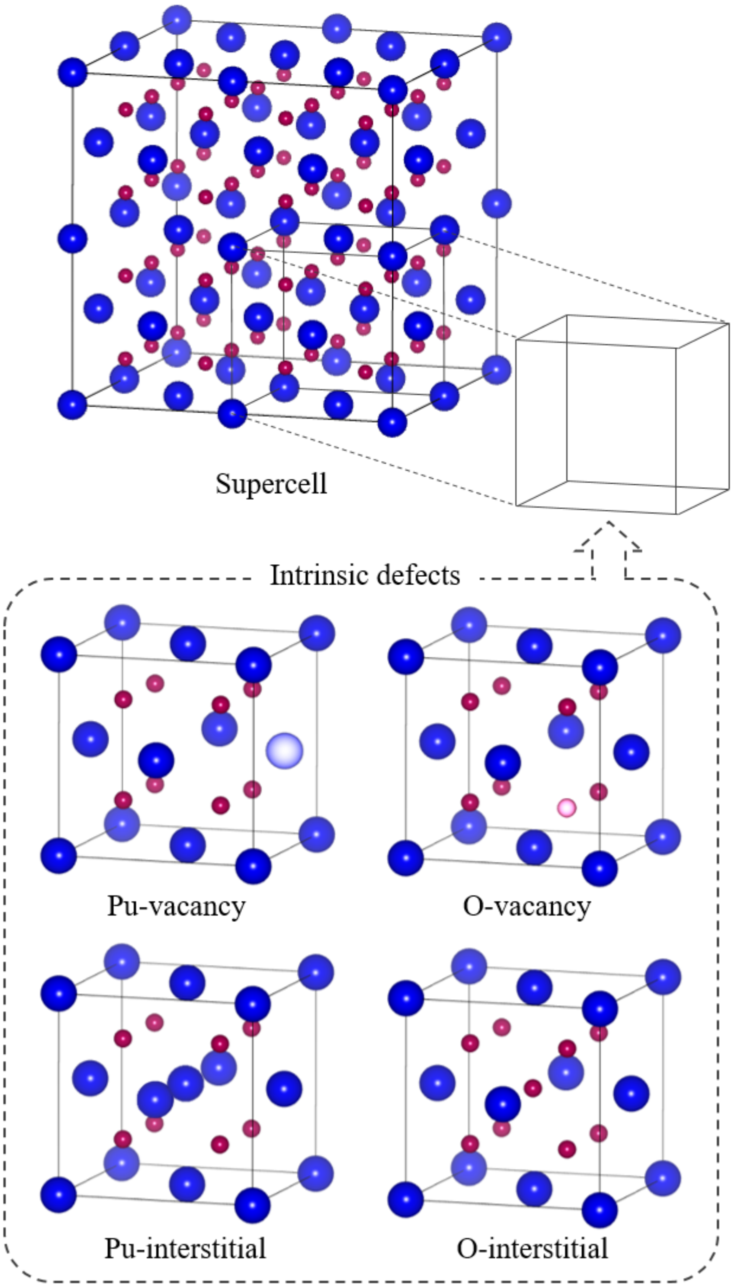

Figure 2.10: Illustration of the intrinsic defects in PuO_2. Plutonium and oxygen atoms are depicted with blue and red spheres, respectively. To simulate the defects using DFT, they are placed into a supercell, as depicted here using a $2 \times 2 \times 2$ supercell.

in the internal energy, ΔU, of the system, equal to the change in enthalpy, ΔH, if the system is at constant pressure. The accompanying change in disorder of the system is expressed with the change in entropy, ΔS. Introduction of defects into a crystal will increase ΔS, the ΔH necessary to form the defects limits their number. The actual number of defects present in a crystal at temperature T is governed by the change in Gibbs free energy of the system, ΔG, with equilibrium conditions achieved when $\Delta G = 0$:

$$\Delta G = \Delta H – T\Delta S \tag{2.22}$$

Consider a metal oxide, MO, with N metal (M) atoms in the starting material that forms n_v M vacancies. The M vacancies are formed by moving an M-atom from an M-site in the bulk to the surface of the compound, resulting in the total number of sites becoming $N + n_v$. For this system described, Equation 2.22 is adapted to become Equation 2.23.

$$\Delta G = n_v\Delta H – T(n_v\Delta S_{\text{vib}} + \Delta S_{\text{conf}}) = n_v(\Delta H – T\Delta S_{\text{vib}}) - T\Delta S_{\text{conf}} \tag{2.23}$$

The enthalpy change of forming n_v M vacancies is the term, $n_v\Delta H$, whilst the entropy change is divided into two parts: a vibrational entropy change, ΔS_{vib}, and a configurational entropy change, ΔS_{conf}. ΔS_{vib} represents the entropy that each individual vacancy creates; the term is multiplied to reflect the total vibrational entropy change, $n_v\Delta S_{\text{vib}}$. ΔS_{conf} considers the distribution of the vacancies in the system; as the number of defects increases, so does the number defect configurations (arrangements) within the crystal. Here, defect concentrations must be small so that interactions between defects are negligible and the terms ΔH and ΔS_{vib} are constant. ΔS_{conf} can be obtained from the Boltzmann relation,

$$\Delta S_{\text{conf}} = k_B \ln W \tag{2.24}$$

where k_B is Boltzmann's constant and W is the number of distinguishable ways of arranging n_v vacancies on $N + n_v$ sites:

$$W = \frac{(N + n_v)!}{N! n_v!} \tag{2.25}$$

Equations 2.24 and 2.25 combined:

$$\Delta S_{\text{conf}} = k_B \left(\ln(N + n_v)! - \ln(N!) - \ln(n_v!)\right) \tag{2.26}$$

If n_v and N are sufficiently large, Stirling's approximation ($\ln x! = x \ln x - x$) can be applied to Equation 2.26 to give,

$$\Delta S_{\text{conf}} = k_B \left(N \ln \frac{N + n_v}{N} + n_v \ln \frac{N + n_v}{n_v}\right) \tag{2.27}$$

which inserted into Equation 2.23 gives,

$$\Delta G = n_v(\Delta H – T\Delta S_{\text{vib}}) - k_B T \left(N \ln \frac{N + n_v}{N} + n_v \ln \frac{N + n_v}{n_v}\right) \tag{2.28}$$

At thermodynamic equilibrium ΔG is at a minimum. Consequently, the first derivative of Equation 2.28 with respect to n_v is equal to zero:

$$\frac{d\Delta G}{dn_v} = \Delta H – T\Delta S_{\text{vib}} + k_B T \ln \frac{n_v}{N + n_v} = 0 \tag{2.29}$$

$n_v/(N + n_v)$ represents the fraction of total sites that are M vacancies, i.e. the concentration. By rearranging Equation 2.29 it is possible to derive an expression for this term:

$$\frac{n_v}{N + n_v} = \exp\left(\frac{\Delta S_{\text{vib}}}{k_B}\right) \exp\left(\frac{-\Delta H}{k_B T}\right) \tag{2.30}$$

It is possible to construct an analogous derivation for each type of point defect.

2.5.3 Vibrational entropy

It is common when creating a point defect model from first principles to assume that the Gibbs free energy to form a defect can be well approximated without consideration of the vibrational entropy contribution. Recent work by Cooper *et al.* [86] and Soulié *et al.* [87] on UO_2 has shown that it is only by including the change in vibrational entropy due to defect incorporation that it is possible to reproduce the defect chemistry observed in experiment. UO_2 experiences deviation is its perfect stoichiometry with a consensus that the deviations are accommodated by oxygen-type defects. However, in what is described as the "uranium vacancy problem", DFT consistently predicts that uranium vacancies are the dominant defect in UO_{2+x} [86, 88]. The vibrational entropy term introduces instability in uranium vacancies at high temperatures; oxygen interstitials were then favoured as the accommodation of small hyper-stoichiometry [86]. Larger values of hyper-stoichiometry have been found to be accommodated by clusters of oxygen interstitials [87].

The vibrational entropy of a lattice is a function of its phonon frequencies; determined through force calculations associated with the displacements of atoms from their ground state positions. This becomes a very large calculation when defects are introduced, due to the removal of symmetry. The vibrational entropies for systems such as UO_2 and PuO_2 are, therefore, infeasible to calculate using DFT. Cooper *et al.* [86] and Soulié *et al.* [87] successfully demonstrated that empirical pair potentials can be used to perform the vibrational calculations. Vibrational entropies, S_{vib}, can be calculated using Equation 2.31, where, closely following the approach described in Refs. [86, 89, 90], defect entropies are calculated from the normal vibrational frequencies, v_{n}, which are themselves calculated by diagonalising the dynamical matrix of the system.

$$S_{\mathrm{vib}} = -k_{\mathrm{B}} \sum_{n=1}^{3N-1} ln \left(\frac{hv_{\mathrm{n}}}{k_{\mathrm{B}}T} \right) + (3N-3)k_{\mathrm{B}} \tag{2.31}$$

In this formula, h is Planck's constant, N is the number of atoms in the crystal and k_{B} is the Boltzmann constant. Given that the vibrational entropy of a system is temperature dependent, S_{vib} needs to be obtained at conditions representative of where the material resides.

Chapter 3

The Defect Analysis Package

This work is published in:

W.D. Neilson and S.T. Murphy, “DefAP: A Python code for the analysis of point defects in crystalline solids”, *Computational Materials Science*, vol 210, pp. 111434, 2022. [91]

3.1 Introduction

A fundamental objective and requirement of this thesis is to be able to determine the defect concentrations in PuO_2 and how the presence of these defects may modify the properties of the material. While there are a wide array of experimental techniques that are able to infer the presence of different types of defects in a material, an estimation of their concentration is still challenging. In recent years, the dramatic increase in computational power has enabled the study of point defects in materials using DFT [92]. Such simulations are now routine and an excellent guide is given by Kim *et al* [93]. When the supercell methodology is employed (introduced and illustrated in Section 2.5.1) a DFT simulation of a defect in a relatively small supercell is performed allowing the calculation of an energy. In order to gain useful physical insight this energy must be combined with thermodynamics to adequately describe the material's environment. This is crucial as the concentration of a defect in a material will depend on factors including the availability of atoms/ions, temperature, pressure etc. Given the defect concentrations are not constant this further implies that there is no single value for the defect formation energy — they too depend on these factors. Therefore, what is required is a convenient method for linking the results of DFT simulations with appropriate thermodynamics.

The Defect Analysis Package (DefAP), an open-source Python code, has been developed to facilitate the exploration of a material's defect chemistry, connecting the results of DFT calculations with bespoke, user-customised thermodynamics and processing operations that can be tailored to any defect-containing system of interest (Figure 3.1). At its core, DefAP is designed to calculate defect formation energies and concentrations under a range of different experimental conditions, with finite-size effects (due to small simulation cells) mitigated with the optional use of a point charge correction that is applicable to both isotropic and anisotropic systems.

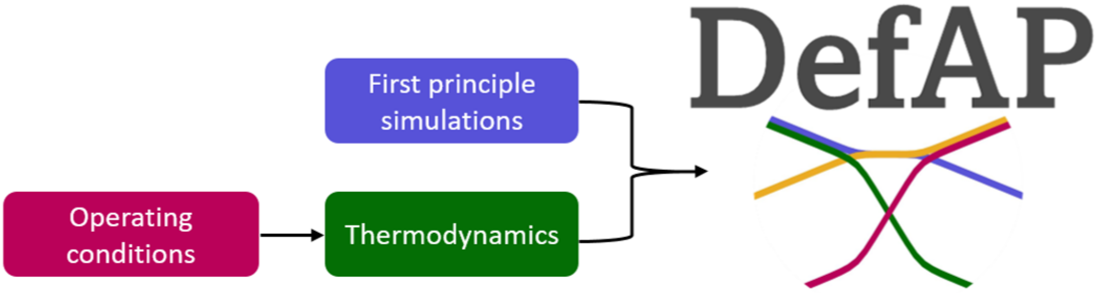

Figure 3.1: The Defect Analysis Package

Alternative codes are available that offer post-treatment of defect-DFT calculations. Some focus on the evaluation of a defect's formation energy [94, 95], whilst the codes Spinney [96], PyDEF-2.0 [97] and SC-FERMI [98] also offer the capability to calculate carrier and defect concentrations. This chapter outlines the enhanced capabilities that makes DefAP an attractive alternative to these codes. DefAP is designed to be user friendly; uniquely, it can perform the calculation of the formation energy of multiple defects and their corresponding equilibrium concentrations as a function of a chosen environmental variable in one single operation, with automatic production of attractive, publication quality plots, using gnuplot.

Examples of the user-customisable methodology include the choice of method to calculate carrier concentrations (to suit the system being studied), the modelling of chemical potential temperature dependence using a real gas model, and the option to consider the change in vibrational entropy due to the defect when calculating the defect's formation energy. The ability to study controlled quantities of multiple dopant species is available, where DefAP determines the chemical potential of each dopant element that delivers the user-defined concentration of each dopant species. This is possible for multiple dopant elements for the first time, due to the nonlinear optimiser designed in the code.

Section 3.2 outlines the methodology and formalism of the DefAP code, before the capabilities and usage of the code is demonstrated in Section 3.3, with use of example systems. DefAP will then be used to study PuO_2 in later chapters.

3.2 Methodology

This section details the scientific principles that DefAP uses throughout its calculations. The superscript 'DFT' is used to denote terms that would be obtained by the user using a DFT code; DefAP is not tied to one specific code (VASP, CASTEP, etc.) but one code must of course be used consistently. A manual is available that provides a comprehensive description of how a user would operate DefAP, available online (https://github.com/DefAP/defap).

Point defects, e.g. vacancies, interstitials, and substitutionals, are crystallographic defects that occur at or around a single lattice point. Assuming that the number of point defects is small compared to the number of lattice sites in the crystal, the equilibrium concentration, c_i, of defect i can be related to the change in the Gibbs free energy, $\Delta G_{\mathrm{f}}^{\mathrm{i}}$, to form the defect, i. This relationship was derived in Section 2.5.2:

$$c_i = m_i \mathrm{exp}\left(\frac{-\Delta G_{\mathrm{f}}^{i}}{k_{\mathrm{B}}T}\right) \tag{3.1}$$

where, m_i is the multiplicity of equivalent sites. Equation 3.1 is derived assuming that defect concentrations are small, where interactions between defects are negligible. The energies of the perfect and defective cells are used to define $\Delta G_{\mathrm{f}}^{\mathrm{i}}$ as:

$$\Delta G_{\mathrm{f}}^{i} = E_{\mathrm{defect}}^{\mathrm{DFT}} - E_{\mathrm{perfect}}^{\mathrm{DFT}} - T\Delta S_{\mathrm{vib}} \pm \sum_{\alpha} n_{\alpha}\mu_{\alpha} + q_{\mathrm{i}}\mu_{\mathrm{e}} + E_{\mathrm{corr}} \tag{3.2}$$

$E_{\mathrm{defect}}^{\mathrm{DFT}}$ and $E_{\mathrm{perfect}}^{\mathrm{DFT}}$ are the DFT total energies of the system with and without the defect, i. ΔS_{vib} is the difference in vibrational entropy between defective and perfect supercells and is discussed in Section 3.2.3. The contribution of vibrational entropy to the defect formation energy is significant and should not be neglected, especially at high temperatures. The contribution can however be neglected if desired, and it is widely considered safe to do so at relatively low temperatures. If neglected, the term $\Delta G_{\mathrm{f}}^{\mathrm{i}}$ is replaced with $\Delta E_{\mathrm{f}}^{\mathrm{i}}$. n_{α} is the number of atoms of species, α, added to or removed from the system to make defect i, μ_{α} is the chemical potential of species α. q_i is the charge of the defect i and $\mu_{\mathrm{e}} = E_{VBM} + \varepsilon_{\mathrm{F}}$: E_{VBM} is the energy of the valence band maximum (VBM) and ε_{F} is the electron chemical potential above the VBM. E_{corr} is an optional correction used to mitigate charge interactions of the defect charges with their periodic images. There have been a large number of charge corrections developed [99, 100, 101, 102, 103, 104, 105], however, many of these require the further examination of the output from DFT calculation of each defect. The resulting corrections can be input manually or DefAP offers the ability to automatically include a point charge correction, as discussed in Section 3.2.4.

More recently Kasamatsu *et al.* [106] have derived a more complex expression for the concentration of a given defect, which includes the interactions of defects competing for the same lattice sites, that is:

$$c_i = m_i \frac{\exp\left(\frac{-\Delta E_{\mathrm{f}}^{i}}{k_{\mathrm{B}}T}\right)}{1 + \sum\limits_j \exp\left(\frac{-\Delta E_{\mathrm{f}}^{j}}{k_{\mathrm{B}}T}\right)} \tag{3.3}$$

where, the sum in the denominator is performed over all defects that occupy the same lattice site as defect i. DefAP allows choice of the expression used to calculate defect concentrations, at low defect concentrations (i.e. when $\Delta E_{\mathrm{f}} << k_{\mathrm{B}}T$) the two expressions converge as there is little competition for lattice sites.

A key design principle of the code is the ability to, in a single operation, evaluate a material's defect chemistry over a range of conditions. DefAP evaluates Equations (3.1 or 3.3) & 3.2 at $iterations$ taken between a $minimum$ and $maximum$ value of a $property$ (where italicised values are user-defined). The properties that can be selected are either (1) the partial pressure of a volatile species, (2) temperature, (3) the concentration of a dopant, or (4) the concentration of an artificial dopant. Dopants are discussed in Section 3.2.5.

3.2.1 Chemical potentials

DefAP contains several mechanisms to either input or calculate the chemical potentials of the elements in the system under study. The user must select one of the four mechanisms implemented in DefAP, based upon the nature of the system studied. The first of these four mechanisms is appropriate for the study of simple systems such as semiconductors (e.g. Si) where the chemical potentials are calculated using DFT or other external means, and supplied in the input file. The only requirement to using this mechanism is that the defined chemical potentials for the constituent elements, as entered, add up to that for the host system, a check that is performed by DefAP. Using $\mathrm{M}_\alpha\mathrm{N}_\beta$ as an example, the following criteria must be met:

$$\alpha\mu_{\mathrm{M}_{(\mathrm{s})}} + \beta\mu_{\mathrm{N}_{(\mathrm{s})}} = \mu^{\mathrm{DFT}}_{\mathrm{M}_\alpha\mathrm{N}_{\beta(\mathrm{s})}} \tag{3.4}$$

The second mechanism, used for systems that contain multiple metal species, enables the exploration of the defect chemistry under conditions that contain either an excess or deficit of each of the species (referred to here as rich and poor conditions, respectively). Again, using the example system $\mathrm{M}_\alpha\mathrm{N}_\beta$, the rich condition for each specie is determined using DFT, i.e.:

$$\mu^{\mathrm{M-rich}}_{\mathrm{M}} = \mu^{\mathrm{DFT}}_{\mathrm{M}_{(\mathrm{s})}} \tag{3.5}$$

To calculate the chemical potential of each element under poor conditions, it is assumed all other elements are defined to be in their rich condition, for example:

$$\mu^{\mathrm{M-poor}}_{\mathrm{M}} = \frac{\mu^{\mathrm{DFT}}_{\mathrm{M}_\alpha\mathrm{N}_{\beta(\mathrm{s})}} - \beta\mu^{\mathrm{DFT}}_{\mathrm{N}_{(\mathrm{s})}}}{\alpha} \tag{3.6}$$

There is therefore now a range in the chemical potential for each element, from poor to rich conditions. To access intermediate compositions a fraction is defined, f, for each metal in the system which is used to calculate the chemical potential of each element, e.g.:

$$\mu^{f}_{\mathrm{M}} = f\mu^{\mathrm{M-rich}}_{\mathrm{M}} + (1-f)\mu^{\mathrm{M-poor}}_{\mathrm{M}} \tag{3.7}$$

A limitation is placed on the possible fractions, f, assigned to each element:

$$\sum_j f^j = n - 1 \tag{3.8}$$

where n is the number of metal elements in the system. For the example system discussed here, $\mathrm{M}_\alpha\mathrm{N}_\beta$, n equals 2, necessitating that $f^M + f^N = 1$. If f^M is set to equal 1, the system would be M-rich meaning that $f^N = 0$ and so the system would be at the N-poor limit.

Compounds containing an element that is in the gas phase in its standard state are systems routinely subject to defect chemistry studies. For such compounds that are binary, the third mechanism is designed to calculate the chemical potential of both constituent elements. These are expressed generally as $\mathrm{M}_\alpha\mathrm{V}_\beta$, where V is a volatile element that exists naturally as a binary gas molecule (O, N, H, Cl and F are common examples that could be V). The chemical potential of V is dependent on the partial pressure of V and on temperature, which results in the chemical potential of M depending on these variables too. To calculate the chemical potentials of the elements in this type of system, DefAP begins by decomposing the binary compounds into their constituents, for example for $\mathrm{M}_\alpha\mathrm{V}_\beta$:

$$\alpha\mu_{\mathrm{M}_{(\mathrm{s})}} + \beta\mu_{\mathrm{V}}(P_{\mathrm{V}_2}, T) = \mu^{\mathrm{DFT}}_{\mathrm{M}_\alpha\mathrm{V}_{\beta(\mathrm{s})}} \tag{3.9}$$

To determine the chemical potential of V the approach of Finnis *et al.* [107] is adopted. This method uses the known formation energy of the binary compound under standard conditions, $\Delta G_{\mathrm{f}}^{\mathrm{M}_\alpha\mathrm{V}_\beta}(P^\circ_{\mathrm{V}_2}, T^\circ)$, to obtain the chemical potential of V at standard temperature and pressure:

$$\Delta G_{\mathrm{f}}^{\mathrm{M}_\alpha\mathrm{V}_\beta}(P^\circ_{\mathrm{V}_2}, T^\circ) = \mu^{\mathrm{DFT}}_{\mathrm{M}_\alpha\mathrm{V}_{\beta(\mathrm{s})}} - \alpha\mu^{\mathrm{DFT}}_{\mathrm{M}_{(\mathrm{s})}} - \beta\mu_{\mathrm{V}}(P^\circ_{\mathrm{V}_2}, T^\circ) \tag{3.10}$$

The chemical potential of V at the desired conditions, $\mu_{\mathrm{V}}(P_{\mathrm{V}_2}, T)$, is extrapolated from $\mu_{\mathrm{V}}(P^\circ_{\mathrm{V}_2}, T^\circ)$ using Equation 3.11:

$$\mu_{\mathrm{V}}(P_{\mathrm{V}_2}, T) = \mu_{\mathrm{V}}(P^\circ_{\mathrm{V}_2}, T^\circ) + \Delta\mu(T) + \frac{1}{2}k_{\mathrm{B}}T\log\left(\frac{P_{\mathrm{V}_2}}{P^\circ_{\mathrm{V}_2}}\right) \tag{3.11}$$

$\Delta\mu(T)$ represents the temperature contribution to the chemical potential. DefAP contains two different approaches for the user to choose when calculating this contribution; the first option is to treat V_2 as a rigid-dumbbell ideal gas and use the following equation:

$$\Delta\mu(T) = -\frac{1}{2}(S^{\circ}_{\mathrm{V}_2} - C^{\circ}_P) + C^{\circ}_P T \log\left(\frac{T}{T^{\circ}}\right) \tag{3.12}$$

where $S^{\circ}_{\mathrm{V}_2}$ is the molecular entropy at standard temperature and pressure and C°_P is the constant pressure heat capacity of V_2. The values DefAP uses for these two properties are taken from the National Institute of Standards and Technology (NIST) Chemistry WebBook [108]; O_2, N_2, H_2, Cl_2 and F_2 are the implemented options. The alternative option is to calculate $\Delta\mu(T)$ using the real heat capacities of the V_2 molecule and employ the Shomate equations:

$$\Delta\mu(T) = \frac{1}{2}(G(P^{\circ},T) - G(P^{\circ},T^{\circ})) \tag{3.13}$$

where,

$$G(P^{\circ},T) = H(P^{\circ},T) - TS(P^{\circ},T) \tag{3.14}$$

$$H(P^{\circ},T) = 1000(At + \frac{1}{2}Bt^2 + \frac{1}{3}Ct^3 - \frac{1}{4}Dt^4 - \frac{E}{t} + F - H) \tag{3.15}$$

$$S(P^{\circ},T) = A\ln(t) + Bt + \frac{1}{2}Ct^2 + \frac{1}{3}Dt^3 - \frac{E}{2t^2} + G \tag{3.16}$$

$$t = \frac{T(K)}{1000} \tag{3.17}$$

Equations 3.15-3.17 and the temperature-dependent parameters $A - G$ are taken from the NIST Chemistry WebBook [108]. Again, O_2, N_2, H_2, Cl_2 and F_2 are the implemented options. Alternative Shomate equations and parameters $A-G$, taken from Johnston *et al.* [109], are also implemented for O_2 and available within the program.

The final mechanism implemented in DefAP is designed to calculate the chemical potential of constituent elements in systems containing a volatile element and multiple metal species, i.e. a non-binary volatile compound. To do this, the compound is deconstructed into binary volatile compounds that could be assumed to thermodynamically construct the original compound. Using the compound $\mathrm{M}_\alpha\mathrm{N}_\beta\mathrm{V}_\gamma$ as an example, where V is the volatile element, it can be said:

$$\mathrm{AM}_\delta\mathrm{V}_{\epsilon\mathrm{(s)}} + \mathrm{BN}_\zeta\mathrm{V}_{\eta\mathrm{(s)}} + \frac{1}{2}\mathrm{CV}_{2\mathrm{(g)}} \rightarrow \mathrm{M}_\alpha\mathrm{N}_\beta\mathrm{V}_{\gamma\mathrm{(s)}} \tag{3.18}$$

where,

$$\delta\mathrm{A} = \alpha \tag{3.19}$$

$$\zeta\mathrm{B} = \beta \tag{3.20}$$

$$\epsilon\mathrm{A} + \eta\mathrm{B} + \mathrm{C} = \gamma \tag{3.21}$$

Under any given conditions, the sum of the chemical potentials per formula unit of the constituent species must be equal to the total Gibbs free energy of the host compound, i.e. in this example:

$$\mathrm{A}\mu_{\mathrm{M}_\delta\mathrm{V}_\epsilon}(P_{\mathrm{V}_2}, T) + \mathrm{B}\mu_{\mathrm{N}_\zeta\mathrm{V}_\eta}(P_{\mathrm{V}_2}, T) + \mathrm{C}\mu_{\mathrm{V}}(P_{\mathrm{V}_2}, T) = \mu_{\mathrm{M}_\alpha\mathrm{N}_\beta\mathrm{V}_{\gamma(s)}} \tag{3.22}$$

Under standard conditions it is assumed that $\mu_{\mathrm{M}_\alpha\mathrm{N}_\beta\mathrm{V}_\gamma}(P_{\mathrm{V}_2}, T) = \mu_{\mathrm{M}_\alpha\mathrm{N}_\beta\mathrm{V}_{\gamma(s)}}$, where the chemical potential of $\mathrm{M}_\alpha\mathrm{N}_\beta\mathrm{V}_\gamma$ is calculated using DFT. Under equilibrium conditions, the chemical potentials of the constituents of a crystal cannot exceed the Gibbs free energy of any phase made of the constituent elements. For example, the chemical potential of $\mathrm{M}_\delta\mathrm{V}_\epsilon$ in $\mathrm{M}_\alpha\mathrm{N}_\beta\mathrm{V}_\gamma$ cannot exceed that of solid $\mathrm{M}_\delta\mathrm{V}_\epsilon$, otherwise a $\mathrm{M}_\delta\mathrm{V}_\epsilon$ precipitate would form. The approach DefAP adopts to find the chemical potentials is to set upper and lower bounds for each binary compound that is selected in Equation 3.18. However there may be many other possible phases that the host compound could decompose into, in addition to the binary compounds in Equation 3.18. Functionality exists in DefAP to examine the stability of these competing phases and is discussed later in this section. Returning to the determination of chemical potentials, the upper bound for the chemical potential of each binary compound is set using DFT, using $\mathrm{M}_\delta\mathrm{V}_\epsilon$ as an example:

$$\mu_{\mathrm{M}_\delta\mathrm{V}_\epsilon}^{\mathrm{M}_\delta\mathrm{V}_\epsilon-\mathrm{rich}} = \mu_{\mathrm{M}_\delta\mathrm{V}_{\epsilon(\mathrm{s})}}^{\mathrm{DFT}} \tag{3.23}$$

To calculate the lower bound for the chemical potential each binary compound, it is assumed all other binary compounds must be at their upper bound and thus:

$$\mu_{\mathrm{M}_\delta\mathrm{V}_\epsilon}^{\mathrm{M}_\delta\mathrm{V}_\epsilon-\mathrm{poor}} = \frac{\mu_{\mathrm{M}_\alpha\mathrm{N}_\beta\mathrm{V}_{\gamma(\mathrm{s})}}^{\mathrm{DFT}} - \mathrm{B}\mu_{\mathrm{N}_\zeta\mathrm{V}_{\eta(\mathrm{s})}}^{\mathrm{DFT}} - \mathrm{C}\mu_{\mathrm{V}}(P_{\mathrm{V}_2}, T)}{\mathrm{A}} \tag{3.24}$$

The values for the chemical potentials can fall anywhere in this rich/poor range, therefore a fraction, f, is defined for each binary compound which controls where in this range the chemical potential falls:

$$\mu_{\mathrm{M}_\delta\mathrm{V}_\epsilon}^{f} = f\mu_{\mathrm{M}_\delta\mathrm{V}_\epsilon}^{\mathrm{M}_\delta\mathrm{V}_\epsilon-\mathrm{rich}} + (1-f)\mu_{\mathrm{M}_\delta\mathrm{V}_\epsilon}^{\mathrm{M}_\delta\mathrm{V}_\epsilon-\mathrm{poor}} \tag{3.25}$$

The fractions, f, assigned to each binary compound must be such that Equation 3.8 is obeyed. The calculated chemical potentials of the binary oxides are further decomposed into the constituent elements according to the method outlined previously using Equations 3.9-3.17. This method calculates a chemical potential of V at standard temperature and pressure ($\mu_{\mathrm{V}}(P_{\mathrm{V}_2}^{\circ}, T^{\circ})$) for each binary compound selected in Equation 3.18. A final value of $\mu_{\mathrm{V}}(P_{\mathrm{V}_2}^{\circ}, T^{\circ})$ is calculated by DefAP as a weighted average of the contributions by the fractions of binary compounds present:

$$\mu_{\mathrm{V}}(P_{\mathrm{V}_2}^{\circ}, T^{\circ}) = \frac{1}{n-1}\sum_j f^j \mu_{\mathrm{V}}^j(P_{\mathrm{V}_2}^{\circ}, T^{\circ}) \tag{3.26}$$

Thermodynamic stability

As discussed throughout this section, DefAP relies on the DFT energies of reference compounds to calculate the chemical potentials of each compounds constituent elements. This approach ensures that each of the selected reference compounds are thermodynamically stable with respect to the host system; using $\mathrm{M}_\alpha\mathrm{V}_\gamma$ as an example of a reference compound in the host sytem, $\mathrm{M}_\alpha\mathrm{N}_\beta\mathrm{V}_\gamma$, Equation 3.27 is satisfied:

$$\alpha\mu_{\mathrm{M}_{(\mathrm{s})}} + \gamma\mu_{\mathrm{V}}(P_{\mathrm{V}_2}, T) \leq \mu^{\mathrm{DFT}}_{\mathrm{M}_\alpha\mathrm{V}_{\gamma(\mathrm{s})}} \tag{3.27}$$

However, many systems will posses a multitude of possible compounds, not used as a reference compound, that the host system could potentially decompose to under specific conditions. DefAP offers the capability to predict the stability of the system with respect to any number of compounds under the range of conditions investigated. For example, the criteria for the stability of $\mathrm{M}_\alpha\mathrm{N}_\beta\mathrm{V}_\gamma$ with respect to $\mathrm{M}_2\mathrm{V}_3$ would be that:

$$2\mu_{\mathrm{M}_{(\mathrm{s})}} + 3\mu_{\mathrm{V}}(P_{\mathrm{V}_2}, T) \leq \mu^{\mathrm{DFT}}_{\mathrm{M}_2\mathrm{V}_{3(\mathrm{s})}} \tag{3.28}$$

In this example, the user would supply the DFT energy of $\mathrm{M}_2\mathrm{V}_3$. If, after DefAP calculates $\mu_{\mathrm{M}_{(\mathrm{s})}}$ and $\mu_{\mathrm{V}}(P_{\mathrm{V}_2}, T)$ at a given condition, Equation 3.28 is not satisfied, a warning will be given. The user may then choose to appropriately adjust their defined position in chemical potential space or the requested environmental conditions. It must be noted that DefAP can only provide an indicator of the thermodynamic stability of a phase; a phase predicted to be unstable would not necessarily be able to overcome the kinetic barriers needed to form a secondary phase. It is for this reason a warning is given instead of terminating the program.

3.2.2 Electron and hole concentrations

In charged systems, the sum of the concentrations of ionic and electronic defects, each multiplied by their charges, must balance to provide overall charge neutrality. This can be expressed as:

$$\sum_{\mathrm{i}} q_{\mathrm{i}}c_{\mathrm{i}} - c_{e^-} + c_{p^+} = 0 \tag{3.29}$$

The first term is the sum of the charges of the point defects. The second and third terms correspond to the concentrations of electrons (e^-) and holes (p^+) respectively. DefAP offers the user several options to calculate the concentration of the electronic defects. The first of these options is to simply fix the concentrations at a desired value. The second option is to employ Boltzmann statistics, with use of Equations 3.30 and 3.31.

$$c_{e^-} = N_c \mathrm{exp}\left(-\frac{E_g - \varepsilon_F}{k_B T}\right) \tag{3.30}$$

$$c_{p^+} = N_v \mathrm{exp}\left(-\frac{\varepsilon_F}{k_B T}\right) \tag{3.31}$$

N_c and N_v are the effective conduction band and valence band DOS and E_g is the bandgap. The third option to calculate electronic defect concentrations is to apply Fermi-Dirac statistics to the electronic DOS to obtain the concentrations of e^- in the conduction band and concentration of holes p^+ in the valance band, respectively:

$$c_{e^-} = \int_{E_{\mathrm{CBM}}}^{\infty} g_{\mathrm{c}}(E) \frac{dE}{1 + \exp(\frac{E - \varepsilon_{\mathrm{F}}}{k_{\mathrm{B}} T})} \tag{3.32}$$

$$c_{p^+} = \int_{-\infty}^{E_{\mathrm{VBM}}} g_{\mathrm{v}}(E) \frac{dE}{1 + \exp(\frac{\varepsilon_{\mathrm{F}} - E}{k_{\mathrm{B}} T})} \tag{3.33}$$

$g_{\mathrm{c}}(E)$ and $g_{\mathrm{v}}(E)$ are the density of electronic states in the conduction band and valence band, respectively. E_{CBM} is the energy of the conduction band minimum. The use of Fermi-Dirac statistics is advocated over Boltzmann statistics owing to the direct utilisation of the system's DOS. A fourth option, particularly useful for the study of semiconductors, is to return to Equations 3.30 and 3.31 but to transform N_c and N_v to the DOS effective mass of electrons and holes, respectively. N_c and N_v are now calculated using the following equations:

$$N_c = 2\left(\frac{2\pi m_e^* k_B T}{h^2}\right)^{\frac{3}{2}} \tag{3.34}$$

$$N_v = 2\left(\frac{2\pi m_p^* k_B T}{h^2}\right)^{\frac{3}{2}} \tag{3.35}$$

m_e^* and m_p^* are the electron and hole effective mass in the chosen semiconductor, respectively. h is Planck's constant. The final option is to treat the electrons and holes in the same manner as all other defects in the system, performing a full structural relaxation of each. The merits of this approach are described by Cooper *et al.* [86].

Altogether, in charged systems, there remains one variable in Equation 3.29 that DefAP is designed to compute: the Fermi level that achieves charge neutrality. Linear bisection is employed, using the sub-process illustrated in Figure 3.2, to find the solution. The convergence criteria for charge neutrality is set by default to be very low ($< 10^{-10}u$), but can be adjusted by the user to further increase accuracy as detailed in the manual. DefAP also checks that the Fermi level computed falls within the bandgap.

3.2.3 Vibrational entropy

DefAP enables the consideration of the difference in vibrational entropy between defective and perfect supercells when evaluating the formation energy of each defect. The vibrational entropy of a system is temperature dependent, therefore DefAP uses interpolation to calculate the vibrational entropy of the system at the desired temperature. This requires the user to gather the vibrational entropy of defective and perfect systems at several temperature values. At the time of writing, phonon calculations of defect-containing supercells are very expensive in DFT. A successful strategy adopted in past studies has seen empirical potentials used to calculate vibrational entropies, as described in Section 2.5.3. In addition to the inclusion of the vibrational entropy term in Equation 3.2, if the chemical potentials have dependence on temperature (i.e. a volatile element is in the system), modifications are made to the method that chemical potentials are calculated. Using

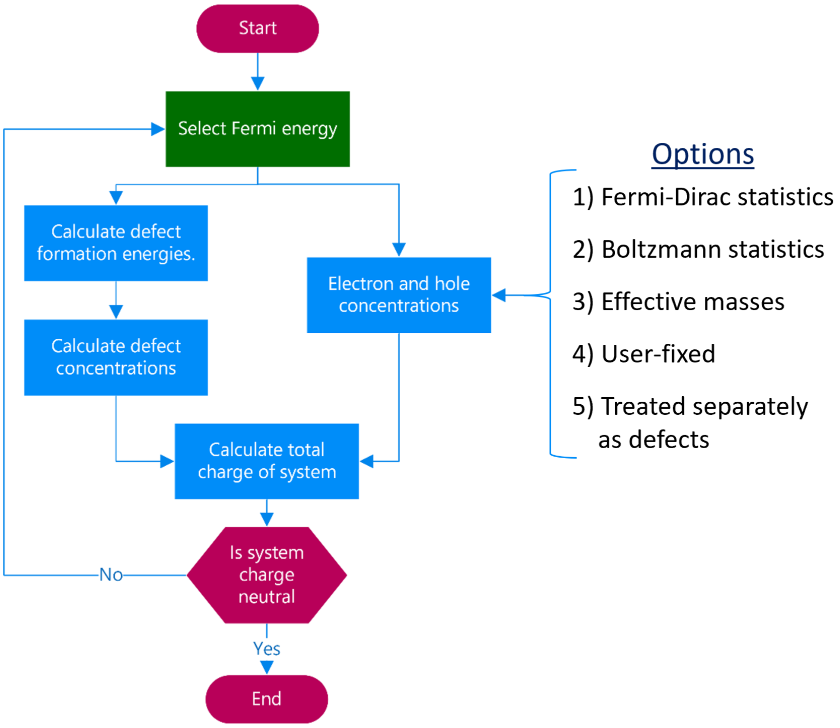

Figure 3.2: Sub-process designed in DefAP to compute the Fermi energy that achieves a charge neural system.

$S_x(T)$, the vibrational entropy of compound x at temperature T, Equation 3.9 is modified to:

$$\alpha\mu_{\mathrm{M}_{(s)}} + \beta\mu_{\mathrm{V}}(P_{\mathrm{V}_2}, T) = \mu^{\mathrm{DFT}}_{\mathrm{M}_\alpha\mathrm{V}_{\beta(s)}} - TS_{\mathrm{M}_\alpha\mathrm{V}_{\beta(s)}}(T) \tag{3.36}$$

Equations 3.23 and 3.24, employed when studying non-binary volatile compounds, are modified to Equations 3.37 and 3.38, respectively.

$$\mu^{\mathrm{M}_\delta\mathrm{V}_\epsilon-\mathrm{rich}}_{\mathrm{M}_\delta\mathrm{V}_\epsilon} = \mu^{\mathrm{DFT}}_{\mathrm{M}_\delta\mathrm{V}_{\epsilon(s)}} - TS_{\mathrm{M}_\delta\mathrm{V}_{\epsilon(s)}}(T) \tag{3.37}$$

$$\begin{aligned} \mu^{\mathrm{M}_\delta\mathrm{V}_\epsilon-\mathrm{poor}}_{\mathrm{M}_\delta\mathrm{V}_\epsilon} &= \frac{1}{\mathrm{A}}\Big(\mu^{\mathrm{DFT}}_{\mathrm{M}_\alpha\mathrm{N}_\beta\mathrm{V}_{\gamma(s)}} - TS_{\mathrm{M}_\alpha\mathrm{N}_\beta\mathrm{V}_{\gamma(s)}}(T) \\ &-\mathrm{B}\left(\mu^{\mathrm{DFT}}_{\mathrm{N}_\varsigma\mathrm{V}_{\eta(s)}} - TS_{\mathrm{N}_\varsigma\mathrm{V}_{\eta(s)}}(T)\right) - \mathrm{C}\mu_{\mathrm{V}}(P_{\mathrm{V}_2}, T)\Big) \end{aligned} \tag{3.38}$$

3.2.4 Finite size error corrections

The introduction of charged defects into the small simulation supercells accessible using DFT introduces a number of finite size effects as discussed extensively in Ref. [110]. These include Coulombic interactions between the defect and its periodic image as well as with the background charge. The result is that defect formation energies exhibit a strong dependence on the size of the supercell used and this must be corrected for. DefAP offers the option for externally calculated corrections for each defect to be supplied and used, or, alternatively the direct calculation and implementation of the correction for each defect. The charge correction that DefAP can calculate for a simple point charge is given as:

$$E_{\mathrm{corr}} = \frac{q^2 v_M^{scr}}{2} = \frac{q^2 \alpha}{2\epsilon L} \tag{3.39}$$

where, v_M^{scr} is the Madelung potential for a point charge in a general 3-dimensional box screened by a general dielectric. If the system is cubic, $v_M^{scr} = \frac{\alpha}{\varepsilon L}$, where $\alpha =$ 2.837, L is the length of the simulation supercell and ϵ is the material's dielectric constant. If studying a non-cubic system with anisotropic dielectric properties, DefAP can be used to calculate an appropriate value of v_M^{scr} for the system, using the systems dielectric tensor, $\bar{\epsilon}$, and the method described by Murphy and Hine [104]:

$$\begin{aligned} v_M^{scr} &= \sum_{\boldsymbol{R}_\mathrm{i}}^{i \neq 0} \frac{1}{\sqrt{\det \bar{\epsilon}}} \frac{\mathrm{erfc}(\gamma \sqrt{\boldsymbol{R}_i \cdot \bar{\epsilon}^{-1} \cdot \boldsymbol{R}_i})}{\sqrt{\boldsymbol{R}_i \cdot \bar{\epsilon}^{-1} \cdot \boldsymbol{R}_i}} \\ &+ \sum_{\boldsymbol{G}_\mathrm{i}}^{i \neq 0} \frac{4\pi}{V_c} \times \frac{\exp(-\boldsymbol{G}_i \cdot \bar{\epsilon} \cdot \boldsymbol{G}_i / 4\gamma^2)}{\boldsymbol{G}_i \cdot \bar{\epsilon} \cdot \boldsymbol{G}_i} - \frac{2\gamma}{\sqrt{\pi \det \bar{\epsilon}}} - \frac{\pi}{V_c \gamma^2} \end{aligned} \tag{3.40}$$

where the sum extends over all vectors of the direct ($\boldsymbol{R}_i$) and reciprocal ($\boldsymbol{G}_i$) lattices, γ is a suitably chosen convergence parameter, and V_c is the volume of the supercell.

3.2.5 Dopants and impurities

Many of the most interesting properties of materials arise due to the presence of foreign atoms in the host matrix, whether this is due to intentional doping or unintentionally such as accommodation of fission products in a nuclear fuel. When considering dopants there are two major factors to consider, the first is how the foreign atoms are incorporated into the lattice and second how does the presence of the foreign atom influence the intrinsic defect chemistry. There are two different methods for studying dopants in DefAP. The first and most simple is to introduce a concentration of defects with a given charge. In this case the type of defect that is incorporated is not important, however this allows the user to see how the introduction of say 1 ppm of a defect with a 1+ charge alters the concentrations of the intrinsic defects. The charge neutrality condition, Equation 3.29, is modified to accommodate the artificial presence of a dopant with concentration, c_D, and charge, q_D:

$$\sum_{\mathrm{i}} q_{\mathrm{i}} c_{\mathrm{i}} - c_{e^-} + c_{p^+} + c_D q_D = 0 \tag{3.41}$$

The advantage of this approach is that it does not require any further DFT data, however, there is no insight about how the foreign atoms are accommodated in the lattice. In the second approach, the dopant is included by considering its incorporation as a defect at different lattice sites using DFT, then calculating the formation energy of each considered defect with Equation 3.2. This approach requires the calculation of the chemical potential for the dopant. There are two possibilities for defining the chemical potential of the dopant, dependent on the source of the dopant. The first option considers a constant, unlimited source/reservoir, with the result being a description of how the host lattice incorporates the dopant from this reservoir. The dopant chemical potential, $\mu_{\mathrm{D}_{(\mathrm{s})}}$, is calculated from a supplied reference state compound; for example, $\mathrm{D}_\alpha \mathrm{V}_\beta$, containing the dopant element, D, and a volatile element present in the host system, V:

$$\mu_{\mathrm{D}_{(\mathrm{s})}} = \frac{\mu^{\mathrm{DFT}}_{\mathrm{D}_\alpha \mathrm{V}_{\beta(\mathrm{s})}} - \beta\mu_{\mathrm{V}}(P_{\mathrm{V}_2}, T)}{\alpha} \tag{3.42}$$

The reference state compound can be replaced with a reference dopant atom as appropriate for gasses, such as Xe. The second option for determining the dopant chemical potential is to define the total concentration of the dopant as a specified, restricted quantity that exists in the material. DefAP determines the dopant chemical potential and blend of dopant defects that delivers the desired concentration. This is a very useful method as often the concentration of a dopant under experimental conditions is known/desired and an inquiry exists regarding the accommodation of this concentration. Examples include semiconductors doped with specific concentrations of dopant elements or nuclear fuels containing known quantities of radiogenic impurities. If one dopant element is studied, DefAP uses linear bisection to find the chemical potential of the dopant that achieves the desired concentration, subject to the constraint that, if a charged system is being studied, the Fermi level is in the bandgap. DefAP can also study systems with multiple dopant elements, each with a specified concentration target. This becomes a nonlinear optimisation, therefore, sequential least squares programming (SLSQP) is deployed to find a solution, subject to the Fermi level constraint, described above. Figure 3.3 illustrates the program's architecture designed to predict the accommodation of n dopant species with a user-specified concentration. The thermodynamic stability of secondary phases that include elements of the dopant(s) can be investigated using the same methodology described in Section 3.2.1.

3.2.6 Stoichiometry deviation

When studying compounds that contain an element that is in the gas phase in its standard state, the ratio of this volatile element to the metal element(s) (or the stoichiometry) is of particular interest. Deviations in stoichiometry may have a

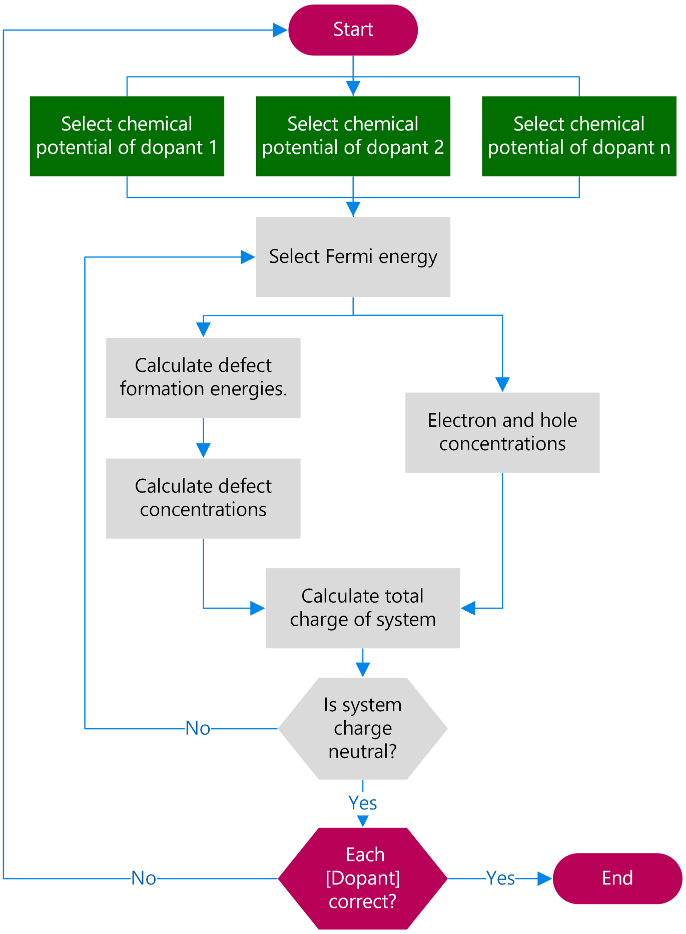

Figure 3.3: Sub-process designed in DefAP to compute the chemical potentials of n dopant species that achieve the user-requested concentration of each dopant. The grey tiles represent the Fermi energy sub-process, introduced in Figure 3.2.

significant impact upon the material properties, for example, the oxygen-to-metal ratios in metal oxide nuclear fuels are a critical parameter of performance. Small deviations in perfect stoichiometry can result from the formation of point defects; DefAP calculates the concentration of these defects, enabling a measurement and prediction of both the magnitude and cause of any deviation. No additional information is needed from the user, and the program is able to calculate the stoichiometry for both binary and non-binary compounds. Here, to aid description of the method DefAP uses to calculate any deviation, a binary compound, $\mathrm{M_{\alpha}V_{\beta\pm x}}$, can be considered where M is a metal element, V is the volatile element and x is the deviation from stoichiometry. Again, this represents a binary compound, but there may be multiple metal species if a non-binary compound is studied. To calculate the value of x, the compound of interest is rewritten in the form, $\mathrm{M_{\alpha+y}V_{\beta+z}}$, where y and z represent the surplus of M and V, as a result of the formation of defects, respectively. To calculate x, Equation 3.43 is used, where α and y are computed for each metal species, m.

$$\beta + \mathrm{x} = \frac{\beta + \mathrm{z}}{\sum_{\mathrm{m}} (\alpha + \mathrm{y})} \tag{3.43}$$

z and y are calculated using the predicted defect concentrations; the concentration of defects that involve the addition of the volatile element to the host contribute positively to z, conversely the concentration of defects that involve the removal of the volatile element are subtracted from z. y is the metal equivalent of z, but if the number of metal species in the host exceeds one, y is calculated for each species individually.

The addition of dopant/impurity element(s), D, to the host invokes reconsideration of the method used to calculate x in the compound $\mathrm{M_{\alpha}D_{w}V_{\beta\pm x}}$. If dopant defects are studied, two options are available to calculate the deviation in stoichiometry. The first is to retain use of Equation 3.43 which considers the cation/volatile species leaving the system as a consequence of the dopant addition when calculating z and y in $\mathrm{M_{\alpha+y}D_{w}V_{\beta+z}}$, but does not treat the dopant as a cation species, (i.e.

the value of w is insignificant). Alternatively, the second option treats the dopant species as metal species, with x in $\mathrm{M_{\alpha}D_{w}V_{\beta\pm x}}$ calculated using Equation 3.44 which includes the term w. w is calculated separately for each dopant species, d, and is the sum of the concentration of defects that include the dopant species.

$$\beta + \mathrm{x} = \frac{\beta + \mathrm{z}}{\sum_{\mathrm{m}} (\alpha + \mathrm{y}) + \sum_{\mathrm{d}} \mathrm{w}} \tag{3.44}$$

3.3 Example usage

This section highlights the capabilities of DefAP by studying the defect chemistry of three systems: Si, $\mathrm{YBa_2Cu_3O_7}$, and $\mathrm{Li_2TiO_3}$. The effect of P incorporation into Si, and both T and He in $\mathrm{Li_2TiO_3}$ is investigated to showcase the study of dopant defects. These systems help demonstrate the output of DefAP, however, a detailed investigation of each is not performed. DefAP operates according to user-requested `tasks`, most of which require data acquired from first-principle calculations performed on the system of interest. This data, as well as user defined information (such as the environmental conditions of interest) is collected in the DefAP input files. Figure 3.4 illustrates how DefAP operates, showing how operations performed are dependent on the `tasks` selected. DFT is employed to study the three example systems, the details of these simulations is compiled in Appendix A.

3.3.1 Silicon

To study intrinsic Si, the cubic diamond structure and the formation of both uncharged and charged vacancies and interstitials in several configurations is investigated. Three interstitial sites are studied: the tetrahedral ($\mathrm{Si_{i,T}}$), hexagonal ($\mathrm{Si_{i,H}}$), and the <110> dumbbell configuration ($\mathrm{Si_{i,110}}$), where two Si atoms share one atom site. As well as the conventional vacancy, where one Si atom is removed from the perfect lattice ($\mathrm{V_{Si,L}}$), a split vacancy is also considered, where a Si atom

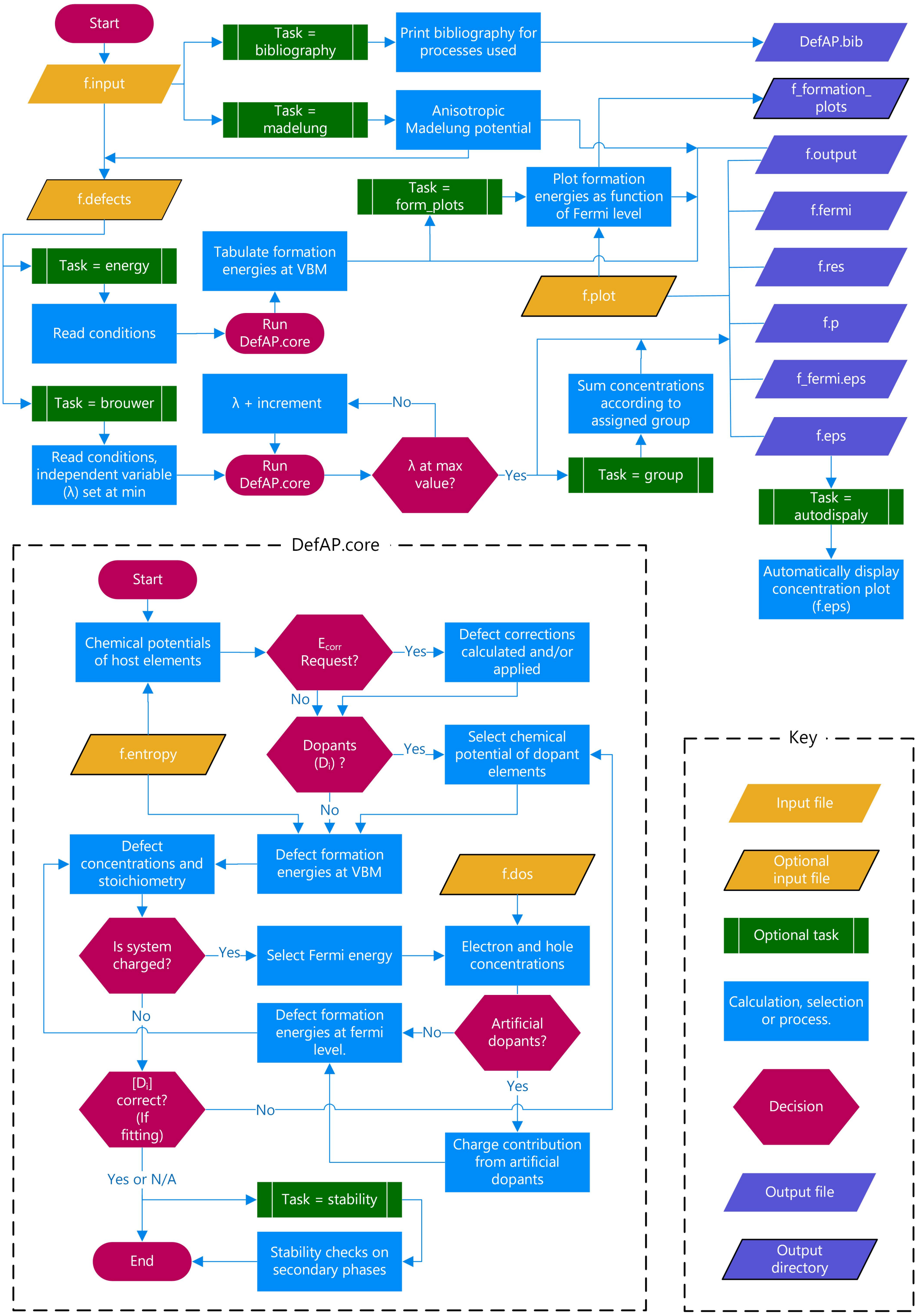

Figure 3.4: DefAP flow diagram

sits between two empty sites ($V_{\mathrm{Si,B}}$). The carrier concentration is of particular importance within semiconductor materials; the option available in DefAP to calculate these concentrations using the DOS effective masses of the electrons and holes (Equations 3.34 and 3.35) is used. The values reported by Green [111] are used for the effective masses of electrons and holes. Green tabulated values between 50 K and 500 K, at 50 K intervals; DefAP uses an interpolation function to estimate values at temperatures falling in the intervals. A charge correction is calculated and applied to the formation energy of each charged defect, using Equation 3.39 and a static dielectric constant of 11.9 [112]. The task `energy` instructs DefAP to calculate the formation energy of each defect at the VBM, and when coupled with the task `form_plots`, DefAP produces figures illustrating the defect's formation energy dependence on Fermi level across the length of the band gap, if a charged system is studied. Figure 3.5 demonstrates the output of this task for the intrinsic defects studied in Si, with a separate plot for interstitials and vacancies (please note that the charge labels have been manually added). Figure 3.5 shows only the charge state with the lowest formation energy for each defect, which is an optional user choice. It is seen that positively charged $\mathrm{Si_{i,T}}$ interstitials have the lowest formation energy below the midpoint of the band gap, whereas neutral and negatively charged $\mathrm{Si_{i,110}}$ interstitials are favoured above the midpoint, towards the conduction band. Negatively charged $V_{\mathrm{Si,B}}$ vacancies are found to have lowest formation energy across the majority of the band gap. All defects have relatively high formation energies, explaining the low concentrations of intrinsic defects seen in Si. The values and trends seen in Figure 3.5 are in close agreement with the DFT study of Centoni *et al.* [113] where the interstitial and vacancy with the lowest formation energy varied between the VBM and CBM in the order $\mathrm{Si_{i,T}^{2+}} \rightarrow \mathrm{Si_{i,110}^{\times}} \rightarrow \mathrm{Si_{i,110}^{1-}}$ and $V_{\mathrm{Si,L}}^{1+} \rightarrow V_{\mathrm{Si,L}}^{\times} \rightarrow V_{\mathrm{Si,L}}^{1-} \rightarrow V_{\mathrm{Si,B}}^{2-}$, respectively.

Figure 3.6 displays the output of the task `brouwer`: a plot of the defect concentrations as a function of a chosen variable, in this case, temperature. Intrinsic silicon is predicted to have a very low concentrations of defects. The carrier concentra-

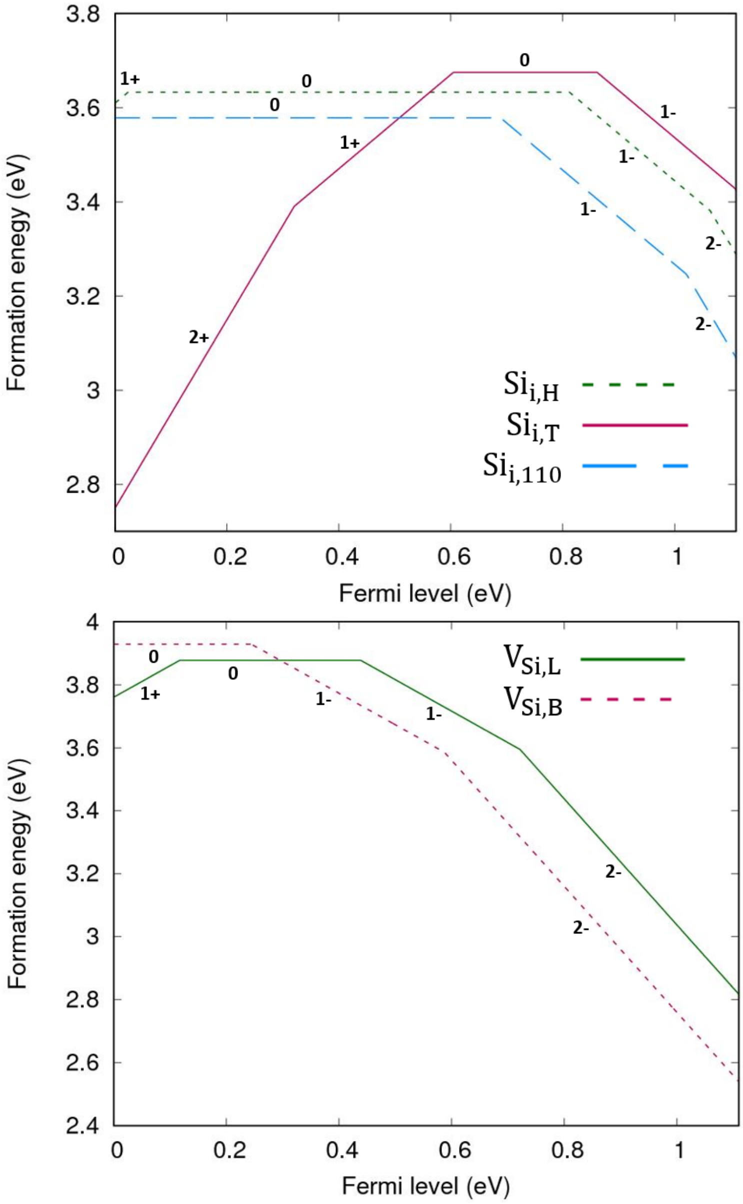

Figure 3.5: Defect formation energies for intrinsic interstitials (top) and vacancies (bottom) in Si as a function of Fermi energy. Only the charge state with the lowest formation energy for a given Fermi level is shown for each defect, represented with numeric label.

tions are equal, but none of the intrinsic defects are found to exist at a concentration above 10^{-12} cm^{-3} in the temperature range studied. Si is doped with impurity atoms to alter its properties; for example incorporation of phosphorus creates n-type Si. One Si atom is replaced with a P atom to create a Si substitutional, $\mathrm{P}^{\mathrm{j}}_{\mathrm{Si,L}}$, with integer j values between ± 3 considered. This substitutional was found to be the favoured accommodation site of P in Si, compared to the three interstitial sites discussed earlier. DefAP then uses the methodology described in Section 3.2.5 to investigate the impact of a fixed concentration of 1×10^{15} cm^{-3} (equivalent to a concentration of approximately 2×10^{-8} P atoms per Si). Figure 3.6 shows that DefAP correctly predicts that P behaves as an n-type dopant, raising the Fermi level in Si, and consequently increasing the concentration of electrons. The dominant P defect charge states are predicted to be $\mathrm{P}^{\times}_{\mathrm{Si,L}}$ and $\mathrm{P}^{1+}_{\mathrm{Si,L}}$ with the former making up the bulk of P in Si at low temperatures. The impact of adding P on the Fermi level is shown on the plot in Figure 3.7. This plot, illustrating the predicted Fermi level as a function of the environmental variable selected (temperature in this case) is automatically produced by DefAP when using the task `brouwer`. Two of these plots are superimposed in Figure 3.7 to allow comparison.

3.3.2 Yttrium barium copper oxide

The critical temperature of the high temperature superconductor $YBa_2Cu_3O_7$ has been shown to be dependent upon the value of x in $YBa_2Cu_3O_{7-x}$, motivating the study of point defects in the material. Vacancies, interstitials, and antisite defects are studied, taking into account the different, unique defect sites in $YBa_2Cu_3O_7$ that are possible due to its orthorhombically shaped unit cell. Clustered oxygen vacancies are also considered: pairs of oxygen vacancies in the Cu-O chain, denoted V_{O2}, were calculated. The DFT treatment of this complex crystallography is discussed in previous work [114]. $YBa_2Cu_3O_7$ falls into the category of a non-binary volatile compound; to calculate the chemical potentials of Y, Ba, Cu, and O,

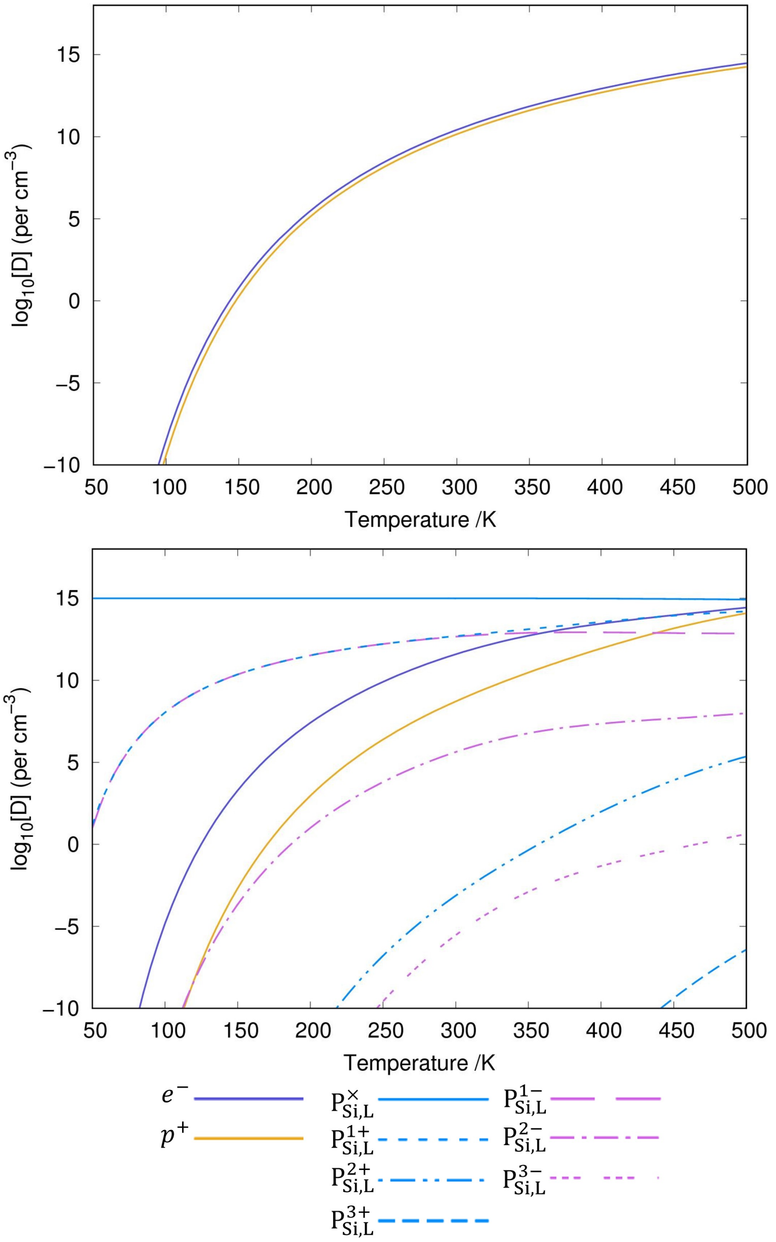

Figure 3.6: The defect concentrations in Si as a function of temperature with a P concentration of (top) 0.0 and (bottom) 1×10^{15} cm^{-3} (equivalent to a concentration of approximately 2×10^{-8} P atoms per Si). The carrier concentrations are equal in the top figure, the concentration of electrons were artificially shifted in order for both lines to be visible.

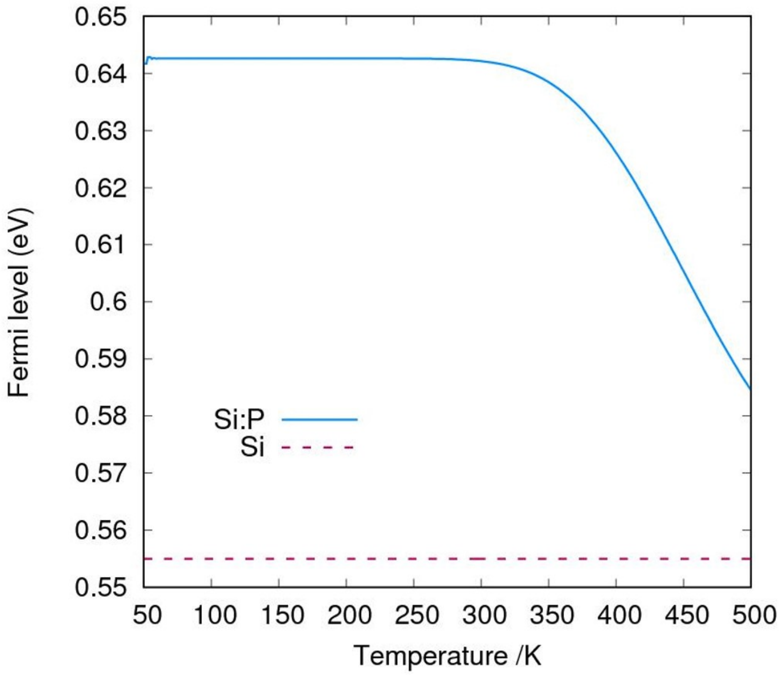

Figure 3.7: The predicted Fermi level as a function of temperature in intrinsic and P-doped Si, with a P concentration of 1×10^{15} cm^{-3} (equivalent to a concentration of approximately 2×10^{-8} P atoms per Si).

DefAP uses the method outlined in Section 3.2.1 (Equations 3.18-3.26), using the real heat capacities of O_2 to determine the oxygen chemical potential temperature dependence. This method requires that three binary oxides are defined (one for each metal species in the host) that $YBa_2Cu_3O_7$ could theoretically be constructed from. The following oxides are selected:

$$3\mathrm{Cu_2O_{(s)}} + 4\mathrm{BaO_{(s)}} + \mathrm{Y_2O_{3(s)}} + 2\mathrm{O_{2(g)}} \rightarrow \mathrm{YBa_2Cu_3O_{7(s)}} \tag{3.45}$$

Running the task `stability` evaluates the thermodynamic stability of an unlimited number of possible competing phases, requiring only the DFT energy of each compound to be defined. Checking the ten compounds in Table 3.1 reveals that at 700 K, an oxygen partial pressure of 10^{-4} atm, and Cu_2O-poor conditions, it is predicted that the compounds Y_2BaO_4 and $Ba_2(CuO_2)_3$ are thermodynamically stable with respect to $YBa_2Cu_3O_7$: i.e. it would be thermodynamically favorable

Table 3.1: The stability of selected competing phases in the $YBa_2Cu_3O_7$ system calculated at 700 K, an oxygen partial pressure of 10^{-4} atm, and Cu_2O-poor conditions. $\Delta\mu$ denotes the difference between the summed chemical potentials calculated by DefAP and the DFT energy of each compound. A positive $\Delta\mu$ indicates thermodynamic stability w.r.t. $YBa_2Cu_3O_7$.

Compound	$\Delta\mu$
Y_2BaO_4	0.0950
$Y_4Ba_3O_9$	-0.0798
$YCuO_2$	-0.826
YCu_2O_4	-0.425
BaCu	-6.05
$BaCu_3O_4$	-0.742
$Ba_2(CuO_2)_3$	0.734
CuY	-9.69
Cu_2BaO_2	-1.16
Cu_5Y	-14.5

for these two phases to form as secondary phases within $YBa_2Cu_3O_7$.

At this point, it is useful to further explain the method used in DefAP to define regions of stability within a material, using $YBa_2Cu_3O_7$ as an example. As discussed, the first step is always to assume that the material can be fabricated from a series of binary volatile compounds (i.e, Equation 3.45 for $YBa_2Cu_3O_7$). This then defines a region of chemical space where the material is stable with respect to the compounds selected to construct the material. This region is depicted for $YBa_2Cu_3O_7$ as a function of μ_{Cu} and μ_{Y} at an oxygen partial pressure of 10^{-4} atm and a temperature of 700 K in Figure 3.8. The user can then navigate this region of chemical space by varying the fraction, f^j, assigned to each compound, j. The second step — which is optional — is to investigate whether, at the position in chemical space requested via the assignment of f^j, the material is stable with respect to any number of secondary phases. Figure 3.9 illustrates how this would look like for the example system, $YBa_2Cu_3O_7$: at these conditions, five of the phases in Table 3.1 are stable in, at least, a portion of the defined chemical space.

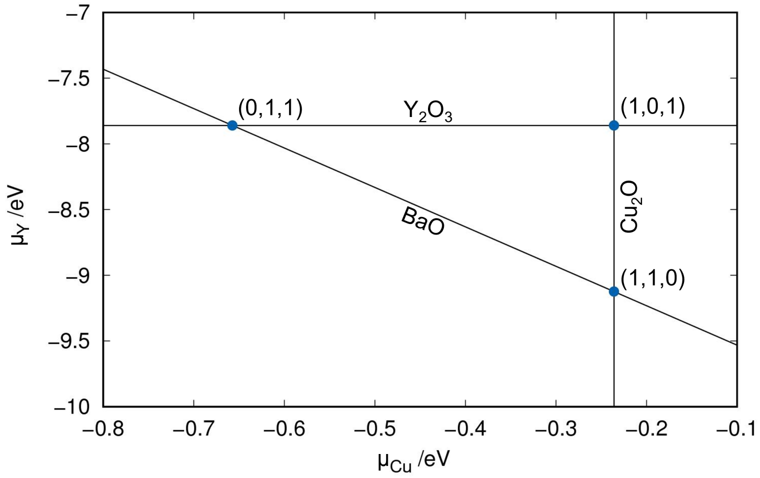

Figure 3.8: Chemical potential diagram showing μ_{Cu} and μ_{Y} at a temperature of 700 K and an oxygen partial pressure of 10^{-4} atm. The points indicated on the diagram correspond to different regimes — these are based on the fractions assigned to the three binary oxides that were defined to construct $\mathrm{YBa_2Cu_3O_7}$, i.e. ($f^{\mathrm{Cu_2O}}$, f^{BaO}, $f^{\mathrm{Y_2O_3}}$).

The compound $\mathrm{Ba_2(CuO_2)_3}$ is shown to be stable throughout the whole space; at $\mathrm{Cu_2O}$-poor conditions, two phases are stable, highlighting the data produced in Table 3.1.

When DefAP predicts that the material is unstable, it displays a clear warning, and prints to the output file a recording of the tested phases with the relevant calculations. This methodology is chosen — as opposed to the user defining a stable region of stable chemical space that considers all possible phases — to facilitate the key principle of DefAP: the evaluation of a material's defect chemistry over a range of conditions. The stable region of chemical space changes very significantly as a function of environmental conditions. This is shown using Figure 3.8 which plots the stability region of $\mathrm{YBa_2Cu_3O_7}$ as a function of μ_{Cu}, μ_{Y} and temperature at an oxygen partial pressure of 10^{-4} atm. Temperature can be seen to impact heavily both the size and positioning of the stable region of chemical space. The second part of the figure depicts the huge reduction in the size of the space when a portion of the phases in Table 3.1 are also considered.

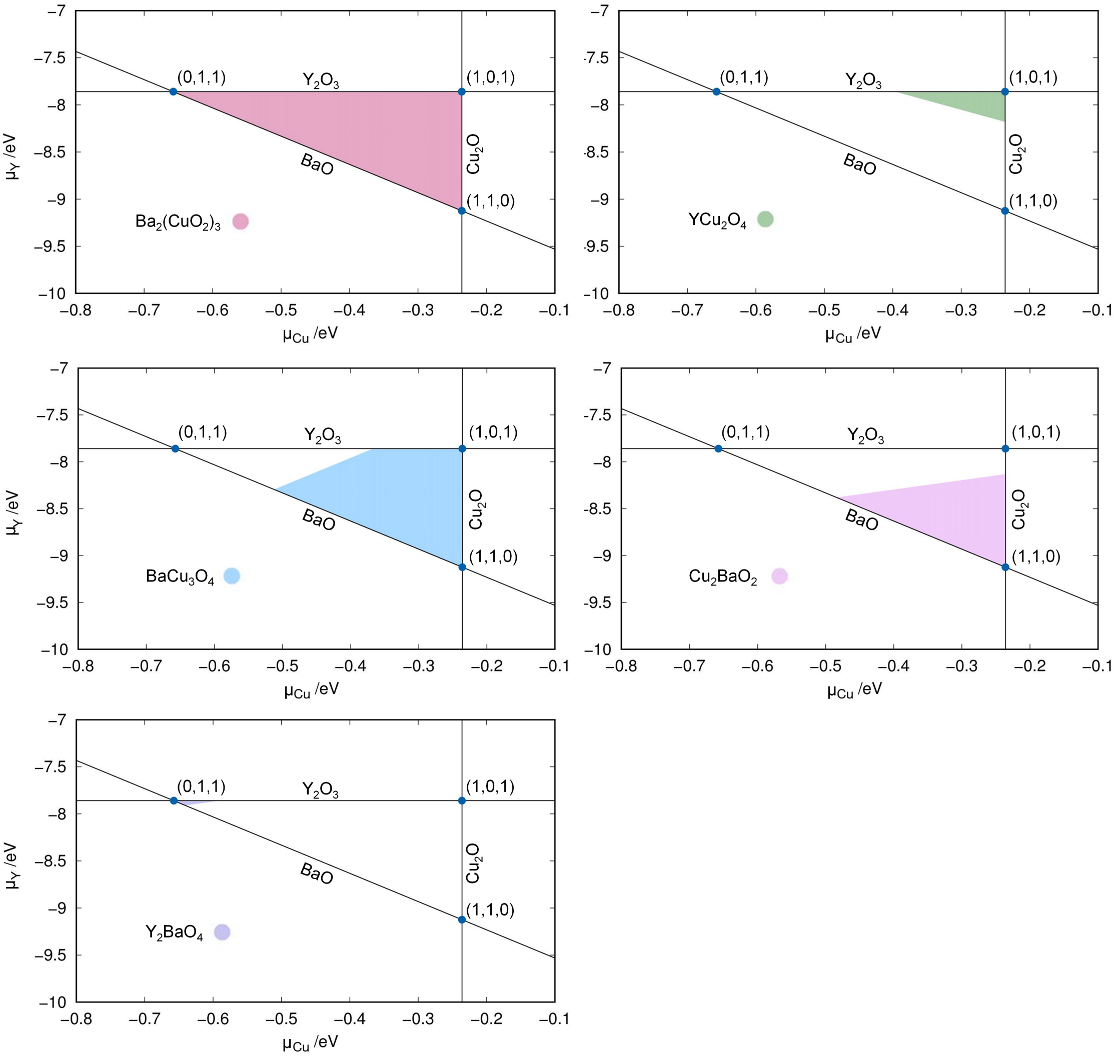

Figure 3.9: Chemical potential diagram showing μ_{Cu} and μ_{Y} at a temperature of 700 K and an oxygen partial pressure of 10^{-4} atm. A coloured region indicates conditions where the labelled secondary phase is predicted to be stable with respect to $\mathrm{YBa_2Cu_3O_7}$. The points indicated on the diagram correspond to different regimes — these are based on the fractions assigned to the three binary oxides that were defined to construct $\mathrm{YBa_2Cu_3O_7}$, i.e. $(f^{\mathrm{Cu_2O}}, f^{\mathrm{BaO}}, f^{\mathrm{Y_2O_3}})$.

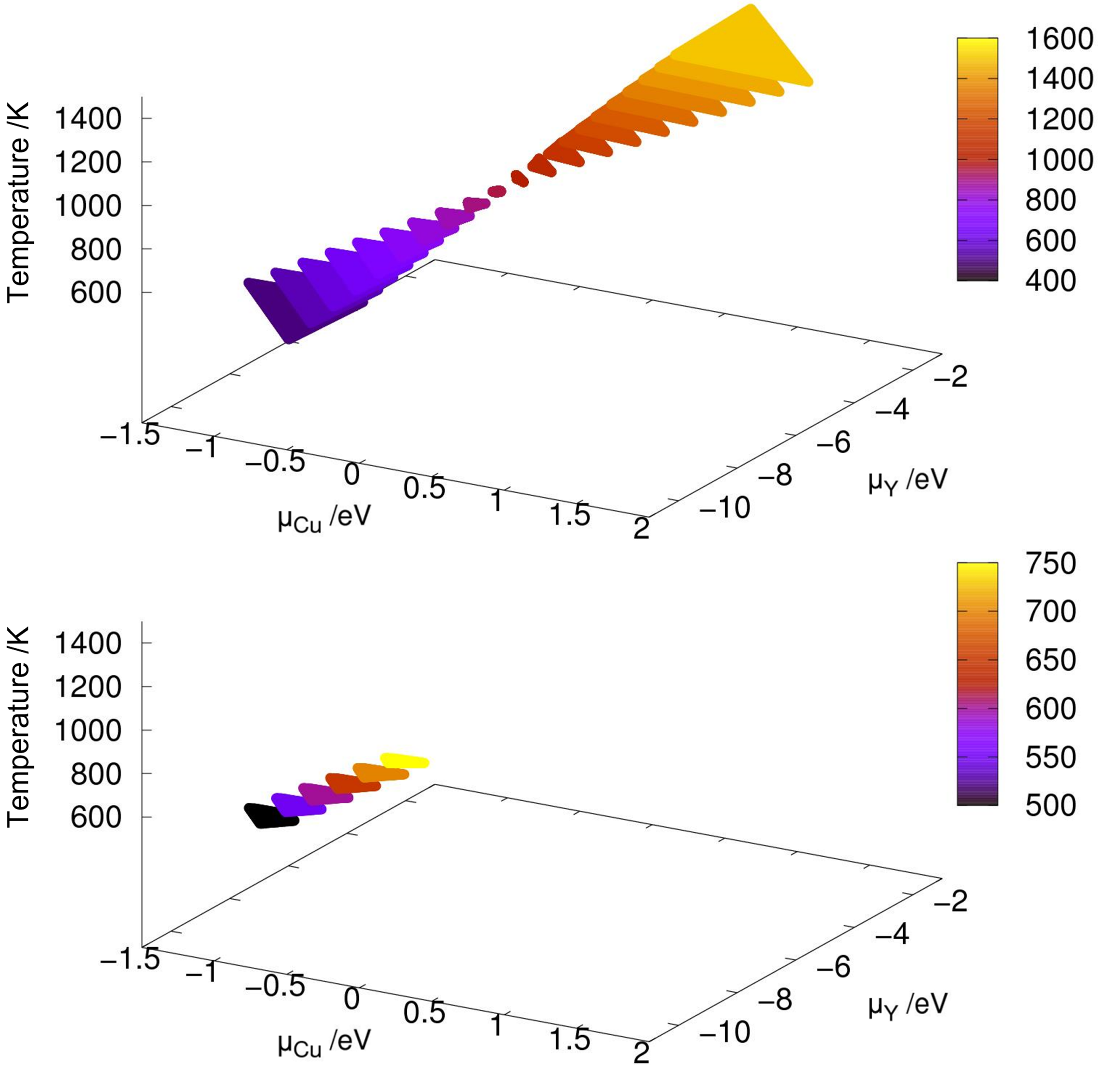

Figure 3.10: Illustration of the stability region of $YBa_2Cu_3O_7$ as a function of μ_{Cu}, μ_{Y} and temperature at an oxygen partial pressure of 10^{-4} atm. The top plot indicates the stability region constructed from Equation 3.45. The bottom plot indicates the stability region when the secondary phases listed in Table 3.1* are also considered. $*$With the exception of $Ba_2(CuO_2)_3$: this phase is predicted to be stable at all conditions plotted, it is omitted to illustrate the concept of a shrinking stability region.

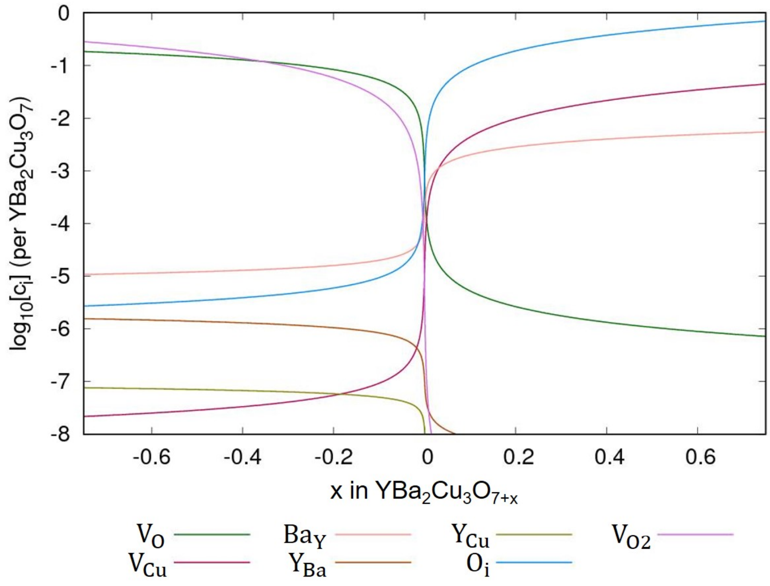

Figure 3.11: The concentration of defects in in $YBa_2Cu_3O_{7+x}$ as a function of x at 700 K under Cu_2O-poor conditions.

Returning to the defect chemistry of $YBa_2Cu_3O_7$, Figure 3.11 presents the output of the task `brouwer` for the system at 700 K, under Cu_2O-poor conditions (BaO- and Y_2O_3-rich conditions). The option in DefAP to plot the defect concentrations as a function of x in $YBa_2Cu_3O_{7+x}$ is used and for clarity, sum and plot together all defects of the same type by using the task `group` meaning that for example $c_{V_{Cu}} = c_{V_{Cu1}} + c_{V_{Cu2}}$. Figure 3.11 enables easy interpretation of the defects that are predicted to cause oxygen deficiency in $YBa_2Cu_3O_{7-x}$: It is the oxygen vacancy defects that are responsible for the deficiency, with the clustered vacancies increasingly significant with increasing x.

3.3.3 Lithium metatitanate

Li_2TiO_3, is a leading candidate tritium breeding material for use in a future fusion reactor. The material generates tritium by transmutation of the Li induced by the neutron produced in the fusion reaction: ${}^{6}_{3}Li + {}^{1}_{0}n \rightarrow {}^{4}_{2}He + {}^{3}_{1}T$. With use of the SLSQP algorithm implemented in DefAP, the accommodation method of defined quantities of both He and T is studied concurrently, as well as their impact on the intrinsic defect chemistry of Li_2TiO_3. To attain the chemical potentials of the host elements, Li, Ti and O, DefAP repeats the method described for $YBa_2Cu_3O_7$ (also a non-binary compound) using the following oxides to thermodynamically construct Li_2TiO_3:

$$\mathrm{Li_2O_{(s)}} + \mathrm{TiO_{2(s)}} \rightarrow \mathrm{Li_2TiO_{3(s)}} \tag{3.46}$$

Continuing from previous work [115, 116], each conceivable intrinsic defect at every unique site in the Li_2TiO_3 unit cell and at all accessible charge states is investigated. Li and O substitutions, as well as interstitial sites, are considered here as the possible T and He incorporation sites. To calculate the concentration of electrons and holes, Boltzmann statistics are selected (Equations 3.30 & 3.31). Li_2TiO_3 is an example of a non-cubic system that exhibits anisotropic dielectric properties, necessitating careful consideration of the charge correction assigned to the charged defects studied. The task `madelung` is used to calculate v_M^{scr} for Li_2TiO_3, using Equation 3.40 and the dielectric tensor predicted by Murphy and Hine [104], thereby accounting for the anisotropic nature of Li_2TiO_3:

$$\bar{\epsilon} = \begin{bmatrix} 36.1 & 0 & -5.0 \\ 0 & 37.8 & 0 \\ -5.0 & 0 & 17.8 \end{bmatrix} \tag{3.47}$$

DefAP automatically uses the v_M^{scr} calculated to apply a charge correction (Equation 3.39) when computing the formation energies of the charged defects in subsequent tasks. The result of the task `brouwer`, with the task `group` used to sum defects of the same type that vary only in position in the cell, is shown in Figure 3.12. The plots shows the concentration of defects in Li_2TiO_3 at 1000 K under either Li_2O- or TiO_2-rich conditions. Figures 3.12a & b show that when both T and He concentrations are fixed at 0.01 atoms per Li_2TiO_3 functional unit, T is incorporated as either $\mathrm{T_O^{1+}}$ or $\mathrm{T_i^{1+}}$ defects in Li_2O-rich conditions, and $\mathrm{T_{Li}^{\times}}$ defects in TiO_2-rich conditions. Meanwhile, He is incorporated as either He_{O}^{2+} or $He_{i}^{\times}$ defects in Li_2O-rich conditions, and He_{Li}^{1-} defects in TiO_2-rich conditions. So far, this result is indicative that the presence of T or He in Li_2TiO_3 does not affect the method of incorporation of the other impurity; the methods of incorporation are not predicted to be altered compared to when T and He have been studied individually [115, 116]. This can be further explored by using the option in DefAP to study defect concentrations as a function of a chosen dopant element concentration. In Figures 3.12c & d, the defect concentrations in Li_2TiO_3 are plotted as a function of T concentration, with He concentration fixed at 0.01 atoms per Li_2TiO_3 functional unit. It can now be seen that, in Li_2O-rich conditions, the quantity of T present does impact the mode of He accommodation. At low T concentrations, He is accommodated as both $He_{i}^{\times}$ and He_{O}^{2+} defects. However, increasing the total concentration of T present results in only the $He_{i}^{\times}$ being favorable. This is due to the T being accommodated as the positively charged T_{i}^{1+} defect, therefore, as this increases to ensure charge neutrality the concentration of He_{O}^{2+} must decrease. In contrast, the equivalent result at TiO_2-rich conditions finds that the concentration of T has no bearing on the mode of He incorporation, due to the dominant $T_{Li}^{\times}$ defect being charge neutral. The intrinsic defect chemistry of Li_2TiO_3 is also predicted to alter in response to increasing He concentrations: charge compensation for the T_{i}^{1+} defect is provided by increasing the concentration of the Li_{Ti}^{3-} defect.

3.4 Summary

This chapter has introduced DefAP, a Python code designed to analyse a material's defect chemistry by processing the results of DFT calculations according to the instructions of the user, generating an output of plots designed with gnuplot. This chapter has used example systems to demonstrate the flexibility and capabilities of the code. The formation energies of charged intrinsic defects in Si as a function of Fermi level were predicted, whilst the equilibrium concentration of defects, and

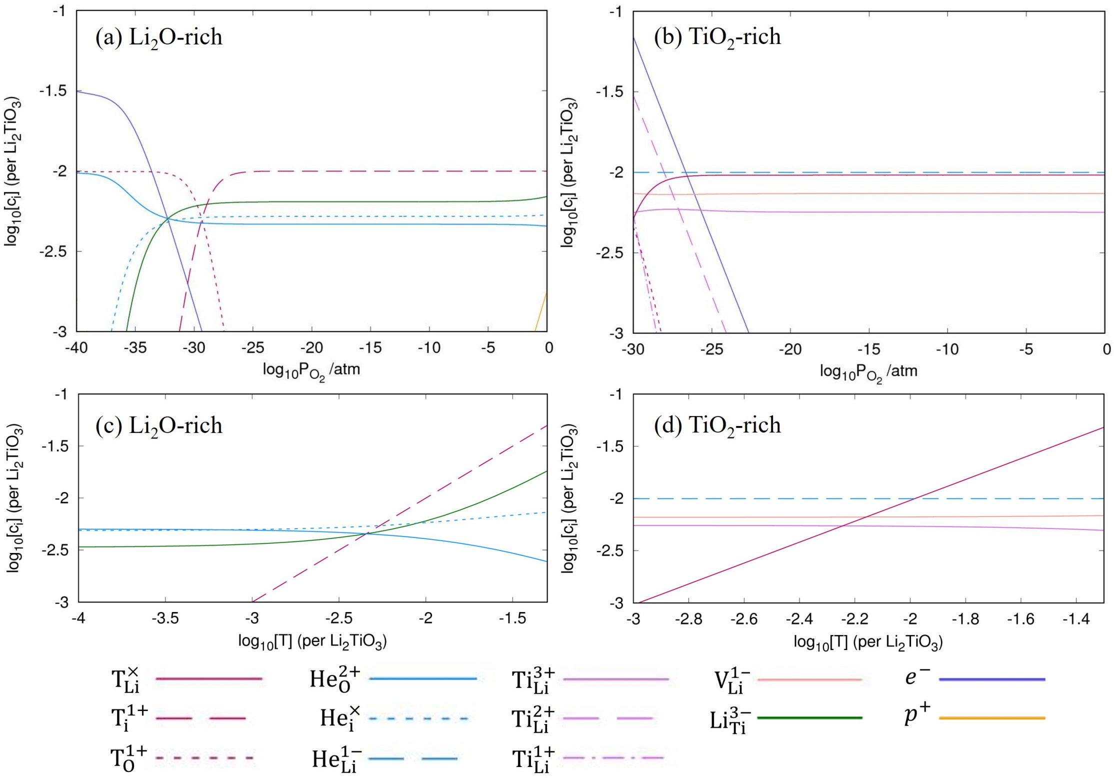

Figure 3.12: The concentration of defects in Li_2TiO_3 at 1000 K under Li_2O and TiO_2-rich conditions. In (a) and (b) concentrations are plotted as a function of oxygen partial pressure with the total concentration of T and He fixed at 0.01 atoms per Li_2TiO_3 functional unit. In (c) and (d) concentrations are plotted as a function of the total concentration of T, with the total concentration of He fixed at 0.01 atoms per Li_2TiO_3 functional unit and an oxygen partial pressure of 10^{-20} atm.

carriers where applicable, were studied in Si , $YBa_2Cu_3O_7$, and Li_2TiO_3. A suitable point charge correction can be calculated on request in the event charged defects are studied, that is applicable to both isotropic and anisotropic systems. DefAP has an extensive set of options for studying dopants; here, the dopant P in Si, and the breeder products T and He in Li_2TiO_3 were studied. DefAP will now be used to aid the investigation of the defect chemistry of PuO_2 in the chapters that follow. The package is available on GitHub at https://github.com/DefAP/defap.

Chapter 4

Intrinsic defect chemistry of $PuO_{2\pm x}$

This work is published in:

W.D. Neilson, J.T. Pegg, H. Steele, and S.T. Murphy, "The defect chemistry of non-stoichiometric $PuO_{2\pm x}$", *Physical Chemistry Chemical Physics*, vol. 23, pp. 4544-4554, 2021. [117]

The article is part of the themed collection: 2021 PCCP HOT Articles.

4.1 Introduction

The formation of intrinsic point defects are a cause and mechanism of deviation in perfect stoichiometry of a material. The defect chemistry of a material can describe the defects responsible for the deviation, as well as the conditions these defects will form. In this chapter, the intrinsic point defect processes of $PuO_{2\pm x}$ are studied to further understanding of the material's evolution across a range of experimentally relevant conditions. In particular, attention is paid to the PuO_{2+x} phase: the defect chemistry should inform whether an intrinsic defect mechanism (i.e. formation of O interstitials or Pu vacancies) is thermodynamically favourable.

Section 2.2 briefly reviewed the history of this search, as well as the pertinence to PuO_2 storage safety.

Multiple studies have investigated the formation energies of intrinsic and extrinsic defects in PuO_2 [79, 80, 118, 119, 120, 121, 122]. Thermochemical models have been produced that study the defect chemistry of $PuO_{2\text{-}x}$, over a large stoichiometry range [123, 124], whilst using DFT + U and a point defect model, Lu *et al.* [79] determined the stability of charged defects within $PuO_{2\pm x}$. A consensus has been reached that O-type defects dominate the defect chemistry, owing to a stable Pu sub-lattice. Lu *et al.* [79] report that the V_{O}^{2+} defect is responsible for hypo-stoichiometry, whilst the O_{i}^{2-} defect is the source of hyper-stoichiometry; the study also suggested that under reasonable conditions, O_{i}^{2-} defects are able to exist at relatively high concentrations; i.e. PuO_{2+x} is attainable.

An updated methodology will be used in this chapter to re-analyse the material's defect chemistry. DFT simulations of point defects in PuO_2 will take full account of non-collinear magnetism to attain defect energies that will be incorporated, alongside an empirically calculated vibrational entropy contribution, into the updated point defect model within DefAP.

4.2 Methodology

The concentration of point defects are calculated using Boltzmann statistics (Equation 3.1) which is a function of the formation energy of each defect, calculated with Equation 3.2. This methodology section details how the parameters that feed Equation 3.2 are calculated.

4.2.1 Computational methodology

DFT simulations were performed using VASP employing the projector augmented wave (PAW) [125, 126] method implemented with the frozen-core approximation. The plutonium 6*s*, 6*p*, 5*f*, 6*d* and 7*s* and oxygen 1*s*, 2*s* and 2*p* electrons are treated as valence. Following convergence testing, the cut-off energy for the planewave basis set was selected to be 500 eV and a 4 × 4 × 4 Monkhorst-Pack k-point mesh [63] was used for the 12-atom PuO_2 unit cell. For 2 × 2 × 2 supercells used in defect simulations, the k-point mesh is adjusted to 2 × 2 × 2. The non-collinear relativistic computational study of the PuO_2 magnetic structure by Pegg *et al.* [48] finds a longitudinal 3k AFM magnetic ground state for PuO_2, which was adopted in this study. This magnetic configuration is described in Figure 2.8. SOI [127] is considered as not including it resulted in a different magnetic ground state being obtained [48].

To study the properties of the bulk PuO_2, the study of Pegg *et al.* [48] is replicated which used the hybrid Heyd-Scuseria-Ernzerhof (HSE06) functional [128, 129, 130, 131]:

$$E_{\mathrm{XC}}^{\mathrm{HSE}} = \frac{1}{4}E_{\mathrm{X}}^{\mathrm{HF,SR}}(\mu) + \frac{3}{4}E_{\mathrm{X}}^{\mathrm{PBE,SR}}(\mu) + E_{X}^{\mathrm{PBE,LR}}(\mu) + E_{\mathrm{C}}^{\mathrm{PBE}} \tag{4.1}$$

where $E_{\mathrm{XC}}^{\mathrm{HSE}}$ is the exchange-correlation HSE06 energy, $E_{\mathrm{X}}^{\mathrm{HF,SR}}$ is the short-range HF exchange, $E_{\mathrm{X}}^{\mathrm{PBE,SR}}$ and $E_{\mathrm{X}}^{\mathrm{PBE,LR}}$ are the short-range and long-range components of the PBE exchange functional respectively and $E_{\mathrm{C}}^{\mathrm{PBE}}$ is the PBE correlation energy. A quarter of the short-range HF exchange is used in this functional and the screening parameter (μ) is 0.207 Å^{-1}. The iteration threshold for electronic and ionic convergence when using this functional is 1×10^{-6} eV and 1×10^{-2} eV Å^{-1}, respectively.

For calculation of defect energies in PuO_2 supercells hybrid functionals are computationally too expensive; DFT calculations are therefore performed with the GGA using the PBE functional revised for solids (PBEsol) [65, 66]. The PBEsol functional was shown by Pegg *et al.* [48] to best reproduce experimental properties, where available, in actinide dioxides when using the DFT + U formulism. The strong correlations due to *f*-electrons in Pu were accounted for by applying the DFT + U method using the Liechtenstein formulism [50]. When using PBEsol + U, the iteration threshold for electronic convergence is 1×10^{-6} eV and for ionic convergence is 1×10^{-2} eV Å^{-1} and 2×10^{-2} eV Å^{-1} when simulating PuO_2 unit cells and defect containing PuO_2 supercells, respectively. In this study, the U parameter within PBEsol + U was selected such that it reproduced the band gap obtained from the HSE06 functional (3.04 eV). It was chosen to reproduce the HSE06 band gap as the experimental data shows a large variation (see Section 2.3.1) and this functional has been proven to replicate experimental band gaps well [47]. This resulted in a U parameter of 7.0 eV being used for this study (see Figure 4.1). The use of a high U parameter is not without precedence, with several previous studies adopting U values exceeding 6.0 eV when studying actinide dioxides, including PuO_2 [49, 132]. The J parameter was fixed at a value of 0.0 eV throughout this study, as any introduction of J was shown by Pegg *et al.* [49] to detrimentally affect the reproduction of the band gap for PuO_2. The resulting equilibrium properties found for longitudinal 3k AFM PuO_2 simulated using either the HSE06 functional or PBEsol + U ($U = 7.0$ eV) are presented in Table 4.1. The discrepancy between the theoretical and experimental description of the magnetic properties of PuO_2 was discussed in the Section 2.4.2.

In summary, it was chosen to reproduce the HSE06 bandgap to set U as the experimental data shows a large variation and this functional has been proven to replicate experimental band gaps [47]. Figure 4.2 presents comparison of the projected DOS obtained using the PBEsol + U and HSE06 functionals. Increasing U is seen to increase the band gap, but decrease the hybridisation of the O (p) and Pu(f) bands at the VBM. The band gaps predicted for U values of 1 eV, 4 eV, and 7

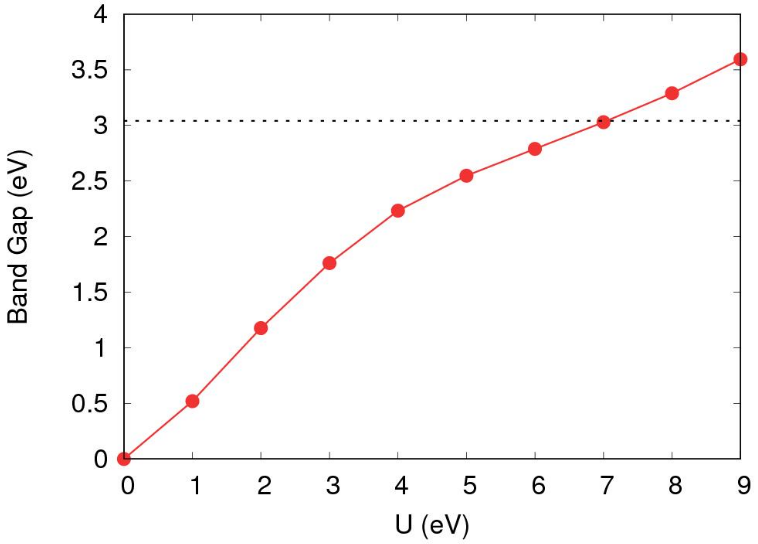

Figure 4.1: Variation of band gap as a function of the Coulomb modifier (U). Band gap value calculated using the HSE06 functional shown with horizontal dotted line.

Table 4.1: The lattice constant (Å), magnetic moment (μ_B/Pu ion), band gap energy (eV) and crystal symmetry for longitudinal 3k AFM PuO_2 calculated using either the HSE06 functional or PBEsol + U (U = 7.0 eV). In addition, the reported experimental values are shown.

		Lattice constant (Å)	Magnetic moment (μ_B/Pu ion)	Band gap (eV)	Magnetic configuration	Space group
This work	HSE06	5.379	3.65	3.04	Longitudinal 3k AFM	$Fm\bar{3}m$
	PBEsol+U	5.415	3.82	3.03	Longitudinal 3k AFM	$Fm\bar{3}m$
Exp.		5.399 [133]	0.00 [76]	1.80 [56] 2.80 [57] 3.92 [58] 4.1 [59]	DM [76]	$Fm\bar{3}m$ [81]

eV are 0.52 eV, 2.23 eV, and 3.03 eV, respectively. The HSE06 functional predicts a band gap of 3.04 eV. PBEsol + U is unable to achieve a band gap exceeding 2.5 eV, as predicted by experiment [57, 59, 58] and hybrid DFT, whilst maintaining the hybridisation of the O (p) and Pu(f) bands at the VBM. Whilst the choice of *U* impacts the DOS, the impact to the DFT formation energy of a defect is found to be minimal. Table 4.2 demonstrates this, reporting the dependence on the DFT formation energy of the 2+ oxygen vacancy on the choice of *U* in the PBEsol + U functional.

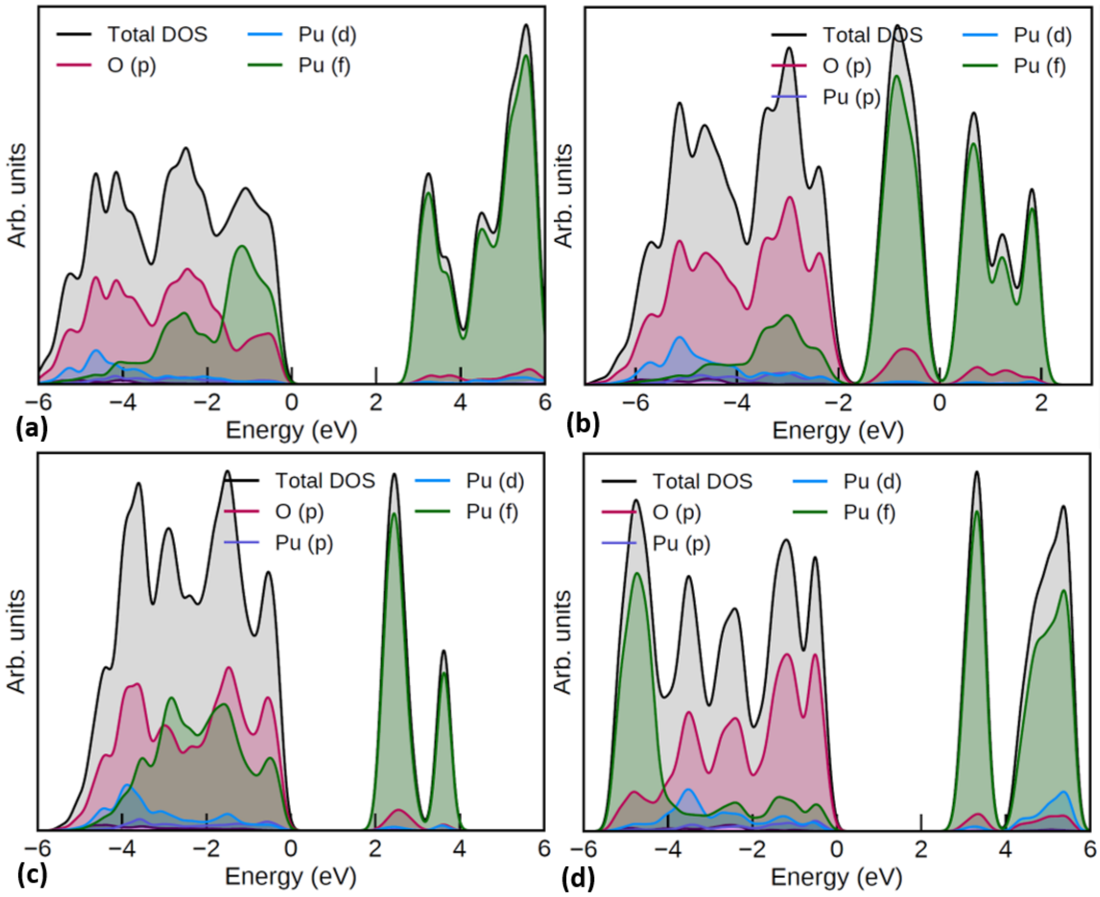

Figure 4.2: The density of states of PuO_2 calculated by (a) the HSE06 hybrid functional and the PBEsol + U functional where (b) $U = 1$ eV, (c) $U = 4$ eV, and (d) $U = 7$ eV.

Table 4.2: The impact of the choice of U in the PBEsol + U functional on the difference in energy between a defect-free PuO_2 supercell and a PuO_2 supercell containing a 2+ oxygen vacancy.

U (eV)	DFT formation energy of V_O^{2+} defect (eV)	Difference in energy, compared to $U = 7$ eV (eV)	Percentage difference, compared to $U = 7$ eV
3	-9.68	0.15	1.54
4	-9.69	0.15	1.51
5	-9.71	0.12	1.27
6	-9.76	0.076	0.78
7	-9.84	0	0

Defects were inserted into 2 × 2 × 2 expansions of the 12-atom PuO_2 unit cell. Only one unique site exists for the vacancies and interstitials of plutonium and oxygen considered, due to the symmetry of the PuO_2 lattice. Different charge states were considered for each defect, modelled by adding or removing electrons from the supercell. Defect-containing supercells were relaxed under constant volume, using the lattice constants obtained from defect-free simulations. The defects considered in this study are denoted below:

Oxygen interstitials: $O_i^{\times}$, O_i^{1-} and O_i^{2-}

Oxygen vacancies: $V_O^{\times}$, V_O^{1+} and V_O^{2+}

Plutonium interstitials: $Pu_i^{\times}$, Pu_i^{1+}, Pu_i^{2+}, Pu_i^{3+} and Pu_i^{4+}

Plutonium vacancies: $V_{Pu}^{\times}$, V_{Pu}^{1-}, V_{Pu}^{2-}, V_{Pu}^{3-} and V_{Pu}^{4-}

4.2.2 Vibrational entropies

Vibrational entropies are obtained using empirical potentials, with the General Utility Lattice Program (GULP) [134] together with the Cooper, Rushton and Grimes (CRG) potential [135, 136]. This is a many-body potential model used to describe actinide oxide systems which achieves good reproduction of thermodynamic and mechanical properties. The phonon DOS for PuO_2, calculated with the CRG potential and compared to the experimental data of Manley *et al.* [137] is shown in Figure 4.3. The calculated phonon DOS compares reasonably well to the experimental data. Many of the characteristic peaks and troughs are replicated, although at high frequency the magnitude of these features is smaller for the calculated data. This is a result of adopting a large *k*-point mesh that smooths the phonon DOS, and at high frequencies the experimental data has wide error bars [137]. The calculation of vibrational entropies, S_{vib}, follows the method described in Section 2.5.3. In this study, the system to calculate vibrational entropies is a 4 × 4 × 4 expansion of the PuO_2 unit cell. Defective supercells are created by adding or removing atoms and are relaxed under constant volume in the same way as the DFT simulations. Defect vibrational entropies are found by calculating the difference in vibrational entropies between the defective and perfect supercell (ΔS_{vib}) and presented in Table 4.3 alongside the vibrational entropy of PuO_2 per formula unit. The same value of ΔS_{vib} is given to all charge states of a given defect.

4.2.3 Finite size correction

To calculate the finite size correction, E_{corr}, for the charged defects studied, a number of available methods are surveyed. The simplest correction that can be calculated is the point charge (PC) correction. For a cubic system, such as PuO_2, the PC correction energy can be written Equation 4.2 — the cubic form of Equation

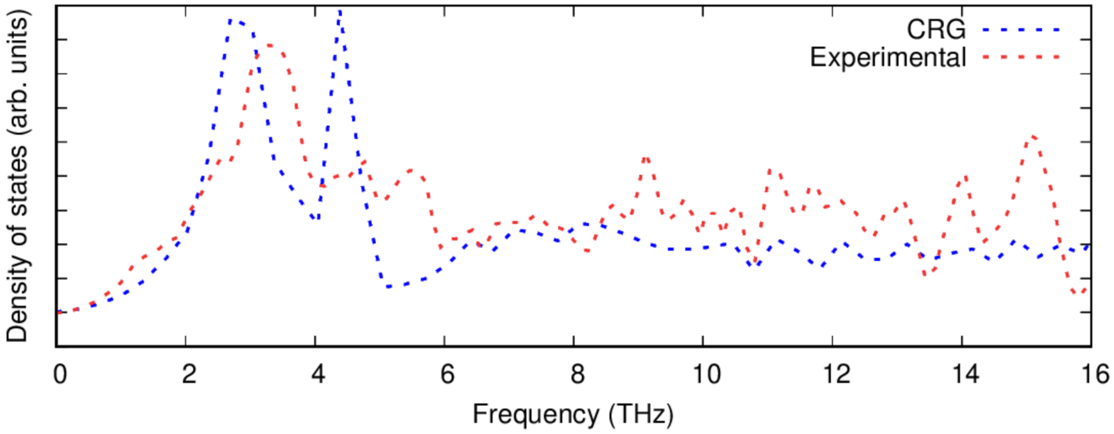

Figure 4.3: The phonon density of states of PuO_2 calculated with the CRG empirical potential (blue), compared to experimental data [137] (red).

Table 4.3: The difference in vibrational entropy of PuO_2 due to the addition of a defect, calculated using the CRG potential.

T (K)	Defect entropy ($\Delta S_{\mathrm{vib}}/k_{\mathrm{B}}$)			
	V_O	O_i	V_{Pu}	Pu_i
400	0.545	4.572	-3.783	2.518
600	-0.453	5.373	-5.245	3.110
800	-1.230	6.058	-6.208	3.725
1000	-1.868	6.638	-6.940	4.270
1200	-2.391	7.137	-7.508	4.746
1400	-2.843	7.578	-7.996	5.164
1600	-3.238	7.961	-8.402	5.547
1800	-3.574	8.309	-8.761	5.883
2000	-3.899	8.599	-9.086	6.174

3.39:

$$E_{\mathrm{PC}}^{\mathrm{iso}} = \frac{q^2\alpha}{2\epsilon L} \tag{4.2}$$

where α = 2.837 is the lattice-type dependent Madelung constant, L is the super cell lattice constant and ϵ is the static dielectric constant. The static dielectric constant of PuO_2 was calculated using density functional perturbation theory (DFPT) as implemented in VASP. The previously described longitudinal 3k AFM PuO_2 unit cell with PBEsol + U (U = 7.0 eV) is used. The static dielectric tensor of PuO_2, ε_{ij} is calculated by summing its electronic and ionic components. The average of the static dielectric tensor, $\frac{1}{3}\mathrm{Tr}(\varepsilon_{ij})$ is calculated and used as the static dielectric constant of PuO_2. A static dielectric constant of 19.66 is obtained; this compares favourably to the experimental value (18.9 [138]) and falls between the experimental value for UO_2 (23.8 [139]) and the DFT-obtained value for AmO_2 (17.40 [140]), thus fits within the emerging trend.

Makov and Payne (MP) extended the PC correction to include a term with L^{-3} order [100]. More recently Freysoldt, Neugebauer and Van de Walle (FNV) developed a correction that compares the planar-averaged electrostatic potentials of supercells with and without defects ($V_{\mathrm{defect,q}}$ & V_{bulk} respectively) [102]. The FNV scheme correction energy is summarised following Ref. [105] as:

$$E_{\mathrm{corr}} = E_{\mathrm{PC}}^{\mathrm{iso}} - q\Delta V_{\mathrm{PC,q/b|far}} \tag{4.3}$$

$$V_{\mathrm{q/b}} = V_{\mathrm{defect,q}} - V_{\mathrm{bulk}} \tag{4.4}$$

$$\Delta V_{\mathrm{PC,q/b}} = V_{\mathrm{q/b}} - V_{\mathrm{PC,q}} \tag{4.5}$$

$\Delta V_{\mathrm{PC,q/b}}$ is the potential difference between the defect induced potential ($V_{\mathrm{q/b}}$) and the PC potential, $V_{\mathrm{PC,q}}$. $\Delta V_{\mathrm{PC,q/b|far}}$ is $\Delta V_{\mathrm{PC,q/b}}$ at a position far from the defect site but still within the supercell. The FNV scheme has been demonstrated to be an effective correction in many systems [141], however the use of planar-averaged electrostatic potentials can provide unreliable corrections when the atomic positions of the defective supercell are allowed to relax. This was observed in the system investigated in this study: with the example of a $\mathrm{V}_{\mathrm{Pu}}^{4-}$ supercell, $\Delta V_{\mathrm{PC,q/b|far}}$ could not be determined accurately as $V_{\mathrm{q/b}}$ was seen to strongly fluctuate whilst $V_{\mathrm{PC,q}}$ remains parabolic (illustration in Figure 4.4). Consequently, this study employs the correction of Kumagai and Oba which uses atomic site electronic potentials as opposed to planar averaged electrostatic potentials [105]. Using the same example of a $\mathrm{V}_{\mathrm{Pu}}^{4-}$ supercell, Figure 4.5 shows that this scheme is able to produce $\Delta V_{\mathrm{PC,q/b|far}}$ that is close to constant across the sampling region. Kumagai and Oba also demonstrate that a potential alignment correction, sometimes adopted to shift the valance band maximum of a charged defect to that of a pristine host, is not required [105].

The best measure of the effectiveness of a correction scheme is its ability to allow, when implemented, the use of relatively small simulation cells to study point defects. When used, the dependence of a defect's energy on the cell size should be reduced to the best possible extent. The strong performance of the Kumagai and Oba scheme is illustrated in Figure 4.6. The difference in the value of $E_{\mathrm{defect}}^{\mathrm{DFT}} - E_{\mathrm{perfect}}^{\mathrm{DFT}}$ calculated for a $\mathrm{V}_{\mathrm{Pu}}^{4-}$ $3 \times 3 \times 3$ supercell and a $\mathrm{V}_{\mathrm{Pu}}^{4-}$ $2 \times 2 \times 2$ decreases from 1.29 eV when no correction is applied to 0.06 eV following correction. This gives confidence that the correction works well for the system studied here.

4.2.4 Chemical potentials

To determine the chemical potentials of the two constituent elements, Pu and O, the method in DefAP that is designed for binary compounds containing an element that is in the gas phase in its standard state is used. This method was described generally in Section 3.2.1; in this section the specific method as appropriate for the $\mathrm{PuO_2}$ system will be provided.

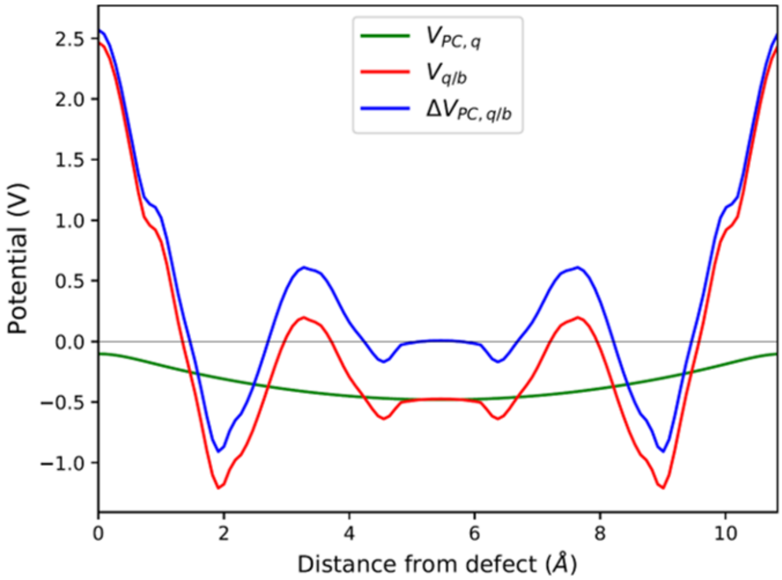

Figure 4.4: Planar averaged $V_{\mathrm{q/b}}$, $V_{\mathrm{PC,q}}$ and $\Delta V_{\mathrm{PC,q/b}}$ calculated at the atomic positions of a PuO_2 supercell with a V_{Pu}^{4-} defect.

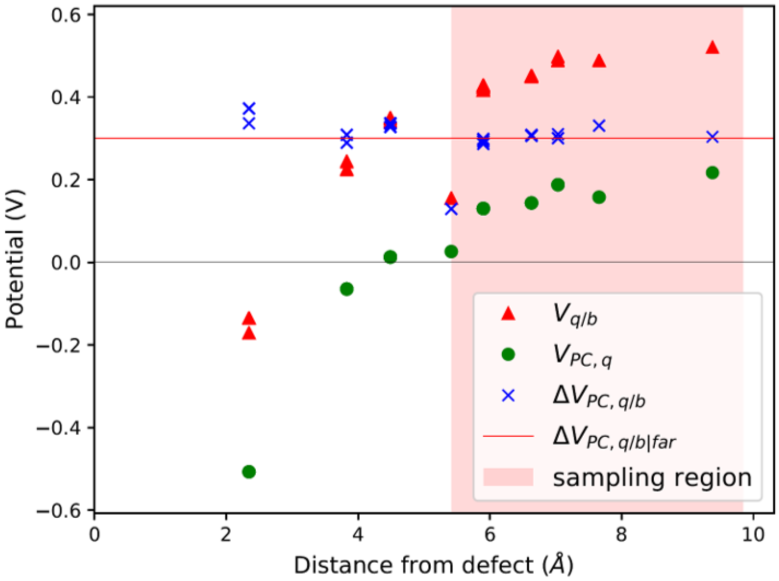

Figure 4.5: $V_{\mathrm{q/b}}$, $V_{\mathrm{PC,q}}$ and $\Delta V_{\mathrm{PC,q/b}}$ calculated at the atomic positions of a PuO_2 supercell with a V_{Pu}^{4-} defect. $\Delta V_{\mathrm{PC,q/b|far}}$ calculated by averaging $\Delta V_{\mathrm{PC,q/b}}$ across sampling region.

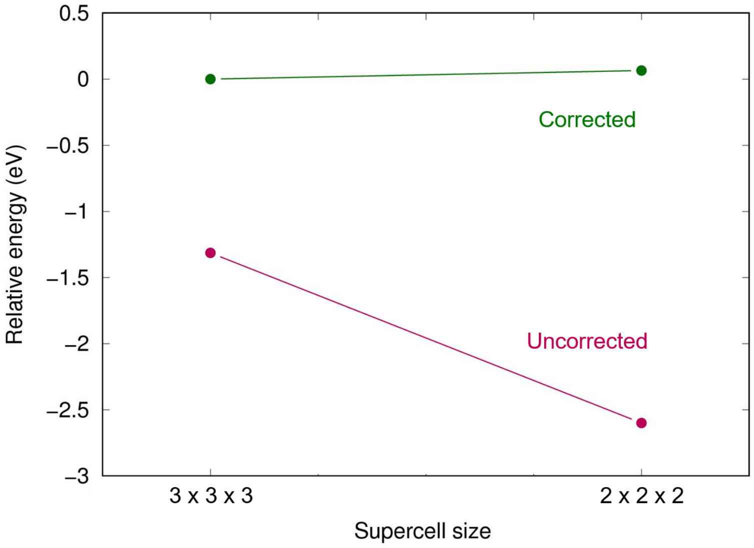

Figure 4.6: The effectiveness of the finite-size correction of Kumagai and Oba [105] illustrated using the example of the V_{Pu}^{4-} defect. Plotted is the relative difference in $E_{\text{defect}}^{\text{DFT}}$ and $E_{\text{perfect}}^{\text{DFT}}$ (the DFT total energies of the PuO_2 supercell with and without the defect, respectively) compared for two supercell sizes.

The starting point is to define the chemical potential of solid PuO_2 ($\mu_{\text{PuO}_{2(\text{s})}}$) in terms of the chemical potential per formula unit of the constituent species, namely plutonium, $\mu_{\text{Pu}}(P_{\text{O}_2}, T)$, and oxygen, $\mu_{\text{O}_2}(P_{\text{O}_2}, T)$:

$$\mu_{\text{Pu}}(P_{\text{O}_2}, T) + \mu_{\text{O}_2}(P_{\text{O}_2}, T) = \mu_{\text{PuO}_{2(\text{s})}} \tag{4.6}$$

For a solid $\mu(P^{\circ}_{\text{O}_2}, T^{\circ}) \approx \mu(0, 0)$, therefore the temperature and pressure dependencies have been dropped. In equilibrium conditions, the chemical potential of Pu cannot exceed that of solid Pu, otherwise a Pu precipitate would form. This upper bound is the Gibbs free energy of Pu in its natural state. It can therefore be said that in Pu-rich conditions:

$$\mu_{\text{Pu}}(P_{\text{O}_2}, T) = \mu_{\text{Pu}_{(\text{s})}} \tag{4.7}$$

To find $\mu_{\text{Pu}_{(\text{s})}}$ the α phase of Pu is simulated with DFT using PBEsol + U. Using the recommendation of the review by Söderlind *et al.* [142] to use small *U* and *J* values, the *U* and *J* parameters are set at 2.2 eV and 0.58 eV respectively. The atomic volume obtained with these values (18.27 Å^3) matched closely the atomic volume obtained by Söderlind *et al.* [142] when using PBE + U. To determine the chemical potential of oxygen the approach of Finnis *et al.* [107] is adopted. This method uses the known experimental formation energy of the oxide ($\Delta H_{\mathrm{f}}^{\mathrm{PuO_2}}(P^{\circ}_{\mathrm{O_2}}, T^{\circ})$ = -10.94 eV [143]) to obtain the chemical potential of oxygen at standard temperature and pressure, i.e.:

$$\Delta H_{\mathrm{f}}^{\mathrm{PuO_2}}(P^{\circ}_{\mathrm{O_2}}, T^{\circ}) = \mu_{\mathrm{PuO_{2(s)}}} - \mu_{\mathrm{Pu_{(s)}}} - \mu_{\mathrm{O_2}}(P^{\circ}_{\mathrm{O_2}}, T^{\circ}) \tag{4.8}$$

Unlike the solid species in Equation 4.8, the temperature and pressure dependence of the oxygen chemical potential cannot be neglected and is extrapolated from $\mu_{\mathrm{O_2}}(P^{\circ}_{\mathrm{O_2}}, T^{\circ})$ according the Equation 4.9:

$$\mu_{\mathrm{O_2}}(P_{\mathrm{O_2}}, T) = \mu_{\mathrm{O_2}}(P^{\circ}_{\mathrm{O_2}}, T^{\circ}) + \Delta\mu(T) + k_{\mathrm{B}}T\log\frac{P_{\mathrm{O_2}}}{P^{\circ}_{\mathrm{O_2}}} \tag{4.9}$$

Where $\Delta\mu(T)$, the temperature contribution to the chemical potential is determined from the real heat capacities of the O$_2$ molecule:

$$\Delta\mu(T) = \frac{1}{2}(G(P^{\circ}, T) - G(P^{\circ}, T^{\circ})) \tag{4.10}$$

where,

$$G(P^{\circ}, T) = A(T - T\ln(T)) - \frac{1}{2}BT^2 - \frac{1}{6}CT^3 - \frac{1}{12}DT^4 - \frac{E}{2T} + F - GT \tag{4.11}$$

Equation 4.11 and parameters $A - G$ are taken from Johnston *et al.* [109].

The electron chemical potential is a function of the Fermi level: $\mu_{\mathrm{e}} = E_{VBM} + \varepsilon_{\mathrm{F}}$. The Fermi level is computed such that charge neutrality, Equation 3.29, is achieved. This requires the charge contribution from electrons and holes in the system to be known; Fermi-Dirac statistics are applied to the electronic DOS to obtain the concentrations of electrons (e^{-}) in the conduction band and concentration of holes (p^{+}) in the valence band (Equations 3.32 & 3.33).

4.2.5 Stoichiometry

Finally, the deviation from stoichiometry, x in PuO$_{2\pm\mathrm{x}}$ can be calculated from the predicted defect concentrations summed over all charge states:

$$x = \frac{2 + [\mathrm{O_i}] - [\mathrm{V_O}]}{1 + [\mathrm{Pu_i}] - [\mathrm{V_{Pu}}]} - 2 \tag{4.12}$$

4.3 Results & discussions

The formation energy of all defects considered are plotted as a function of the Fermi level in Figure 4.7. Figure 4.7 shows the formation energies at 1000 K and O-rich (10^{-2} atm)/O-poor (10^{-30} atm) conditions, displaying only the charge state of each defect that corresponds to the lowest formation energy at a given position in the bandgap. For each defect it can be seen that, to varying degrees, the charge state with the lowest energy varies across the bandgap. $\mathrm{V_{Pu}}$ defects have the least variation, its full ionic charge state ($\mathrm{V_{Pu}^{4-}}$) has the lowest energy across the majority of the bandgap. Conversely, under halfway across the bandgap, the neutral $\mathrm{V_O^{\times}}$ defect is seen to overtake the fully charged $\mathrm{V_O^{2+}}$ defect as the oxygen vacancy with the lowest formation energy. Prodan *et al.* [31] report that $\mathrm{O_i^{1-}}$ is the most energetically favourable charge state for the oxygen interstitial. Here it is found that although the $\mathrm{O_i^{2-}}$ defect has the lowest energy for much of the bandgap, $\mathrm{O_i^{1-}}$ becomes favourable at low Fermi level values, with $\mathrm{O_i^{\times}}$ most favourable at the lowest Fermi levels close to the valence band. Therefore, under certain conditions this study also finds $\mathrm{O_i^{1-}}$ to be the preferred interstitial. Across the band gap the favourable charge state of $\mathrm{Pu_i}$ defects are seen to vary, with each charge state except $\mathrm{Pu_i^{2+}}$ possessing the lowest formation energy over fairly large ranges in Fermi level.

Table 4.4 displays the calculated reaction energy of unbound oxygen and pluto-

Table 4.4: Reaction energies (in eV) for the intrinsic processes in PuO_2 with comparison to experimental and previous theoretical studies. Theoretical studies are separated further, based on if results are obtained using DFT or empirically.

Method	Study	O Frenkel pair $V_O^{2+} + O_i^{2-}$	Pu Frenkel pair $V_{Pu}^{4-} + Pu_i^{4+}$	Schottky defect $V_{Pu}^{4-} + 2V_O^{2+}$
DFT + U	This work	4.89	13.86	7.65
	LSDA + *U* [79]	3.48	15.19	7.51
	LDA + *U* [120]	4.58	10.02	6.09
	GGA + *U* [122]	3.9	11.90	
Empirical	Ref. [118]	5.52	13.58	10.40
	Ref. [119]	2.66	10.03	3.54
	Ref. [122]	4.90	24.00	
Experiment	Ref. [144]	2.72-2.92		

nium Frenkel pairs (FP) and the unbound Schottky tri-vacancy (STV), with defects formally charged. Each reaction energy is found to be within the range of previous theoretical calculations, which are provided for comparison in Table 4.4. The ranges are seen to be of the order of several eV; in the DFT + U studies, the different exchange-correlation functionals employed may explain the differences. The review of Murch *et al.* [144] provides the only experimental comparison available, indicating that the oxygen Frenkel pair has a much lower formation energy than calculated here. Caution is however attached to the oxygen Frenkel pair experimental result, which is described by Murch *et al.* [144] as “on the low side”. The results match the established pattern in all techniques, where O-FP $<$ STV $<$ Pu-FP, showing that oxygen-type defects are significantly more favourable than plutonium-type defects.

The resulting point defect concentrations, calculated as a function of temperature at a fixed oxygen partial pressure of 10^{-5} atm, are presented in Figure 4.8. Concentrations of oxygen defects are observed to be multiple orders of magnitude greater than cation defect concentrations across all temperatures. This agrees with

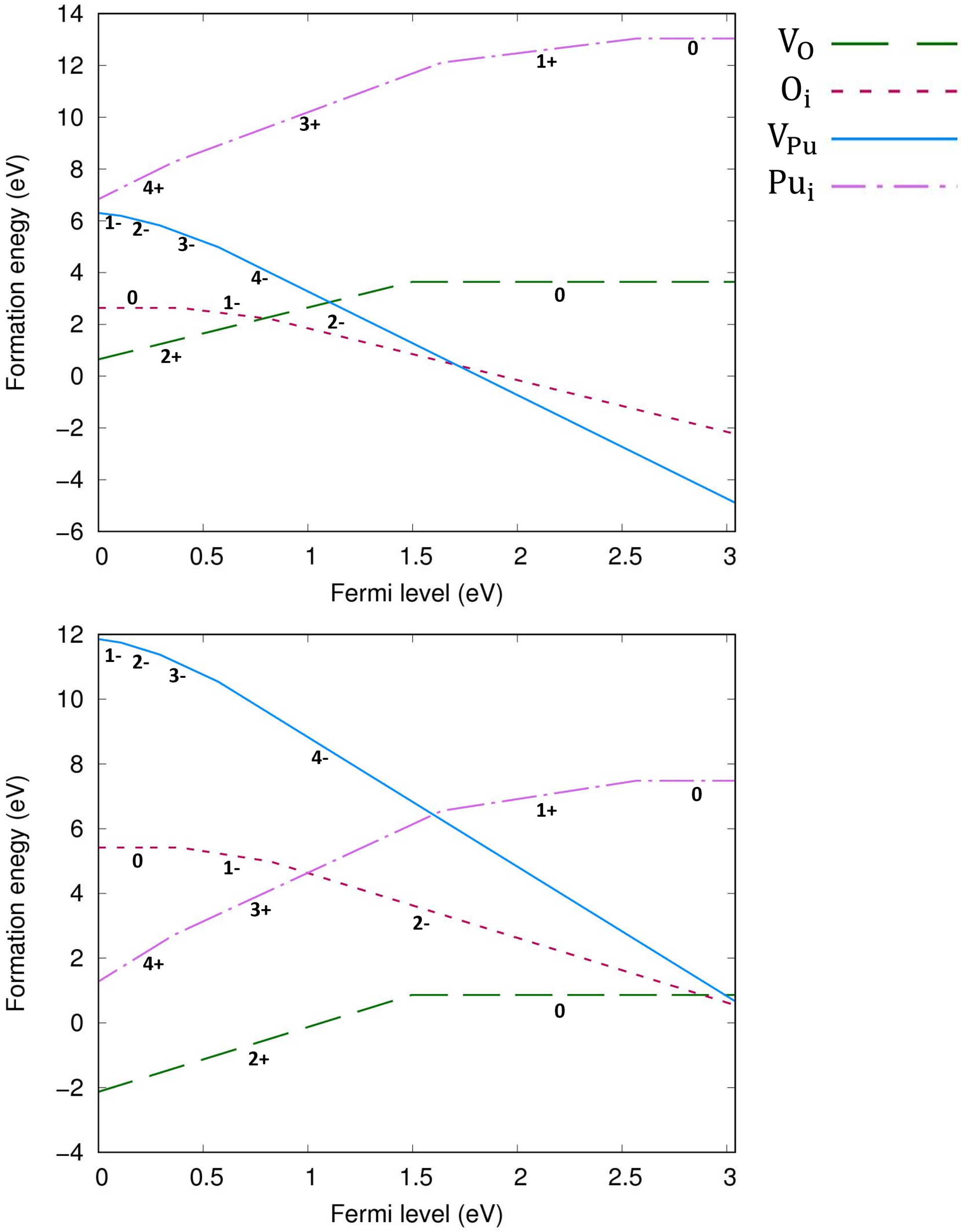

Figure 4.7: Defect formation energies for O vacancies & interstitials as well as Pu vacancies & interstitials as a function of Fermi energy. Calculated at 1000 K and oxygen partial pressure of 10^{-2} atm (top) and 10^{-30} atm (bottom). Only the charge state with the lowest formation energy for a given Fermi level is shown for each defect, represented with numeric label.

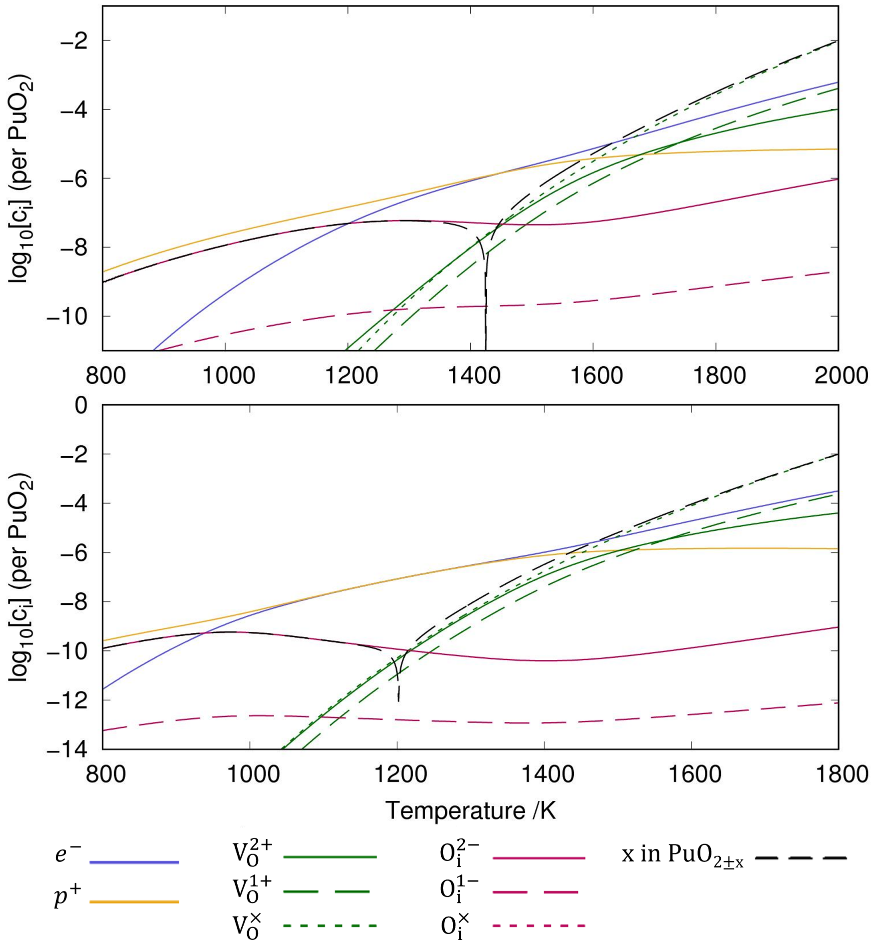

Figure 4.8: The defect chemistry of $PuO_{2\pm x}$ as a function of temperature at an oxygen partial pressure of 10^{-5} atm. The diagrams include (top) and exclude (bottom) vibrational entropy contributions when calculating defect concentrations. To the left and right of the minima of the black line, the diagram records the calculated value of $\log_{10}[x]$ in $PuO_{2\text{-}x}$ and PuO_{2+x}, respectively.

previous experimental work that metal defects are minority defects in PuO_2 [144]. All plutonium vacancy and interstitial defects are predicted to have such low concentrations that do not appear in Figure 4.8. Figure 4.8 also displays the impact of including vibrational entropy contributions. Inclusion of vibrational entropy is seen to increase the temperature at which perfect stoichiometry occurs: ≈ 1200 K when vibrational entropy is omitted versus ≈ 1425 K when included. Perfect stoichiometry occurs when $[O_i] = [V_O]$, meaning that vibrational entropy inclusion further promotes O_i defects. From the point of perfect stoichiometry, increasing or decreasing temperature results in hypo-stoichiometric or hyper-stoichiometric $PuO_{2\pm x}$ respectively. The diagrams display the reluctance for PuO_2 to be hyper-stoichiometric in oxygen, with x in PuO_{2+x} peaking at approx. 10^{-7} at 1210 K (when vibrational entropy included), representing negligible hyper-stoichiometry. As temperature decreases from this peak, the concentration of defects and the value of x in PuO_{2+x} falls. The concentration of defects becomes increasingly negligible; this continues beyond the range of Figure 4.8, at lower temperatures. It can be seen hypo-stoichiometry is much more favourable, which correlates with the wide hypo-stoichiometric region evident in the phase diagram of PuO_2 [145].

From this point onwards, all plots discussed include vibrational entropy. Broadly speaking, the diagram in Figure 4.8 can be broken down into three regions based upon electron and hole concentrations: these are a hole-dominant region, a region of equal concentration and an electron dominant region. At low temperatures the O_i defects dominate and are charge compensated by holes. The $[O_i]$:$[p^+]$ ratio is approximately 1:2, due to the dominance of the O_i^{2-} defect. Increasing the temperature past the point of peak-hyper-stoichiometry, which coincides with peak $[O_i]$, the hole concentration is no longer set such that it provides charge compensation to O_i defects. Instead, the concentration of holes matches the concentration of electrons and the Fermi level remains fixed at the midpoint of the bandgap. $[V_O]$ increases with temperature, resulting in increasing hypo-stoichiometry. At high temperatures, $[V_O]$ reaches levels close to the concentration of holes and electrons. To accommodate any further increases in $[V_O]$, the concentration of electrons increases to maintain charge neutrality. The concentration of holes then decreases as the temperature increases resulting in the Fermi level increasing. In this region, the $[V_O]$:$[e^-]$ ratio varies in order to provide charge compensation to both V_O^{2+} and V_O^{1+} defects.

The defect chemistry of PuO_2 as a function of oxygen partial pressure is presented in the Brouwer diagrams of Figure 4.9, at temperatures 1000 K and 2000 K. At

1000 K, in the region close to perfect stoichiometry, where x in PuO$_{2\pm x}$ is at its smallest, $\mathrm{O_i^{2-}}$ is the dominant oxygen interstitial. The dominant oxygen vacancies are found to be $\mathrm{V_O^{2+}}$ and $\mathrm{V_O^{\times}}$, which have concentrations of similar magnitude, with $\mathrm{V_O^{\times}}$ at narrowly higher concentrations. In this region of near-stoichiometry, the defect chemistry and dependence on oxygen partial pressure can be attributed to the following defect reactions occurring:

$$\frac{1}{2}\mathrm{O_2} + e^- \rightleftharpoons \mathrm{O_i^{2-}} + p^+ \tag{4.13}$$

$$\mathrm{O_O^{\times}} + p^+ \rightleftharpoons \mathrm{V_O^{2+}} + e^- + \frac{1}{2}\mathrm{O_2} \tag{4.14}$$

$$\mathrm{O_O^{\times}} \rightleftharpoons \mathrm{V_O^{\times}} + \frac{1}{2}\mathrm{O_2} \tag{4.15}$$

Application of the law of mass action to Equations 4.13, 4.14 and 4.15 finds equilibrium constants of k_1, k_2 and k_3, respectfully:

$$k_1 = [\mathrm{O_i^{2-}}][p^+][e^-]^{-1}\mathrm{P}_{\mathrm{O_2}}^{-\frac{1}{2}} \tag{4.16}$$

$$k_2 = [\mathrm{V_O^{2+}}][e^-][p^+]^{-1}\mathrm{P}_{\mathrm{O_2}}^{\frac{1}{2}} \tag{4.17}$$

$$k_3 = [\mathrm{V_O^{\times}}]\mathrm{P}_{\mathrm{O_2}}^{\frac{1}{2}} \tag{4.18}$$

Given that $[e^-] = [p^+]$, it can be seen that $[\mathrm{O_i^{2-}}]$ is proportional to $\mathrm{P}_{\mathrm{O_2}}^{\frac{1}{2}}$, whilst $[\mathrm{V_O^{2+}}]$ and $[\mathrm{V_O^{\times}}]$ are proportional to $\mathrm{P}_{\mathrm{O_2}}^{-\frac{1}{2}}$ in this region. Increasing the oxygen partial pressure beyond the region of near-stoichiometry sees the concentration of holes, $\mathrm{O_i^{2-}}$ defects and x in PuO$_{2+x}$ transition to an oxygen partial pressure dependence of $\mathrm{P}_{\mathrm{O_2}}^{\frac{1}{6}}$. With too few electrons available, two holes are created for charge compensation of the $\mathrm{O_i^{2-}}$ defect. Equations 4.19 and 4.20 show the defect reaction responsible and the corresponding equilibrium constant, respectively. Given that $[\mathrm{O_i^{2-}}] = 2[p^+]$, it can be shown using Equation 4.20 that $[\mathrm{O_i^{2-}}]$ is proportional to

$P_{O_2}^{\frac{1}{6}}$ in the hyper-stoichiometric region.

$$\frac{1}{2}O_2 \rightleftharpoons O_i^{2-} + 2p^+ \tag{4.19}$$

$$k_4 = [O_i^{2-}][p^+]^2 P_{O_2}^{-\frac{1}{2}} \tag{4.20}$$

Reducing the oxygen partial pressure below the region of near-stoichiometry sees the concentration of V_O^{2+} defects transition to a dependence on the oxygen partial pressure of $P_{O_2}^{-\frac{1}{6}}$, whilst concentration of $V_O^{\times}$ defects maintain a dependence on the oxygen partial pressure of $P_{O_2}^{-\frac{1}{2}}$. Consequently, it is Equation 4.15 that is the dominant defect reaction in the hypo-stoichiometric region, causing $V_O^{\times}$ defects to become the dominant defect and the source of hypo-stochiometric $PuO_{2\text{-x}}$. The dependence of x in $PuO_{2\text{-x}}$ has been shown experimentally to have a dependence on the oxygen partial pressure of $P_{O_2}^{-\frac{1}{4}}$ [124], indicative of the V_O^{1+} vacancy being dominant. This result reflects experimental data at large non-stoichiometry, where the point defect model breaks down due to the occurrence of complex processes involving defect clusters. The result of this work, that reflects very small non-stoichiometry, can therefore not be directly compared.

Comparing the two Brouwer diagrams in Figure 4.9, increasing temperature creates a more reducing environment, increasing oxygen vacancy concentrations. Perfect stoichiometry therefore occurs at higher oxygen partial pressures. Aside from this, in the 1000 K temperature range investigated here, temperature is found not to alter the defect chemistry of PuO_2 significantly.

The finding that the defect chemistry of PuO_2 is dominated by oxygen interstitials and vacancies agrees with the predictions in the PuO_2 point defect study of Lu *et al.* [79]. However, the present study has found a significant increase in the concentrations of non-formally charged defects relative to their formally charged counterparts. Whereas Lu *et al.* [79] found $[O_i^{2-}]$ and $[V_O^{2+}]$ defects to be multiple orders of magnitude greater than any non-formally charged defect, here $V_O^{\times}$ is the

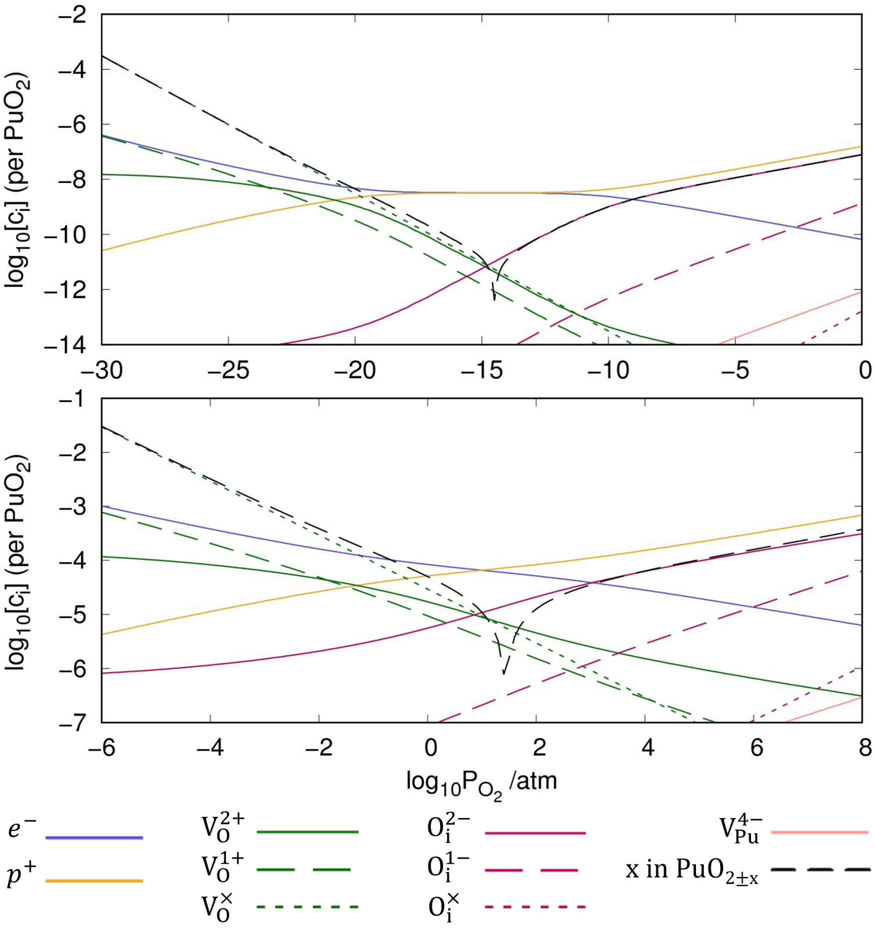

Figure 4.9: Calculated Brouwer diagram showing the defect chemistry of $PuO_{2\pm x}$ as a function of the oxygen partial pressure at 1000 K (top) and 2000 K (bottom). Both diagrams include vibrational entropy contributions when calculating defect concentrations. To the left and right of the minima of the black line, the diagram records the calculated value of $\log_{10}$[x] in PuO_{2-x} and PuO_{2+x}, respectively.

dominant oxygen vacancy and concentration of O_i^{1-} is predicted to be much closer to that of O_i^{2-}. This can be partially attributed to the larger bandgap used in this work (3.04 eV vs 1.70 eV). Electrons and holes, which are required to provide charge compensation to charged defects, have an increased formation energy with increased band gap. Therefore, increasing the bandgap increases the favourability of defects with a smaller charge magnitude. Additionally, here a much lower degree of hyper-stoichiometry is reported. For example, at a temperature of 1000 K and oxygen partial pressure of 10^{-5} atm Lu *et al.* [79] report a value of x in PuO_{2+x} of $\approx 10^{-3}$, several orders of magnitude greater than the value of $\approx 10^{-6}$ found in this study .

4.4 Summary

In summary, using DFT + U with a longitudinal 3k AFM magnetic structure and SOI, the intrinsic point defect concentrations in $PuO_{2\pm x}$ have been predicted as a function of temperature and oxygen partial pressure. The results predict that the defect chemistry of PuO_2 is dominated by oxygen vacancies and interstitials, but that even at high oxygen partial pressures, PuO_2 is found reluctant to form hyper-stoichiometric PuO_{2+x}, with oxygen interstitials present only in very low concentrations irrespective of conditions. Hypo-stoichiometric PuO_{2-x} is predicted, in agreement with the PuO_2 phase diagram [145], and is accommodated by both the $V_O^{\times}$ and V_O^{2+} defects at small values of x, with $V_O^{\times}$ increasingly dominant with increasing x. The little hyper-stoichiometry is accommodated by the O_i^{2-} defect. Aside from increasing the temperature at which perfect stoichiometry occurs, inclusion of vibrational entropy into the defect formation energy calculation was not found to alter which defects accommodate non-stoichiometry in $PuO_{2\pm x}$, as observed in UO_2 [86, 87].

Chapter 5

The impact of americium

This work is published in:

W.D. Neilson, H. Steele, and S.T. Murphy, “Evolving Defect Chemistry of (Pu,Am)-$O_{2\pm x}$”, *The Journal of Physical Chemistry C*, vol. 125, pp. 15560-15568, 2021. [146]

5.1 Introduction

Under storage conditions aged PuO_2 contains a significant ingrowth of Am produced by ^{241}Pu decaying into ^{241}Am. Am builds up relatively quickly due to the short half life of ^{241}Pu (14.4 years), with Am concentrations peaking after approximately 70 years at which point, it too begins to decay faster than it is produced [147]. The investigation in Chapter 4 of the intrinsic defect chemistry of PuO_2 has concluded, among other findings, that pure PuO_2 is very reluctant to form hyper-stoichiometric PuO_{2+x}. In this chapter the modelling is re-visited to assess the role and impact of Am on the defect chemistry of $PuO_{2\pm x}$. Incorporation of Am is predicted to alter the defect chemistry of PuO_2; in a DFT investigation on Pu-Am mixed oxide surfaces, Chen *et al.* [148] report the presence of Am promotes the formation of O vacancies that increase the favourability of molecular adsorption of water on PuO_2 surfaces whilst reducing the favourability of dissociative water adsorption. The consequence of this could be an increased likelihood of chemical reactions, such as the those linked to gas generation discussed in Section 2.2 [148].

Pu-Am mixed oxides have also been investigated as a fuel candidate in the design of the fourth generation (GEN-IV) of nuclear reactors. The oxygen to metal O/M ratio is an important parameter of the fuel and influences multiple thermo-physical properties, including the oxygen potential. Osaka *et al.* [149] experimentally determined the oxygen potential of $(Pu_{0.91}Am_{0.09})O_{2\text{-}x}$ as a function of the O/M ratio, as well as measuring the deviation x from stoichiometry as a function of oxygen partial pressure. Matsumoto *et al.* [150] experimentally studied the oxygen potential of $(Pu_{0.928}Am_{0.072})O_{2\text{-}x}$ at high temperatures as a function of the O/M ratio and constructed point defect equations to describe the deviation x from stoichiometry. A doubly charged vacancy is predicted as the source of all hypo-stoichiometry [150]. Using X-ray absorption spectroscopy Belin *et al.* [151] were able to quantitively determine Pu and Am valences in the reduction process of $(Pu,Am)O_{2\text{-}x}$, validating an earlier prediction made by Osaka *et al.* [149] that all Am(IV) will reduce to Am(III) prior to any reduction in Pu(IV) occurring.

Globally, significant amounts of Pu exist in the environment, a proportion of which is the form of PuO_2 [152]. The subsurface mobility of the material is very complex and is likely impacted by the accumulation of Am which has a different environmental mobility [152, 153]. A better understanding of how PuO_2 continues to evolve and accommodates Am growth is, therefore, of widespread interest. In particular, the oxidation state that Am adopts in PuO_2 is of importance as it will alter, to some degree, the materials surface reactivity, thermo-physical properties, and environmental mobility.

5.2 Methodology

The methodology introduced in Chapter 4 remains applicable to this study, with the following updates made to account for the presence of Am:

DFT simulations are updated to include Am; the 6*s*, 6*p*, 5*f*, 6*d* and 7*s* electrons are treated as valence. In the 96-atom PuO_2 supercells, the Am-defects considered in this study are denoted below:

Interstitials: $\mathrm{Am}_{\mathrm{i}}^{\times}$, $\mathrm{Am}_{\mathrm{i}}^{1+}$, $\mathrm{Am}_{\mathrm{i}}^{2+}$, $\mathrm{Am}_{\mathrm{i}}^{3+}$ and $\mathrm{Am}_{\mathrm{i}}^{4+}$

Oxygen substitutions: $\mathrm{Am}_{\mathrm{O}}^{\times}$, $\mathrm{Am}_{\mathrm{O}}^{1+}$, $\mathrm{Am}_{\mathrm{O}}^{2+}$, $\mathrm{Am}_{\mathrm{O}}^{3+}$, $\mathrm{Am}_{\mathrm{O}}^{4+}$, $\mathrm{Am}_{\mathrm{O}}^{5+}$ and $\mathrm{Am}_{\mathrm{O}}^{6+}$

Plutonium substitutions: $\mathrm{Am}_{\mathrm{Pu}}^{4-}$, $\mathrm{Am}_{\mathrm{Pu}}^{3-}$, $\mathrm{Am}_{\mathrm{Pu}}^{2-}$, $\mathrm{Am}_{\mathrm{Pu}}^{1-}$, $\mathrm{Am}_{\mathrm{Pu}}^{\times}$, $\mathrm{Am}_{\mathrm{Pu}}^{1+}$, $\mathrm{Am}_{\mathrm{Pu}}^{2+}$, $\mathrm{Am}_{\mathrm{Pu}}^{3+}$, $\mathrm{Am}_{\mathrm{Pu}}^{4+}$ and $\mathrm{Am}_{\mathrm{Pu}}^{5+}$

To provide reference for the Am oxidation state and to assess the thermodynamical stability of $(Pu,Am)O_{2\pm x}$, AmO_2 and Am_2O_3 were simulated with DFT. The PBEsol + U functional is used SOI considered, and a $5 \times 5 \times 5$ k-point mesh applied. For AmO_2, *U* is set to 4 eV and transverse 3k AFM order is applied [49]; for A-type Am_2O_3, *U* is set to 6 eV and longitudinal 1k AFM order is applied [140]. The bulk properties produced with these simulation parameters are reasonable when compared to experiment (see Table 5.1).

The vibrational entropy contribution made by each defect continues to be considered. ΔS_{vib} values calculated for the Am extrinsic defects are reported in Table 5.2.

While the chemical potential of Am ($\mu_{\mathrm{Am}}(P_{\mathrm{O}_2}, T)$) can be determined from DFT, here the chemical potential is fitted to reproduce the desired concentration of Am, allowing for comparison with experiment. $\mu_{\mathrm{Am}}(P_{\mathrm{O}_2}, T)$ is determined using linear bisection in DefAP, a mechanism discussed in Section 3.2.5.

Table 5.1: The lattice volume (Å^3), band gap (eV), magnetic moment (μ_{B}/Am ion) and space group for AmO_2 (transverse 3k AFM, SOI, U = 4 eV) and Am_2O_3 (longitudinal 1k AFM, SOI, U = 4 eV) calculated by PBEsol + U.

Oxide	Method	Lattice volume (Å^3)	Band gap (eV)	Magnetic moment (μ_{B}/Am ion)	Space group
AmO_2	PBEsol + U	155.25	1.30	4.85	$Pa\overline{3}$
	Experimental	155.29 [154]	1.3 [155]	-	$Fm\overline{3}m$ [154]
Am_2O_3	PBEsol + U	73.66	2.57	5.66	$P\overline{3}m1$
	Experimental	74.73 [156]	-	-	$P\overline{3}m1$ [156]

Table 5.2: The difference in vibrational entropy of PuO_2 due to the addition of Am extrinsic defects, calculated using the CRG potential.

T (K)	Defect entropy ($\Delta S_{\mathrm{vib}}/k_{\mathrm{B}}$)		
	Am_{i}	Am_{Pu}	Am_{O}
400	6.835	-0.081	5.268
600	7.322	-0.081	4.711
800	7.810	-0.081	4.479
1000	8.332	-0.081	4.363
1200	8.796	-0.081	4.305
1400	9.307	-0.081	4.259
1600	9.667	-0.070	4.236
1800	9.922	-0.070	4.224
2000	10.305	-0.081	4.201

Finally, the formula to calculate the deviation in stoichiometry, x in $PuO_{2\pm x}$ is updated to reflect the presence of Am. Using the concentration of a defect summed over all charge states, w, y and z in $Pu_{1+w}Am_yO_{2+z}$ are given by:

$$w = [\mathrm{Pu_i}] - [\mathrm{V_{Pu}}] - [\mathrm{Am_{Pu}}] \tag{5.1}$$

$$y = [\mathrm{Am_O}] + [\mathrm{Am_{Pu}}] + [\mathrm{Am_i}] \tag{5.2}$$

$$z = [\mathrm{O_i}] - [\mathrm{V_O}] - [\mathrm{Am_O}] \tag{5.3}$$

x in $(Pu_{1-y}Am_y)O_{2+x}$ or $-x$ in $(Pu_{1-y}Am_y)O_{2-x}$ can be defined as:

$$2 + x = \frac{2+z}{1+w+y} \tag{5.4}$$

$$x = \frac{2 + [\mathrm{O_i}] - [\mathrm{V_O}] - [\mathrm{Am_O}]}{1 + [\mathrm{Pu_i}] - [\mathrm{V_{Pu}}] + [\mathrm{Am_i}] + [\mathrm{Am_O}]} - 2 \tag{5.5}$$

5.3 Results & discussions

The formation energies of the Am-based extrinsic defects are plotted as a function of the Fermi level at 1000 K and an oxygen partial pressure of 0.10 atm in Figure 5.1. Figure 5.1 displays the charge state of each defect that corresponds to the lowest formation energy at a given position in the band gap. It is clear from Figure 5.1 that the Am_{Pu} defects have significantly lower formation energies than Am_O and Am_i defects across the whole band gap. This result is found to be consistent at both high and low oxygen partial pressures and Am concentrations. This shows that in $(Pu,Am)O_2$, Am is preferentially accommodated as a substitutional defect on the Pu site. The most energetically stable charge state of Am_{Pu} is seen to vary across the band gap, with four states in total dominant at one time. However, it is the Am_{Pu}^{1-} and $Am_{Pu}^{\times}$ charge states that dominate across the majority of the band gap, suggesting that it is these two defects that accommodate americium under most equilibrium conditions. By studying the electron occupation of the Am atom in the simulated defect-containing supercells, it was possible to infer an oxidation state for americium of +III and +IV in $\mathrm{Am}_{\mathrm{Pu}}^{1-}$ and $\mathrm{Am}_{\mathrm{Pu}}^{\times}$, respectively. The results of a Bader charge analysis [157] (Table 5.3) helps confirm this result, using AmO_2 and Am_2O_3 as reference oxides for the Am(IV) and Am(III) charge states, respectively. Pu remains in the +IV oxidation state, regardless of defect. $\mathrm{Am}_{\mathrm{Pu}}$ defects do not cause significant distortion of the PuO_2 lattice, only a small distortion of the eight nearest oxygen atoms is observed, as shown in Figure 5.2. In cells containing the $\mathrm{Am}_{\mathrm{Pu}}^{1-}$ defect, the O-Am bond length is just 0.05 Å higher than the O-Pu bond length of 2.34 Å in Am-free PuO_2; this increase is lower in cells containing the $\mathrm{Am}_{\mathrm{Pu}}^{\times}$ defect. This is explained and supported by the reported crystallography: Am(IV) and Am(III) with eight-fold coordination have ionic radii of 0.95 Å and 1.09 Å, respectively [158]. Pu(IV) with eight-fold coordination has an ionic radius of 0.96 Å [158].

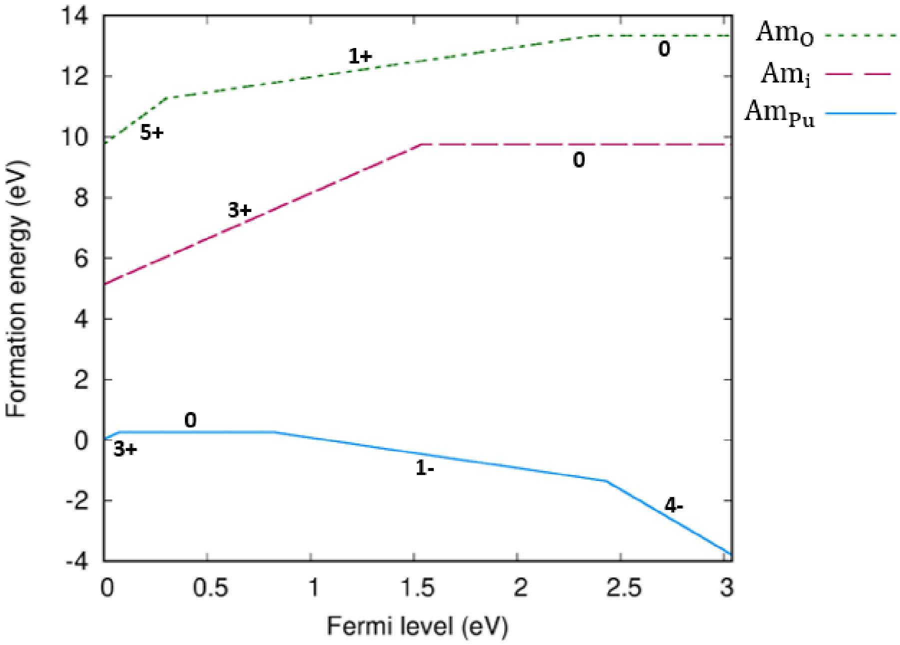

Figure 5.1: Defect formation energies for $\mathrm{Am}_{\mathrm{Pu}}$, Am_{O} and Am_{i} defects in $(Pu_{1-y}Am_y)O_{2\pm x}$ (y = 0.001) as a function of Fermi energy. Calculated at 1000 K and an oxygen partial pressure of 0.10 atm. Only the charge state with the lowest formation energy for a given Fermi level is shown for each defect, represented with numeric label.

Table 5.3: Bader charge (|e|) of Am in Am_{Pu} defects and Am oxides.

$Am_{Pu}^{\times}$	2.44
Am_{Pu}^{1-}	2.02
AmO_2 (Am(IV))	2.38
Am_2O_3 (Am(III))	1.96

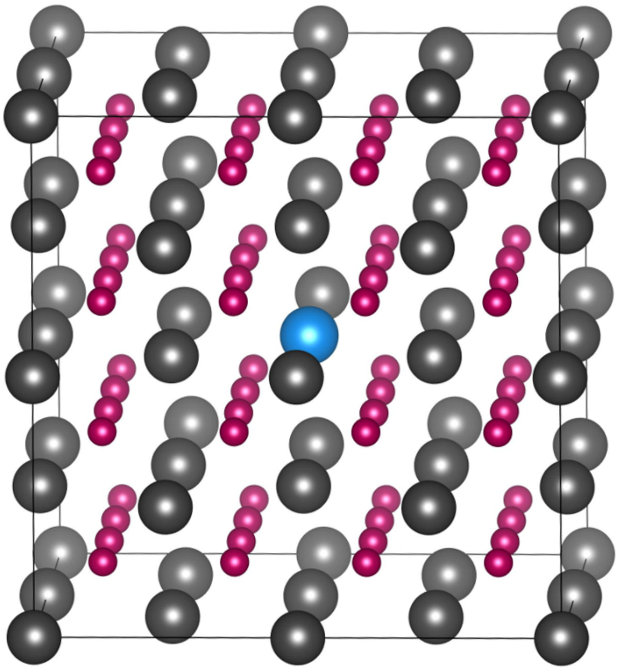

Figure 5.2: Final relaxed structure for the Am_{Pu}^{1-} defect in PuO_2. Plutonium, americium and oxygen are represented with grey, blue and red spheres, respectively.

The Brouwer diagrams in Figure 5.3 show the defect concentrations in $(Pu_{1\text{-}y}Am_y)$-$O_{2\pm x}$ as a function of oxygen partial pressure at 1000 K with comparison made for y values of 0.0 and 0.001. At all values of oxygen partial pressure tested, Am is seen to be accommodated as substitutional defects on Pu sites, with concentrations of Am interstitials and O substitutions negligible to such extent they are not shown on the Brouwer diagrams. The Brouwer diagram shows that as the O/M ratio in $(Pu_{1\text{-}y}Am_y)O_{2\pm x}$ (y = 0.001) decreases, the dominant extrinsic defect transitions from $Am_{Pu}^{\times}$ to Am_{Pu}^{1-}. As previously discussed, this transition corresponds to a reduction in the oxidation state for Am of +IV to +III. This supports the experimental work of Belin *et al.* [151] as well as the model of Osaka *et al.* [149] that find and predict all Am is reduced prior to Pu reduction when the O/M ratio decreases from stoichiometry. Charge compensation for the Am_{Pu}^{1-} defect is provided by holes in the valence band at high oxygen partial pressures, before V_O^{2+} defects compensate when their concentration becomes sufficiently high. Figure 5.3 shows that when Am(IV) is the dominant oxidation state, the concentration of Am(III) ions remains elevated and stable: Am(III) contributes ∼17% to the total Am concentration in the region of stability in Figure 5.3. Consequently the concentrations of holes also remains high to provide charge compensation, with concentrations several magnitudes higher than Am-free PuO_2. It can therefore be said that Am behaves as a p-type dopant, acting to make PuO_2 more conductive.

By comparing the two Brouwer diagrams in Figure 5.3 it is observed that Am incorporation also impacts the intrinsic defect chemistry. The defect responsible for hypo-stoichiometry remains oxygen vacancies, however the presence of Am is observed to alter the favoured oxygen vacancy charge state; the Brouwer diagrams show that the doubly charged V_O^{2+} defect dominates. In contrast, in $PuO_{2\text{-}x}$ the neutral oxygen vacancy was preferred. Increased Am concentration promotes positively charged oxygen vacancies, as higher concentrations are required to charge compensate (Am_{Pu}^{1-}). Hyper-stoichiometry remains very low and accommodated by oxygen interstitials. In pure PuO_{2+x} the O_i^{2-} interstitial is dominant. However,

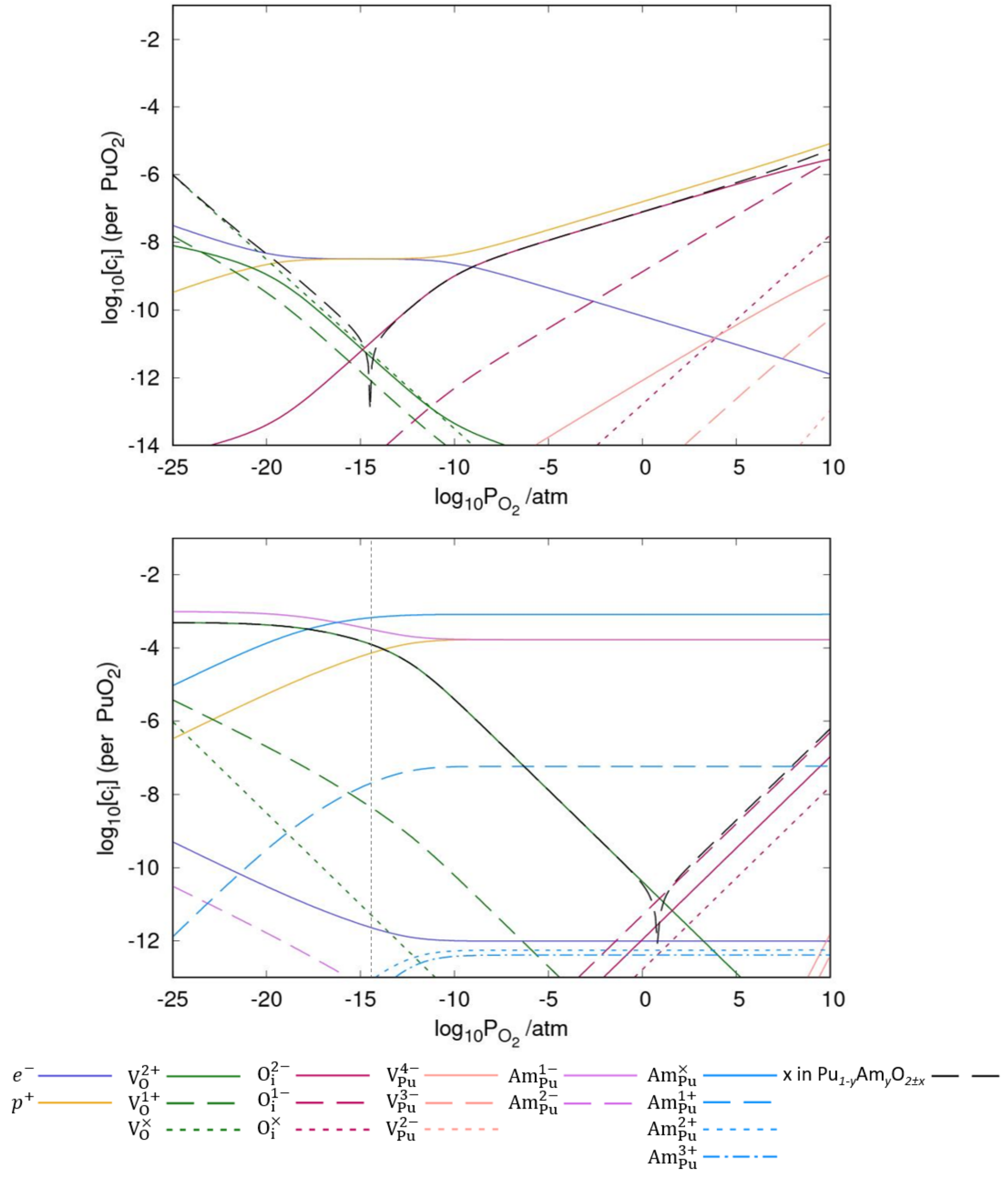

Figure 5.3: Brouwer diagrams showing the defect concentrations and value of x in $(Pu_{1-y}Am_y)O_{2\pm x}$ as a function of oxygen partial pressure at a temperature of 1000 K and y value of 0.0 (top) and 0.001 (bottom). At partial pressures to the left of the vertical dashed line, $(Pu,Am)O_{2\pm x}$ is predicted to be thermodynamically unstable with respect to Am_2O_3. To the left and right of the minima of the black line, the diagram records the calculated value of $\log_{10}[x]$ in PuO_{2-x} and PuO_{2+x}, respectively.

the dominant charge state is seen to be altered with the addition of Am: the $\mathrm{O_i^{1-}}$ interstitial is now dominant. Prodan *et al.* [31] have previously reported that $\mathrm{O_i^{1-}}$ is the most energetically favourable charge state for the oxygen interstitial. Acting as a p-type dopant, increasing the Am concentration lowers the Fermi level of the system to such a degree that $\mathrm{O_i^{1-}}$ becomes the interstitial with the lowest formation energy and $\mathrm{V_O^{2+}}$ is the vacancy with the lowest formation energy.

To assess the reliability of the point defect model, the results are compared to the experimental studies of Osaka *et al.* [149] and Matsumoto *et al.* [150] who studied the O/M ratio in $\mathrm{(Pu,Am)O_{2\text{-}x}}$. By matching the temperature and Am concentrations of the experiments it was possible to determine how x in $\mathrm{(Pu,Am)O_{2\text{-}x}}$ changes with oxygen partial pressure. The results are compared to these previous experimental works in Figure 5.4. It is seen that both the trends and absolute values of x are very well replicated by the model.

From Figures 5.3 & 5.4 an evolving dependence of $[\mathrm{V_O^{2+}}]$ and x on the oxygen partial pressure is seen. At near stoichiometry, the model shows that the presence of Am results in $[e^-] << [h^+]$, in contrast with Am-free $\mathrm{PuO_2}$ where $[e^-] = [h^+]$ at near stoichiometry. Therefore, to construct equations describing the defect chemistry of $\mathrm{(Pu,Am)O_{2\text{-}x}}$, it cannot be said that $[e^-] = [h^+]$ as suggested by Matsumoto *et al.* [150]. Instead, it is proposed that at low concentrations of $\mathrm{V_O^{2+}}$ and near stoichiometry, the formation of $\mathrm{V_O^{2+}}$ is charge compensated by the removal of holes, which exist at concentrations many orders of magnitude greater than $\mathrm{V_O^{2+}}$ at near stoichiometry. The defect reaction and corresponding equilibrium constant (k_1) is written as:

$$\mathrm{O_O^{\times}} + 2p^+ \rightleftharpoons \frac{1}{2}\mathrm{O_2} + \mathrm{V_O^{2+}} \tag{5.6}$$

$$k_1 = [\mathrm{V_O^{2+}}][p^+]^{-2}\mathrm{P_{O_2}^{\frac{1}{2}}} \tag{5.7}$$

Figure 5.3 illustrates that at near stoichiometry, the concentration of holes can be considered fixed. It can therefore be shown that $[\mathrm{V_O^{2+}}]$ (and x in $\mathrm{(Pu,Am)O_{2-x}}$) is

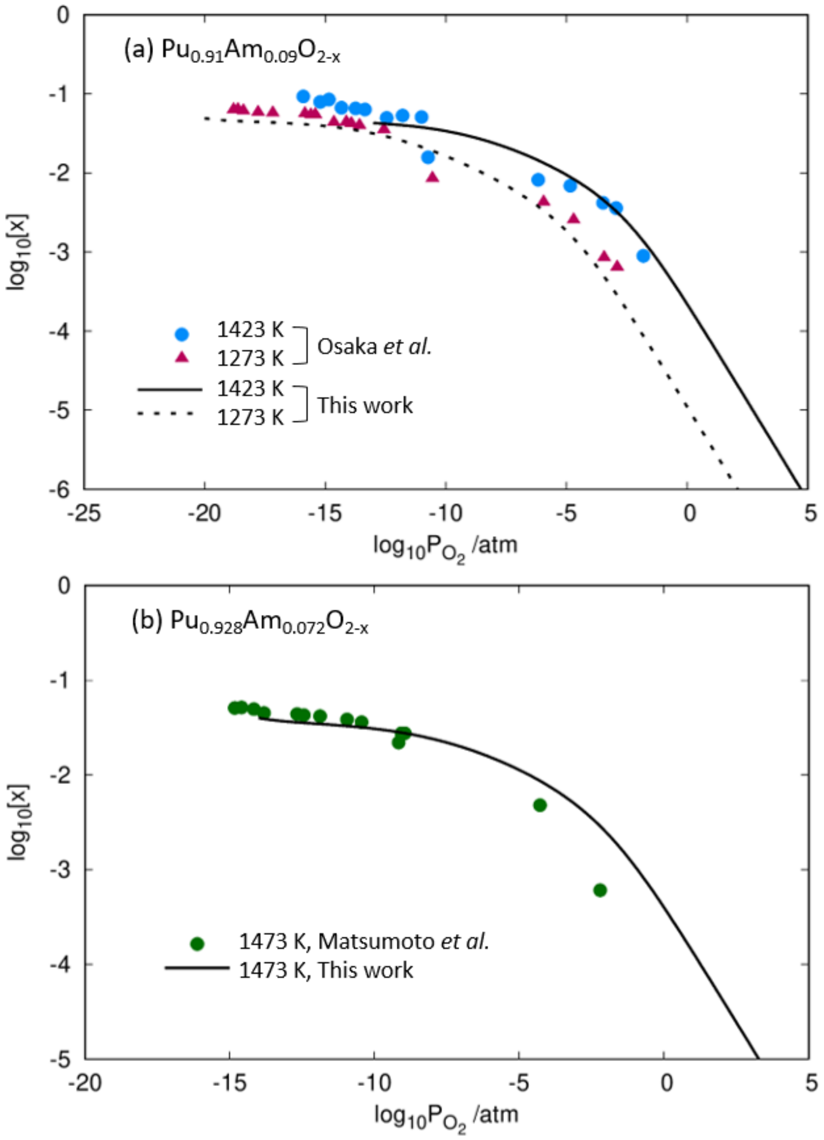

Figure 5.4: Values of x in $(Pu_{1-y}Am_y)O_{2-x}$ as a function of oxygen partial pressure at y values of a) 0.09 and b) 0.072, with comparison to the experimental results of Osaka *et al.* [149] and Matsumoto *et al.* [150].

proportional to $P_{O_2}^{-\frac{1}{2}}$:

$$x = [V_O^{2+}] = k_1^{'} P_{O_2}{}^{-\frac{1}{2}} \tag{5.8}$$

Figure 5.3 shows that when oxygen partial pressures are low enough to cause sufficiently high concentrations of V_O^{2+}, reduction of Am begins. The defect reaction and corresponding equilibrium constant (k_2) becomes:

$$O_O^{\times} + 2Am_{Pu}^{\times} \rightleftharpoons \frac{1}{2}O_2 + V_O^{2+} + 2Am_{Pu}^{1-} \tag{5.9}$$

$$k_2 = [V_O^{2+}][Am_{Pu}^{1-}]^2[Am_{Pu}^{\times}]^{-2}P_{O_2}^{\frac{1}{2}} \tag{5.10}$$

In the reducing region, $[Am_{Pu}^{1-}] = 2\ [V_O^{2+}]$. Equation 5.10 can be rearranged to show that $[V_O^{2+}]$ (and x in (Pu,Am)O_{2-x}) is proportional to both $P_{O_2}^{-\frac{1}{6}}$ and $[Am_{Pu}^{\times}]^{\frac{2}{3}}$ (see Equation 5.11). This explains the curve seen in Figures 5.3 & 5.4: as Am(IV) is reduced, the rate of V_O^{2+} formation decreases and when reduction is complete, $[V_O^{2+}]$ remains constant.

$$x = [V_O^{2+}] = k_2[Am_{Pu}^{\times}]^{\frac{2}{3}}P_{O_2}^{-\frac{1}{6}} \tag{5.11}$$

As oxygen partial pressure is reduced further, the value of x in (Pu,Am)O_{2-x} will continue to evolve. The start of reduction in Pu is predicted to result in the formation of defect clusters [150], however both cluster formation and the higher defect concentrations at low O/M ratios are outside the capabilities of the point defect model.

Figure 5.5 shows the impact of varying temperature on the defect chemistry of $(Pu_{1-y}Am_y)O_{2\pm x}$ where y = 0.0 or 0.001. Am(III) concentration increases with temperature, becoming the dominant oxidation state at high temperature. The Am(IV): Am(III) ratio increases with decreasing temperature, and at low temperatures the Am in $(Pu_{1-y}Am_y)O_{2\pm x}$ is composed entirely of Am(IV). This is supported by the recent finding of Emerson *et al.* [152] who measured the Am L_3-edge X-ray absorption near edge structure (XANES) spectrum of aged PuO_2 samples finding a spectrum characteristic of $Am(IV)O_2$.

The impact of varying the concentration of Am (y in $(Pu_{1-y}Am_y)O_{2\pm x}$) is shown in Figure 5.6. Regardless of its concentration, Am is always accommodated in either the +IV or +III oxidation states, with the ratio of the two oxidation states varying quite significantly depending on the concentration of Am present. At very low concentrations, Am(III) is the dominant oxidation state, whereas accumulation of Am in PuO_2 results in promotion of the +IV oxidation state. Although the Am(IV) concentration rises more rapidly, the Am(III) concentration also continues to increase as Am accumulates accompanied by a concomitant increase in conductivity of the material. Increasing Am concentration can be seen to create a more reducing environment; oxygen vacancy concentrations increase with increasing Am, oxygen interstitial concentrations fall. Therefore at any condition, the O/M ratio is lower if Am concentration in $PuO_{2\pm x}$ is increased. This is a similar result to that found in $(U,Am)O_{2\pm x}$ where increased Am content is seen to hinder oxidation [159]. PuO_2 is much more resistant to oxidation than UO_2 and it is seen here that adding Am further increases this resistance.

In Figures 5.3, 5.5 & 5.6, the dashed vertical lines highlight the point at which the model predicts $(Pu,Am)O_{2\pm x}$ is thermodynamically unstable and will decompose into a combination of two tested Am-oxides: AmO_2 and A-type Am_2O_3. The model predicts that at low oxygen partial pressures, low temperatures, or high Am concentrations, $(Pu,Am)O_{2\pm x}$ becomes unstable. To precipitate out of the material, the Am-oxides would require significant energy to overcome barriers to migration within $(Pu,Am)O_{2\pm x}$. As it is found that at high temperatures $(Pu,Am)O_{2\pm x}$ is stable, it is unlikely that at the conditions of instability found $(Pu,Am)O_{2\pm x}$ would have the energy to decompose into the two Am-oxides, despite being thermodynamically favourable. Improvement may also be required in the DFT model for AmO_2 and Am_2O_3. Specifically, the best approach to modelling with the DFT + U

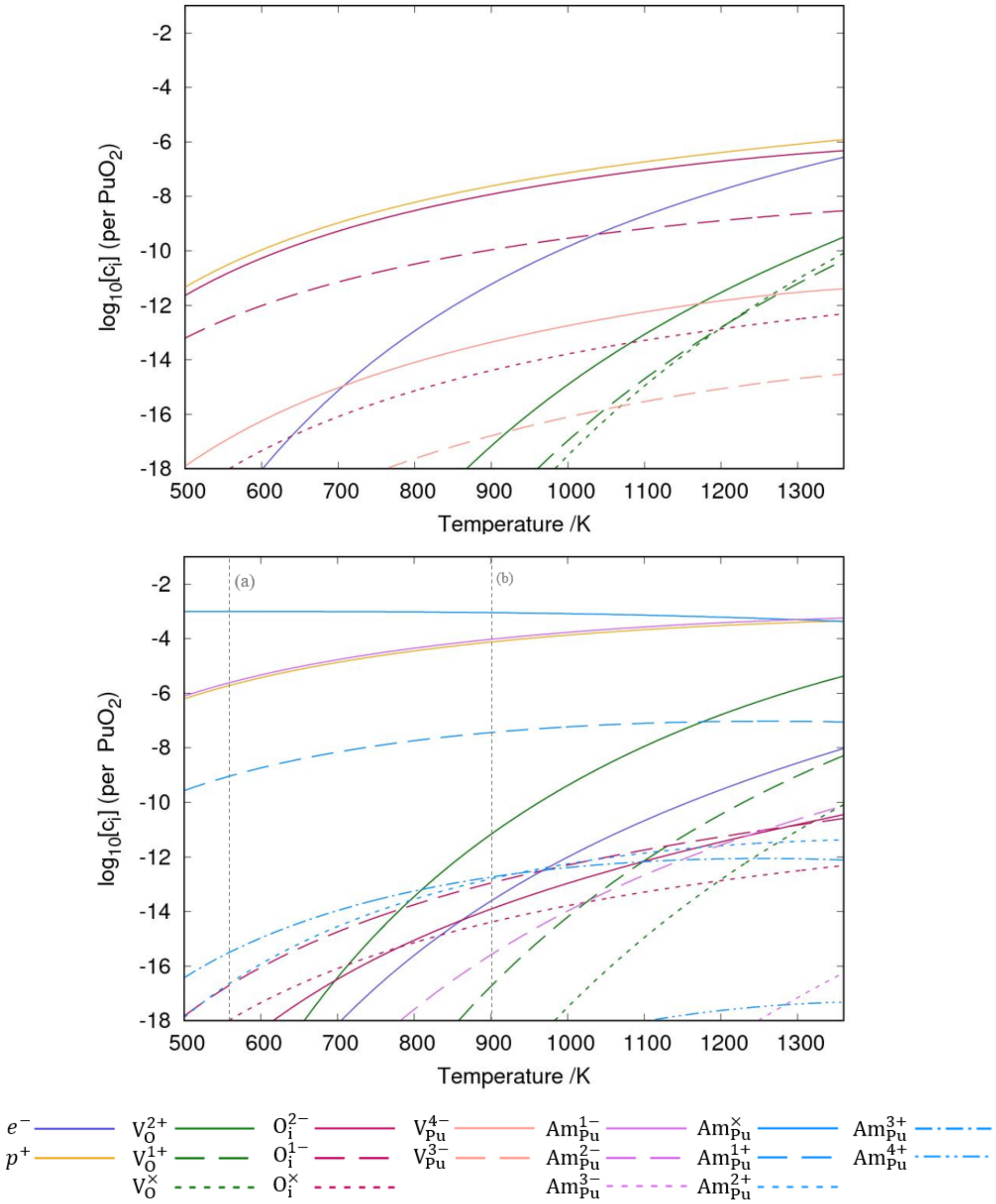

Figure 5.5: The defect concentrations in $(Pu_{1\text{-}y}Am_y)O_{2\pm x}$ as a function of temperature at an oxygen partial pressure of 0.1 atm and y value of 0.0 (top) and 0.001 (bottom). At temperatures to the left of the vertical dashed lines (a) and (b), $(Pu,Am)O_{2\pm x}$ is predicted to be thermodynamically unstable with respect to Am_2O_3 and AmO_2, respectively.

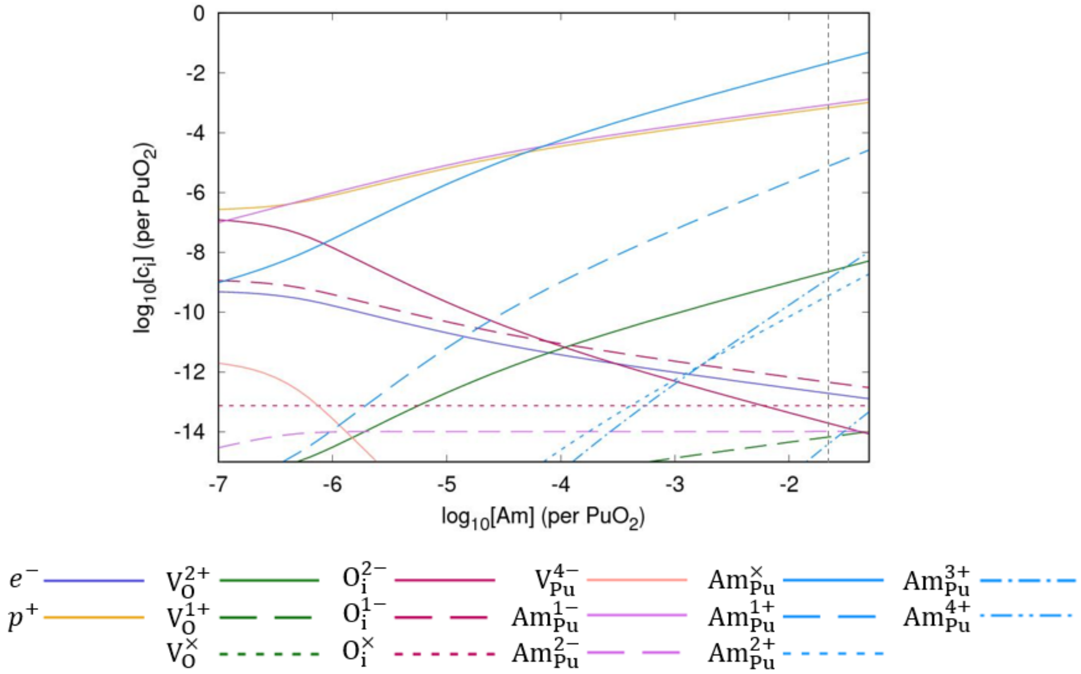

Figure 5.6: The defect concentrations in $(Pu_{1-y}Am_y)O_{2\pm x}$ as a function of the concentration of Am at an oxygen partial pressure of 0.1 atm and temperature of 1000 K. At Am concentrations to the right of the vertical dashed line, $(Pu,Am)O_{2\pm x}$ is predicted to be thermodynamically unstable with respect to AmO_2.

approach remains uncertain. Caution is therefore attached to the results regarding thermodynamic stability.

5.4 Summary

The mode of Am incorporation within PuO_2 and the impact Am makes to the defect chemistry of the host have been investigated using DFT and a point defect model. At all conditions and Am concentrations investigated, Am is found to be accommodated on Pu vacancies, with Am existing in a combination of the +IV and +III oxidation states. Reduction in the O/M ratio of $(Pu,Am)O_{2\pm x}$ is seen to change the dominant extrinsic defect from $Am_{Pu}^{\times}$ to Am_{Pu}^{1-} corresponding to reduction of Am(IV) to Am(III). Am(IV) is promoted by low temperatures and high Am concentrations. The addition of Am results in the concentration of holes in the valence band increasing by multiple orders of magnitude compared to Am-free PuO_2, in order to provide charge compensation to Am(III). It is, therefore, anticipated that the presence of Am increases the electrical activity of PuO_2.

Chapter 6

Helium behavior

This work is published in:

W.D. Neilson, H. Steele, and S.T. Murphy, "Accommodation of helium in $PuO_{2\pm x}$ and the role of americium", *Physical Chemistry Chemical Physics*, vol. 24, pp. 8245-8250, 2022. [160]

6.1 Introduction

He is produced in significant quantities over storage time periods due to the α-decay of Pu with a portion accumulating in the head space of sealed PuO_2 storage canisters [37]. The release of He from the oxide lattice has been shown to be affected by the microstructure and the presence of defects [161]. Studies have demonstrated that at temperatures typical of storage, PuO_2 pellets are able to accommodate significant amounts of radiogenic He with only small fractions released from the lattice [161, 162, 163]. Mulford *et al.* [164] studied an inventory of PuO_2 storage containers aged between 23 and 34 years, finding approximately 75 % of the He produced had been retained in the oxide lattice. Similarly, Ronchi *et al.* [163] found that a 25 year old $^{239}PuO_2$ sample trapped 80-90 % of its generated helium inventory. In contrast, powders in storage have exhibited much weaker retention of He, showing up to 80 % of the He generated is released to the head space.

Previous theoretical investigations have employed DFT to study He incorporation in $PuO_{2\pm x}$. Freyss *et al.* [165, 166] report that He is accommodated on oxygen vacancies under conditions of hypo-stoichiometry, with the interstitial site favoured for PuO_2 and PuO_{2+x}. It should be noted that this study used very small (12 atom) PuO_2 simulation supercells, which typically results in poor convergence of defect formation energies. Tian *et al.* [121] introduced He into 96 atom supercells and predict that the favourable site for He is O vacancies, interstitial sites and Pu vacancies for hypo-, perfect and hyper-stoichiometry, respectively. This result relied on a point defect model constructed for UO_2. Higher oxidation states in UO_2 allow for large hyper-stoichiometry provided by clusters of oxygen interstitials [87]; a different point defect model is required to correctly describe the defect chemistry of $PuO_{2\pm x}$. The preceding chapters have shown that PuO_2 is reluctant to exist as PuO_{2+x} with small values of x predicted to be accommodated by O interstitials with Pu vacancies at concentrations several magnitudes lower. Therefore, while helium may be easily accommodated by plutonium vacancy defects, these are likely to be rare. In this chapter, the PuO_2 point defect model constructed in this thesis will be used to investigate the mode of He incorporation within PuO_2 under a range of external conditions (oxygen partial pressure and temperature) and concentrations of He.

6.2 Methodology

Once again, the methodology introduced in Chapter 4 is employed, with adaptions made to study He. Most significantly, the DFT-D dispersion correction is applied in order to account for long-range van der Waals dispersion interactions. The DFT-D3 scheme [61] was applied to all simulations, including a re-simulation of

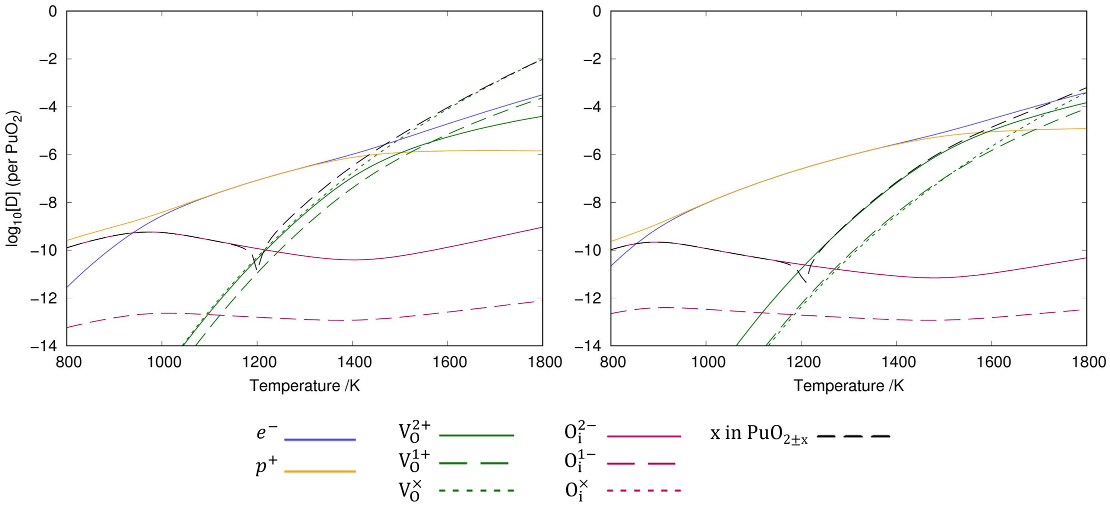

Figure 6.1: The impact of dispersion-corrected density functional theory: the intrinsic defect chemistry of PuO_2 as a function of temperature, where the defects were simulated without (left) or with (right) the DFT-D3 method. To the left and right of the minima of the black line, the diagram records the calculated value of $\log_{10}[x]$ in $PuO_{2\text{-x}}$ and PuO_{2+x}, respectively.

the intrinsic defects from Chapter 4 and the defect-free PuO_2 unit- and supercells. Applying the DFT-D3 scheme has a minor impact on the intrinsic defect chemistry, as evidenced by Figure 6.1. The two plots — which compare the defect chemistry with, and without, the DFT-D3 method — appear very similar, but interestingly the dispersion interaction is seen to promote the V_O^{2+} defect as the defect responsible for hypo-stoichiometry (when x in $PuO_{2\text{-x}}$ is small).

The He-defects considered in this study are denoted below:

Interstitial: $He_i^{\times}$

Oxygen substitutions: $He_O^{\times}$, He_O^{1+} and He_O^{2+}

Plutonium substitutions: He_{Pu}^{4-}, He_{Pu}^{3-}, He_{Pu}^{2-}, He_{Pu}^{1-} and $He_{Pu}^{\times}$

A visual representation of the supercell with He positioned at an octahedral interstitial site is shown in Figure 6.2. The energy required to incorporate He at a interstitial site or pre-existing vacancy defect is defined as the incorporation energy:

$$E_{\mathrm{inc}}(\mathrm{He},x) = E_{\mathrm{He},x} - E_x - E_{\mathrm{He}} \tag{6.1}$$

where, $E_{\mathrm{He},x}$ and E_x are the DFT energies of He at site x and an empty site x, respectively. E_{He} is the energy of an isolated He atom. The incorporation energy is insufficient to discuss the actual likelihood of incorporation of He at a given site. Therefore, DefAP is used to describe a defect's concentration dependence in PuO_2 on temperature, oxygen partial pressure and quantity of He. This begins by defining a defect's formation energy:

$$\Delta H_{\mathrm{f}}^{i} = E_{\mathrm{defect}}^{\mathrm{DFT}} - E_{\mathrm{perfect}}^{\mathrm{DFT}} \pm \sum_{\alpha} n_{\alpha}\mu_{\alpha} + q_{\mathrm{i}}\mu_{\mathrm{e}} + E_{\mathrm{corr}} \tag{6.2}$$

This equation is different to that used in the two preceding chapters: the vibrational entropy contribution has been discarded. There is no reliable empirical potential to describe the Pu-He interaction, which is required for the calculation of vibrational entropies. Fortunately, aside from increasing the temperature at which perfect stoichiometry occurs, inclusion of vibrational entropy into the defect formation energy calculation has been shown not to alter which defects accommodate non-stoichiometry in $PuO_{2\pm x}$ (see Chapter 4), in contrast to in UO_2 [86, 87]. This was true even at conditions where the vibrational entropy contribution is most significant: high temperatures. The primary influence of the vibrational entropy contribution is to decrease the favourability of the cation defects. However, in PuO_2, Pu interstitials and vacancies are found to be unfavourable, even when vibrational entropy is omitted. The vibrational entropy contribution therefore acts only to further suppress formation of these defects; omitting its contribution is, therefore, deemed acceptable.

To calculate the chemical potential of He, the total He concentration is specified and DefAP calculates μ_{He} and the blend of He defects that delivers the specified concentration of He. This continues to be a very useful method, as the concen-

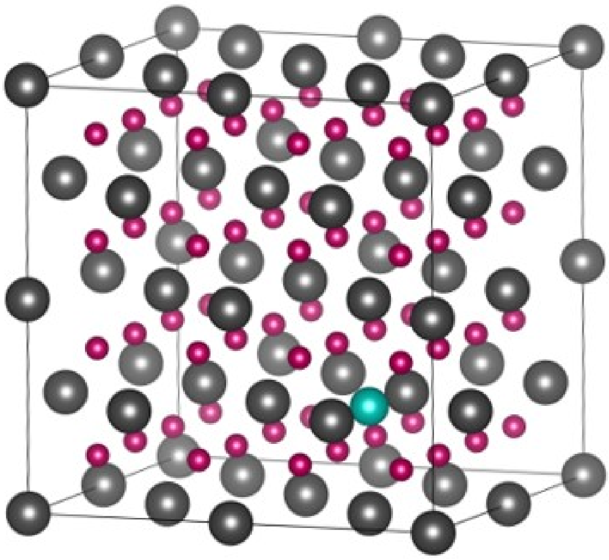

Figure 6.2: The simulation supercell used for PuO_2 with a helium atom incorporated at an octahedral interstitial site. Plutonium, oxygen and helium are represented with grey, red and blue spheres, respectively.

tration of He in PuO_2 can approximated from experimental findings and/or decay equations and the information coveted is how this concentration is accommodated within the host lattice.

Unlike the incorporation energy, the solution energy takes into account the population of the different accommodation sites for He and is, therefore, dependent on temperature, oxygen partial pressure and the quantity of He. The solution energy is defined as:

$$E_{\mathrm{sol}}(\mathrm{He},x) = E_{\mathrm{inc}}(\mathrm{He},x) + \Delta H_{\mathrm{f}}^{x} \tag{6.3}$$

The formula used to calculate the deviation in stoichiometry, x in $PuO_{2\pm x}$ is updated to reflect the presence of He. Using the concentration of a defect summed over all charge states, x in PuO_{2+x} or $-x$ in PuO_{2-x} is defined as:

$$x = \frac{2 + [\mathrm{O_i}] - [\mathrm{V_O}] - [\mathrm{He_O}]}{1 + [\mathrm{Pu_i}] - [\mathrm{V_{Pu}}] - [\mathrm{He_{Pu}}]} - 2 \tag{6.4}$$

Table 6.1: The incorporation and solution energies for He at different sites within PuO_2. Comparison to the incorporation energy calculated in past studies is presented (Note these studies do not describe the charge state of the incorporation site). The solution energies are calculated at a temperature of 1000 K, oxygen partial pressure of 10^{-11} atm and a fixed He concentration of 0.001 atoms per PuO_2, conditions where PuO_2 is predicted to have perfect stoichiometry.

Site	Charge	Incorporation energy (eV) This work	 Other studies	Solution energy (eV) This work
Oxygen vacancy	2+	0.38	0.34[121] -0.5[165]	3.00
	1+	0.66		3.62
	0	0.79		3.78
Plutonium vacancy	4-	0.16	0.36[121] 0.7 [165]	5.05
	3-	0.16		5.78
	2-	0.16		6.80
	1-	0.16		8.01
	0	0.17		9.41
Interstitial	0	0.89	2.73[121] 0.4[165] 1.02[78]	0.89

6.3 Results & discussions

Table 6.1 reports the predicted incorporation and solution energies for He at different sites within PuO_2. The solution energies are dependent on environmental variables: a temperature of 1000 K, an oxygen partial pressure of 10^{-11} atm, and a fixed He concentration of 0.001 atoms per PuO_2 — conditions where PuO_2 is predicted to have perfect stoichiometry — is selected. Table 6.1 shows that the plutonium vacancy site is predicted to have the lowest incorporation energy for He, but the highest solution energy due to the low availability of this site at equilibrium conditions. The interstitial site has the lowest solution energy (note that the solution energy is the same as the incorporation energy as no other atoms must be displaced). In Figure 6.3, the formation energies ($\Delta H_{\mathrm{f}}^{\mathrm{i}}$) of the He extrinsic defects are plotted as a function of the Fermi level, at the same conditions described above for the solution energies in Table 6.1. It is seen that the interstitial site is the accommodation site with the lowest formation energy across the majority of

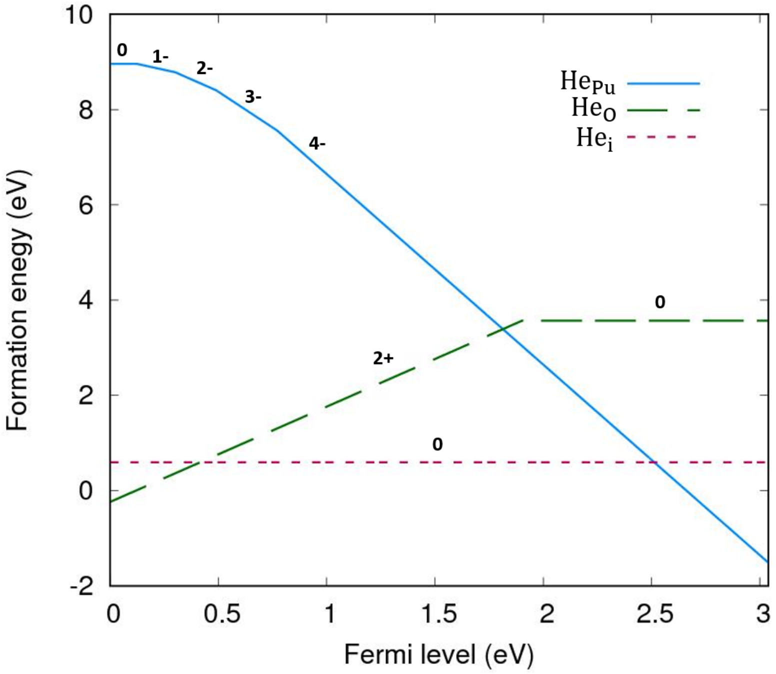

Figure 6.3: Defect formation energies for He_{Pu}, He_O and He_i defects in PuO_2 as a function of the Fermi energy. Calculated at 1000 K and an oxygen partial pressure of 10^{-10} atm. Only the charge state with the lowest formation energy for a given Fermi level is shown for each defect, represented with a numeric label.

the bandgap. Only at the extremities of the bandgap, where the Fermi level is very close to the valence band or conduction band do the oxygen and plutonium vacancies have the lowest formation energy. This result suggests that it will be the interstitial site that is the preferred accommodation site for He under a wide range of conditions.

Presented in Figure 6.4 is a Brouwer diagram showing the defect concentrations and value of x in $PuO_{2\pm x}$ as a function of oxygen partial pressure at a temperature of 1000 K and fixed He concentration of 0.001 atoms per PuO_2. Multiple defects were predicted to have a concentrations of less than 10^{-15} defects per PuO_2 in the oxygen partial pressure range used, so are omitted from the plot. Figure 6.4 shows that for a wide range of oxygen partial pressures encompassing both hypo- and hyper- stoichiometric conditions, the interstitial site is preferred for accommodation of He. The PuO_2 point defect model predicts that hyper-stoichiometry is

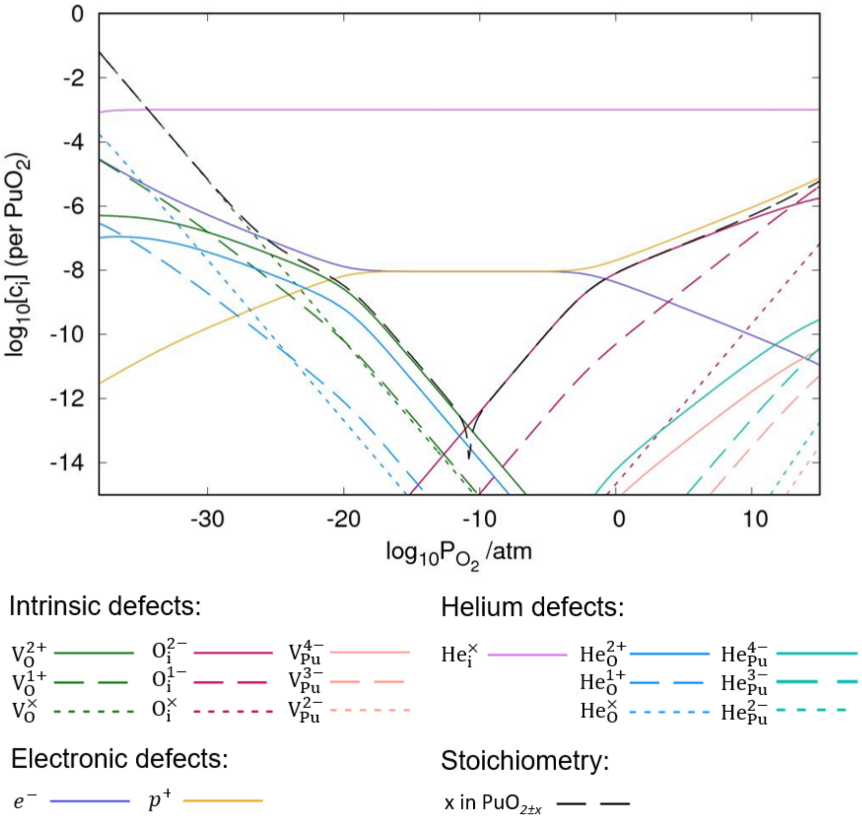

Figure 6.4: Brouwer diagram showing the defect concentrations and value of x in $PuO_{2\pm x}$ as a function of oxygen partial pressure at a temperature of 1000 K and fixed He concentration of 0.001 atoms per PuO_2. To the left and right of the minima of the black line, the diagram records the calculated value of $\log_{10}[x]$ in $PuO_{2\text{-}x}$ and PuO_{2+x}, respectively.

very unfavourable; even at extremely high oxygen partial pressures, x in PuO_{2+x} never exceeds 10^{-5}. What hyper-stoichiometry there is, is accommodated by oxygen interstitials, not plutonium vacancies. Therefore, under conditions of thermal equilibrium, plutonium vacancies are an unviable accommodation site for He in PuO_2. Hypo-stoichiometry is much more favourable in PuO_2, and the predictions made by the point defect model conform to this expectation.

Figure 6.5 shows the predicted defect chemistry in PuO_{2-x} as a function of x at a temperature of 1000 K and fixed He concentration of 0.001 atoms per PuO_2. It is predicted that even at relatively large values of x in PuO_{2-x}, the interstitial site

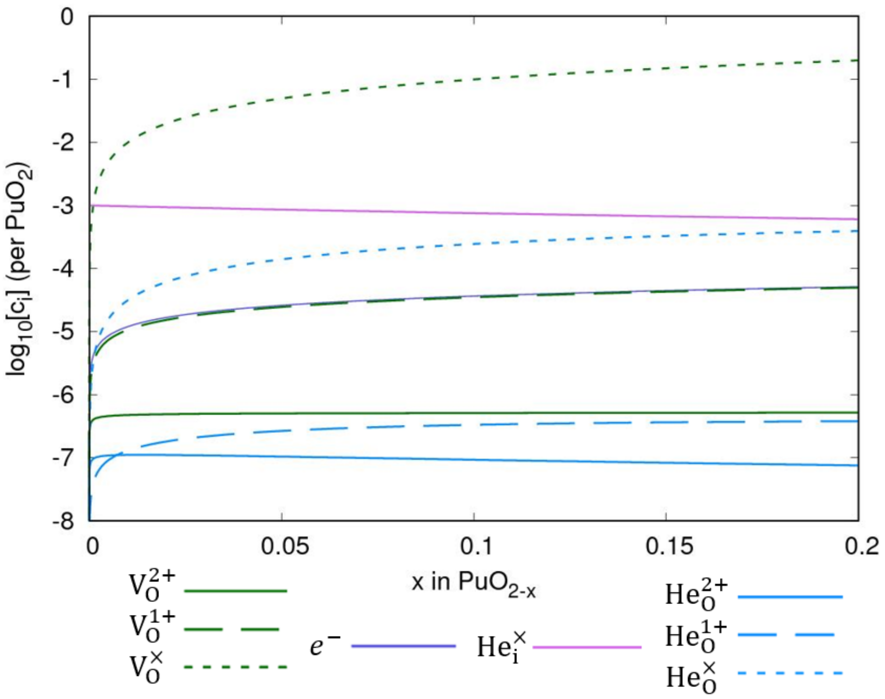

Figure 6.5: The concentration of defects in PuO_{2-x} as a function of x at a temperature of 1000 K and fixed He concentration of 0.001 atoms per PuO_2.

remains the preferred accommodation site for He. The amount of He accommodated on O vacancies increases with increasing hypo-stoichiometry, and the $He_O^{\times}$ defect approaches concentrations of similar magnitude to concentrations of $He_i^{\times}$, but only at significant hypo-stoichiometry.

At the VBM, of all the He extrinsic defects tested, He_O^{2+} is predicted to have the lowest formation energy at all hypo-stoichiometric conditions. The formation energy of positively charged defects increases as the Fermi level rises, whereas charge neutral defects have a formation energy that is independent of the Fermi level. In this system, the point defect model predicts that the Fermi level is sufficiently high that $He_i^{\times}$ is the He defect with the lowest formation energy for the wide range in stoichiometry tested.

The incorporation site for He is found to be independent of the total He concentration. As discussed, He is incorporated into PuO_2 as $He_i^{\times}$, or under certain conditions a proportion is $\mathrm{He}_{\mathrm{O}}^{\times}$. Both these defects are neutrally charged. Consequently, the intrinsic defect chemistry is not affected by the presence of He; the system does not need to adjust to fulfil electrical charge neutrality due to the presence of He. For the point defects investigated in this study, temperature is found not to directly affect the accommodation site for He in PuO_2, but does so indirectly by impacting the stoichiometry. Increasing temperature promotes hypo-stoichiometry, therefore the concentration of He_{O} defects increases with temperature, as seen in seen in Figure 6.5. The heating of PuO_2 will also promote the migration and release of He from the lattice [161].

In Chapter 5 it was found that the presence of Am made a significant impact to the defect chemistry of PuO_2. Therefore, investigation of the behavior of He in PuO_2 is incomplete without consideration the significant ingrowth of Am produced by ^{241}Pu decaying into ^{241}Am with a half-life of 14.4 years. It was found that Am acts as a p-type dopant in PuO_2, accepting electrons and causing the Fermi level to shift towards the valence band. This could impact upon the incorporation method of He in PuO_2. In particular, a lower Fermi level could promote charged oxygen vacancies becoming the incorporation site.

To test this, the impact Am would have in this system is artificially replicated. A controlled concentration of charge, with a charge magnitude of -1, which replicates the accumulation of Am(III) is introduced. This artificial charge is denoted as λ^{1-}. In Chapter 5, Am(III) was found to be accommodated in PuO_2 as substitutions on Pu sites, with a net charge of -1 ($\mathrm{Am}_{\mathrm{Pu}}^{1-}$). The ratio of Am(IV): Am(III) in (Pu,Am)$O_{2\pm x}$ was found to vary with external conditions and total Am concentrations. However, in conditions where Am(IV) is the dominant oxidation state, Am(III) concentrations remain high, and Am(III) is dominant in hypo-stoichiometric PuO_{2-x}, due to reduction of Am(IV) [149, 150, 151]. In Figure 6.6, the impact of increasing the concentration of λ^{1-} on the defect chemistry of PuO_2 is plotted, at a fixed temperature of 1000 K and oxygen partial pressure

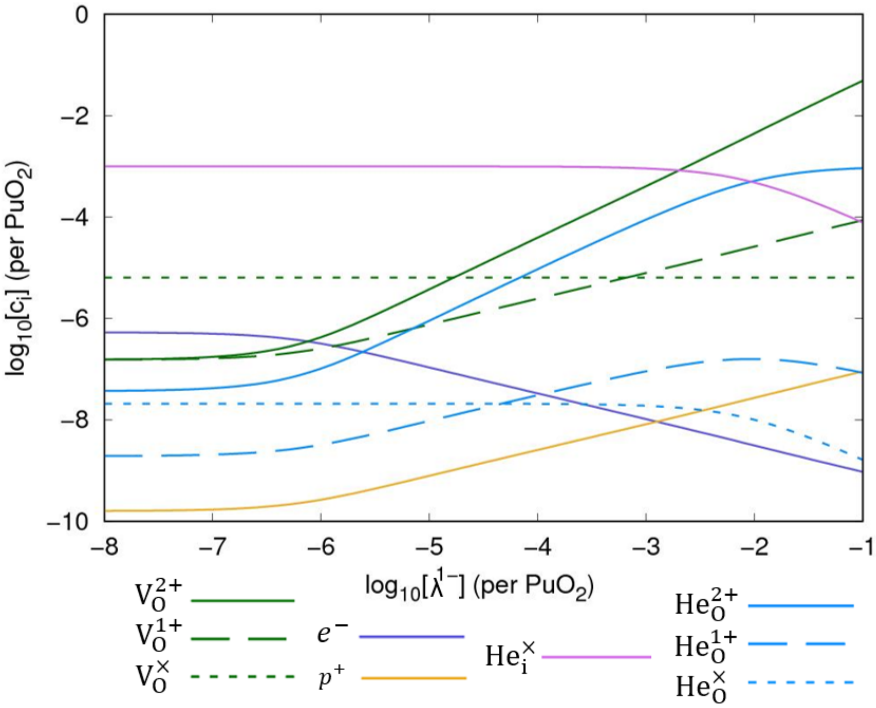

Figure 6.6: The concentration of defects in PuO_2 as a function of the concentration of an artificially added charge (λ^{1-}) at a temperature of 1000 K, oxygen partial pressure of 10^{-30} atm and a fixed He concentration of 0.001 atoms per PuO_2.

of 10^{-30} atm. It can be seen that increasing the concentration of λ^{1-} promotes the accommodation of He on oxygen vacancies and that at a concentration of ≈ 0.01 λ^{1-} per PuO_2, oxygen vacancies overtake the interstitial as the site to accommodate He. Am is, therefore, likely to alter the defect chemistry of He in PuO_2 by promoting the formation of oxygen vacancies that can act as the accommodation site for He.

The final Brouwer diagram, Figure 6.7, aims to predict what this all means for the interim storage of PuO_2. Figure 6.7 models the defect chemistry at 500 K and a fixed concentration of 0.05 λ^{1-} per PuO_2, which simulates $\approx$ 5 % Am(III) in PuO_2. It is now predicted that He is accommodated on oxygen vacancies under conditions of hypo-stoichiometry, with the interstitial site favoured for PuO_2 and PuO_{2+x}.

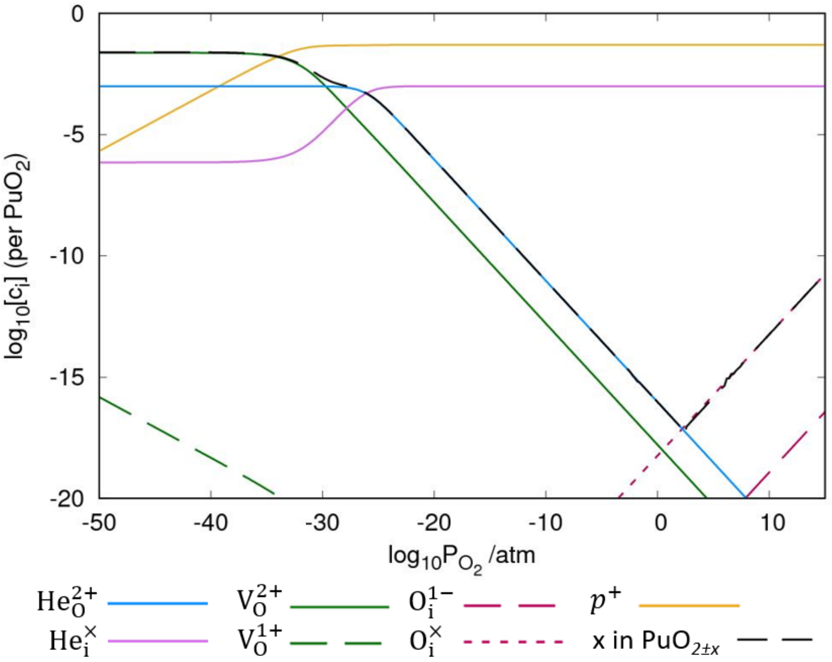

Figure 6.7: Brouwer diagram showing the defect concentrations and value of x in $PuO_{2\pm x}$ as a function of oxygen partial pressure at a temperature of 500 K, and a fixed He concentration of 0.001 atoms per PuO_2. Additionally, a concentration of 5 % Am(III) in PuO_2 is simulated by adding a fixed concentration of 0.05 charges (with a charge magnitude of -1) per PuO_2. To the left and right of the minima of the black line, the diagram records the calculated value of $\log_{10}[x]$ in $PuO_{2\text{-}x}$ and PuO_{2+x}, respectively.

These results can add to the discourse on He migration. The activation barrier for He migration via interstitial sites in PuO_2 will have a different activation barrier to that of migration between oxygen vacancy defect sites. This work has predicted that the accumulation of Am promotes the formation of oxygen vacancies; it would therefore be anticipated that a change in the barrier for He release will occur as the material ages. It cannot be quantified how it will change without calculating the barriers themselves which is left to future work.

6.4 Summary

In summary, it has been shown that the preferred incorporation site for He in PuO_2 is on a plutonium vacancy. However, by considering the availability of such defects it is found using a point defect model constructed for PuO_2 that accommodation of He under equilibrium conditions will be as an interstitial. This remains the preferential site regardless of the concentration of He and for values of x in PuO_{2+x} greater than -0.2. The neutrally charged $\mathrm{He}_{\mathrm{O}}^{\times}$ defect is the favoured oxygen vacancy for He incorporation, but its concentration in PuO_2 is found to be below that of $\mathrm{He}_{\mathrm{i}}^{\times}$ throughout the hypo-stoichiometric region. The impact the decay product Am may have on the method of He incorporation is considered by simulating the presence of its charge in PuO_2. It is predicted that increasing concentrations of Am will promote the accommodation of He on an oxygen vacancy site in hypo-stoichiometric PuO_2.

Chapter 7

Plutonium oxide nanoparticles

7.1 Introduction

So far in this thesis the properties of PuO_2 have been investigated by studying the bulk material. Indeed most computational studies focus their attention on the bulk material, whilst others have studied the material's low-index surfaces; refs. [46] and [77] highlight this effort. Whether these studies are representative of samples of PuO_2 that have a high surface to volume ratio exists as an important, unanswered question. This is very relevant to storage facilities that store PuO_2 as a powder or at nuclear legacy sites where Pu has been found to migrate in subsurface environments in the form of nano-sized PuO_2 colloids [167, 168]. Nanoparticles (NPs), by nature, possess highly under-coordinated cations (relative to the bulk) at the material's facets, edges and corners that could influence the material's properties. In this chapter a theoretical analysis of the properties of PuO_2 NPs is performed: the impact of the NP morphology on the material is analysed, in particular, asking whether the formation of higher oxides (PuO_{2+x}) are linked to this morphology. Using *ab initio* techniques to simulate actinide NPs is computationally demanding and limits the size of NPs that can be studied; here, NPs with up to 245 atoms (equating to a particle diameter of $\backsim$ 2.2 nm) are employed.

The study will complement the existing findings of experiment: PuO_2 NPs have, in recent years, been synthesised and examined using a range of analytical methods. Romanchuk *et al.* [169] and Gerber *et al.* [170] both formed PuO_2 nanoprecipitates by the neutralisation of Pu solutions with Pu in varying oxidation states tested. Both found that, regardless of the synthesis path taken, crystalline NPs with a size of $\backsim$ 2.5 nm formed. Gerber *et al.* [170] used high energy resolution detection (HERFD), as well as complementary methods, to conclusively prove that the NPs were composed of Pu(IV). After producing their NPs, Bonato *et al.* [171] fired them at varying temperatures. The firing temperature was found to effect the nanostructure produced; NPs with a larger diameter were produced at higher temperatures and it was observed that the lattice parameter would decrease as the size of the NP increased. Again, the samples were found to be composed of predominantly Pu(IV). These results have not indicated any presence of PuO_{2+x}, although there is disagreement on the nature of the Pu-O interaction in the first coordination sphere. Whilst some authors [171, 172] report a Pu-O shell splitting, the most recent work by Gerber *et al.* [170] finds that there is only one Pu-O interaction, resulting in a NP structure very similar to bulk PuO_2.

7.2 Methodology

7.2.1 Nanoparticle construction

In order to construct and simulate a PuO_2 NP, the equilibrium shape of the crystal must be known. This can be predicted by performing a Wulff construction, where a crystal is constructed such that the surface energy is minimised. To perform the construction, the surface energies of the low-index surfaces of PuO_2 need to be found and supplied; the low-index {111}, {110} and {100} PuO_2 surfaces are illustrated in Figure 7.1. Past DFT calculations on actinide dioxides [77] and PuO_2 [173, 174, 175] have consistently found that the {111} surface is the most stable, to such an extent that Wulff constructions have predicted a PuO_2 crystal entirely composed of {111} facets [77, 174]. The initial NP structures were therefore constructed from expansions of the $Fm\bar{3}m$ PuO_2 unit cell, cleaved at the O-terminated {111} surface, creating NPs octahedral in shape. Two NPs are constructed using this method: $Pu_{44}O_{80}$ and $Pu_{85}O_{160}$, depicted in Figure 7.2a. These two NPs have a diameter of ∽ 1.6 or ∽ 2.2 nm and contain 33 or 80 fully coordinated bulk O-atoms. NPs with a stoichiometric composition are constructed by removing four or five of the corner Pu atoms in $Pu_{44}O_{80}$ and $Pu_{85}O_{160}$, respectively. These stoichiometric NPs, depicted in Figure 7.2b, now have O-terminated {100} facets at the corners where Pu has been removed. The removal of the remaining corner Pu atoms results in two hyper-stoichiometric NPs, $Pu_{38}O_{80}$ and $Pu_{79}O_{160}$.

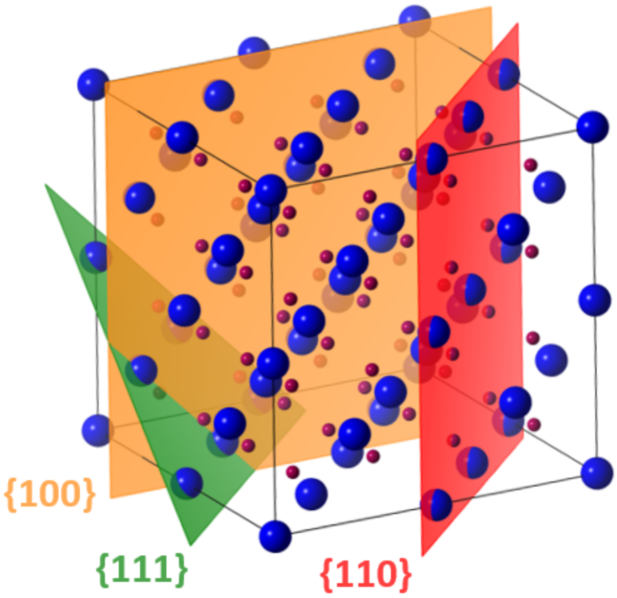

Figure 7.1: The low-index PuO_2 {111}, {110} and {100} surfaces. Plutonium and oxygen atoms are depicted with blue and red spheres, respectively.

The formation energies, E_f, of NPs with differing surface compositions are compared by defining them with respect to the chemical potentials of their two con-

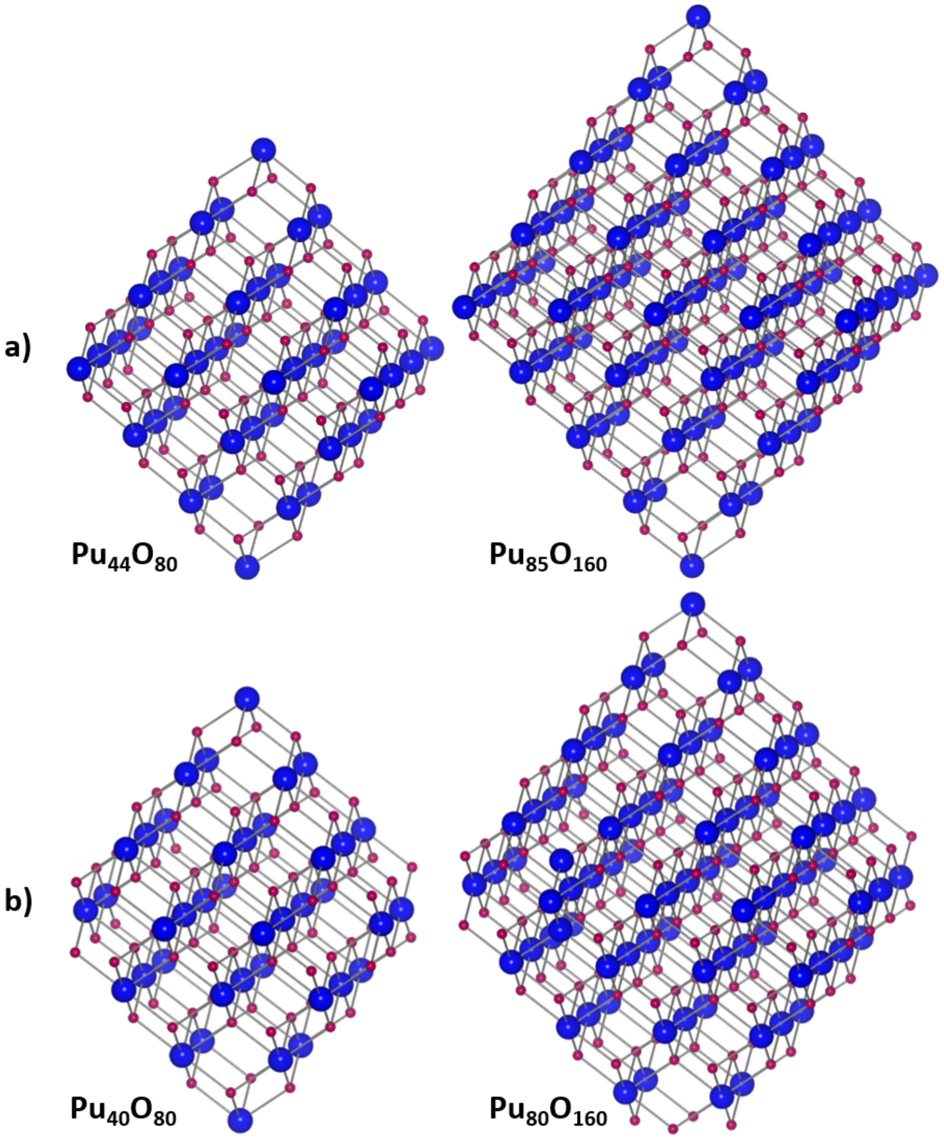

Figure 7.2: Atomic structures of (a) hypo-stoichiometric and (b) stoichiometric PuO_2 NPs. Plutonium and oxygen atoms are depicted with blue and red spheres, respectively.

stituent species, Pu and O_2:

$$E_f = \frac{1}{n} E^{\mathrm{DFT}}_{\mathrm{Pu_nO_m}} - \mu_{\mathrm{Pu_{(s)}}}(P_{\mathrm{O_2}}, T) - \frac{m}{2n}\mu_{\mathrm{O_2}}(P_{\mathrm{O_2}}, T) \tag{7.1}$$

$E^{\mathrm{DFT}}_{\mathrm{Pu_nO_m}}$ is the DFT energy of a plutonium oxide NP with n Pu atoms and m O atoms. $\mu_{\mathrm{Pu}_{(\mathrm{s})}}(P_{\mathrm{O}_2}, T)$ and $\mu_{\mathrm{O}_2}(P_{\mathrm{O}_2}, T)$ are the oxygen partial pressure and the temperature dependent chemical potentials of Pu and O_2, respectively. These two chemical potentials are set according to the chemical potential of PuO_2: defined as the energy of a formula unit of bulk PuO_2, determined using DFT ($\mu^{\mathrm{DFT}}_{\mathrm{PuO}_{2(\mathrm{s})}}$):

$$\mu_{\mathrm{Pu}_{(\mathrm{s})}}(P_{\mathrm{O}_2}, T) + \mu_{\mathrm{O}_2}(P_{\mathrm{O}_2}, T) = \mu^{\mathrm{DFT}}_{\mathrm{PuO}_{2(\mathrm{s})}} \tag{7.2}$$

The chemical potential of O_2 is calculated with the approach of Finnis *et al.* [107]. This method uses the known experimental formation energy of the oxide ($\Delta H_{\mathrm{f}}^{\mathrm{PuO}_2}(P^{\circ}_{\mathrm{O}_2}, T^{\circ})$ = -10.94 eV [143]) and the chemical potential of metallic Pu determined using DFT ($\mu^{\mathrm{DFT}}_{\mathrm{Pu}_{(\mathrm{s})}}$) to obtain the chemical potential of oxygen at standard temperature and pressure, i.e.:

$$\Delta H_{\mathrm{f}}^{\mathrm{PuO}_2}(P^{\circ}_{\mathrm{O}_2}, T^{\circ}) = \mu^{\mathrm{DFT}}_{\mathrm{PuO}_{2(\mathrm{s})}} - \mu^{\mathrm{DFT}}_{\mathrm{Pu}_{(\mathrm{s})}} - \mu_{\mathrm{O}_2}(P^{\circ}_{\mathrm{O}_2}, T^{\circ}) \tag{7.3}$$

The O_2 chemical potential at the desired conditions is extrapolated from $\mu_{\mathrm{O}_2}(P^{\circ}_{\mathrm{O}_2}, T^{\circ})$ using Equation 4.9, where $\Delta\mu(T)$ is determined using the real heat capacities of the O_2 molecule: Equations 3.13 - 3.17.

7.2.2 Computational details

DFT simulations were performed using VASP employing the PAW method implemented with the frozen-core approximation. The plutonium 6*s*, 6*p*, 5*f*, 6*d* and 7*s* and oxygen 1*s*, 2*s* and 2*p* electrons are treated as valence. The cut-off energy for the planewave basis set was 400 eV with reciprocal space summations performed at the Γ-point. The PBEsol + U method is adopted using the approach of Liechtenstein *et al.* [50]. The *U* parameter for the Pu(5*f*) states is varied as part of this investigation, the *J* parameter was fixed at a value of 0.0 eV. The influence of SOI is considered in all simulations, with the magnetic behaviour, including non-collinear configurations, investigated in Section 7.3.1. The energy threshold for electronic convergence is set as 1×10^{-5} eV with structural convergence deemed complete when the forces on all atoms did not exceed 2×10^{-2} eV Å^{-1}. The minimum distance between the periodically repeating NPs is set at 1.5 nm. The electron charge density at each atomic site of the converged DFT simulations was predicted by performing a Bader charge analysis [157].

7.3 Results & discussions

7.3.1 Magnetic configuration

In their study of the magnetic order of bulk PuO_2, Pegg *et al.* showed that DFT predicts a longitudinal 3k anti-ferromagnetic (AFM) ground state, which was then used to study PuO_2 surfaces [48, 77]. Here, using the $Pu_{44}O_{80}$ NP and PBEsol + U (U = 6 eV, as used by Pegg *et al.* [48, 77]), it is investigated whether DFT affirms that this ground state is favourable when PuO_2 is in NP form. The collinear and non-collinear AFM configurations of different domains (longitudinal or transverse) are studied and compared, in addition to the diamagnetic (DM) configuration. Using the central (bulk) atoms of $Pu_{44}O_{80}$, Figure 7.3 illustrates the AFM configurations tested. As illustrated, each Pu atom in the non-collinear configurations is assigned 1 of 4 directions in initial effective magnetic moment. In bulk PuO_2 the periodically repeating unit cell means that there is 1 possible assignment for each domain; however, due to their finite size, the NP possesses 4 unique assignments for each domain, each resulting in a different overall configuration. It was found that these unique assignments must be tested in order to attain the lowest energy state: Figure 7.3 shows the assignment with the calculated lowest energy. Table 7.1 compares the lowest energy magnetic states for each configuration, showing that the longitudinal 3k AFM state is predicted by DFT to continue being the lowest energy configuration for PuO_2 in NP form. The complete set of results is provided in Appendix B. The predicted magnetic moment on the Pu ions is also reported,

Table 7.1: The relative energy (eV per atom) and average magnetic moment (μ_B/Pu ion) for different magnetic configurations assigned to $Pu_{44}O_{80}$, calculated with PBEsol + U (U = 6 eV).

Magnetic configuration		Relative energy	Average magnetic moment			
			Coordination number			
			4	6	7	8
DM		0.232	0.00	4.55	0.00	0.00
Longitudinal	1k	0.015	4.83	4.27	3.81	3.80
	3k	0.000	4.82	4.24	3.81	3.80
Transverse	1k	0.014	4.49	4.32	3.82	3.80
	3k	0.004	4.82	4.19	3.94	3.80

revealing a strong dependence on the Pu atom's coordination number (CN); however, it is thought that DFT could be overestimating these values and that PuO_2 is a small-moment insulator [77]. Figure 7.4 illustrates the direction of the magnetic moment assigned to the 44 Pu atoms in the lowest energy configuration, followed by the subtle change predicted by the DFT calculation. It can be seen that the longitudinal 3k AFM structure is maintained, albeit with some distortion in the direction of the surface Pu atom's magnetic moment. The fully-coordinated Pu atoms experience only very small distortion and effectively behave as bulk, longitudinal 3k AFM PuO_2. With the longitudinal 3k AFM configuration re-affirmed as the favourable configuration, it is applied to all subsequent NPs in this study.

7.3.2 Electronic structure

To mitigate the self-interaction error, present when simulating PuO_2 with conventional DFT, the DFT + U method is adopted. This introduces the independent variable U when J is fixed at 0 eV. The effect of increasing U can be seen clearly in Figure 7.5, where the DOS of $Pu_{40}O_{80}$ is plotted. Increasing the U parameter has two main impacts: it increases the band gap whilst decreasing the Pu($5f$) and

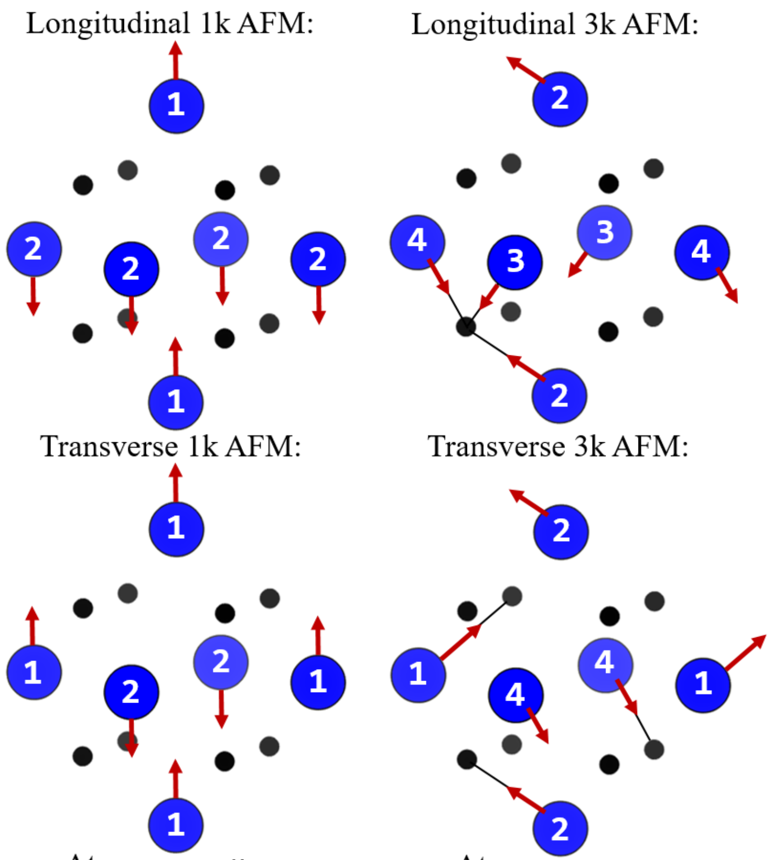

Atom	μ
1	(0, 0, 1)
2	(0, 0, -1)

Atom	μ
1	(1, 1, 1)
2	(-1, -1, 1)
3	(-1, 1, -1)
4	(1, -1, -1)

Figure 7.3: Magnetic structure of $Pu_{44}O_{80}$ nanoparticle's anti-ferromagnetic (AFM) states, depicted using the central, bulk atoms. The direction of the effective magnetic moment (μ) on each plutonium ion is shown by an arrow and the μ = (a,b,c) wave-vector matrix key.

O($2p$) band hybridisation in the valence band. This result for NPs mirrors what is seen in bulk PuO_2 (see Chapter 4); it can be concluded that the main characteristics of the DOS are retained for PuO_2 whether in bulk or NP form. Beyond these main characteristics, the NP-form does impact the DOS: the under-coordinated Pu and O ions, present at the surface of the NPs, result in the appearance of defective

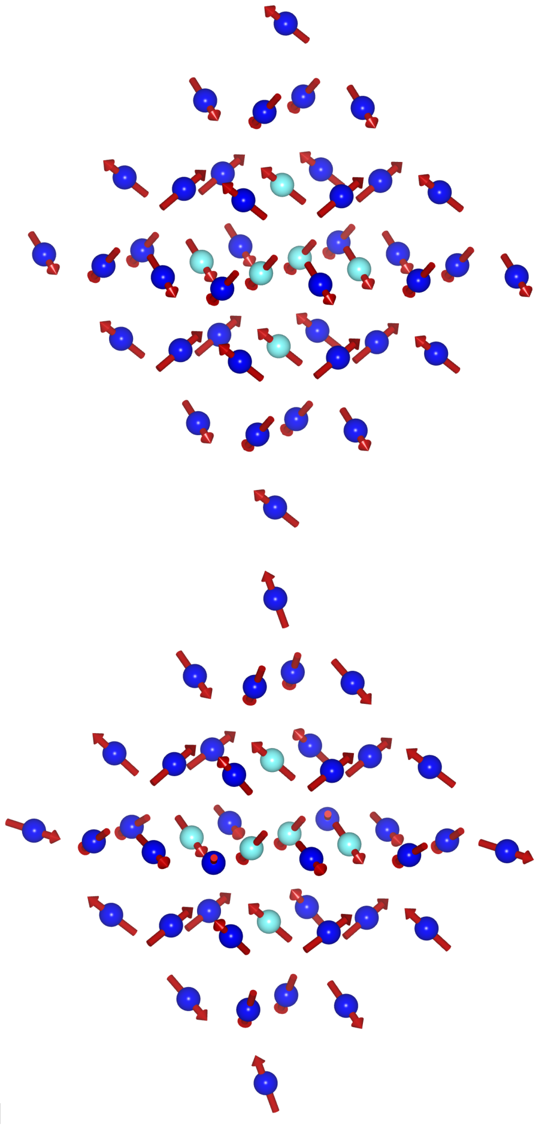

Figure 7.4: The magnetic structure of $Pu_{44}O_{80}$ assigned the longitudinal 3k AFM configuration prior to (top) and following (bottom) DFT calculation with PBEsol + U (U = 6 eV). The arrows indicate the direction of the effective magnetic moment, plutonium surface and bulk atoms are depicted with dark blue and light blue spheres, respectively. Oxygen atoms are not shown.

states. Defective Pu and O sites are found at the conduction and valence bands, respectively. The rest of this study demands a selection of the U parameter. Once again, a U parameter is selected that reproduces the band gap of bulk PuO_2 calculated by hybrid-DFT (the HSE06 functional), as justified in Chapter 4. For bulk PuO_2, this band gap is reproduced in PBEsol + U at a U value of 7 eV, which is

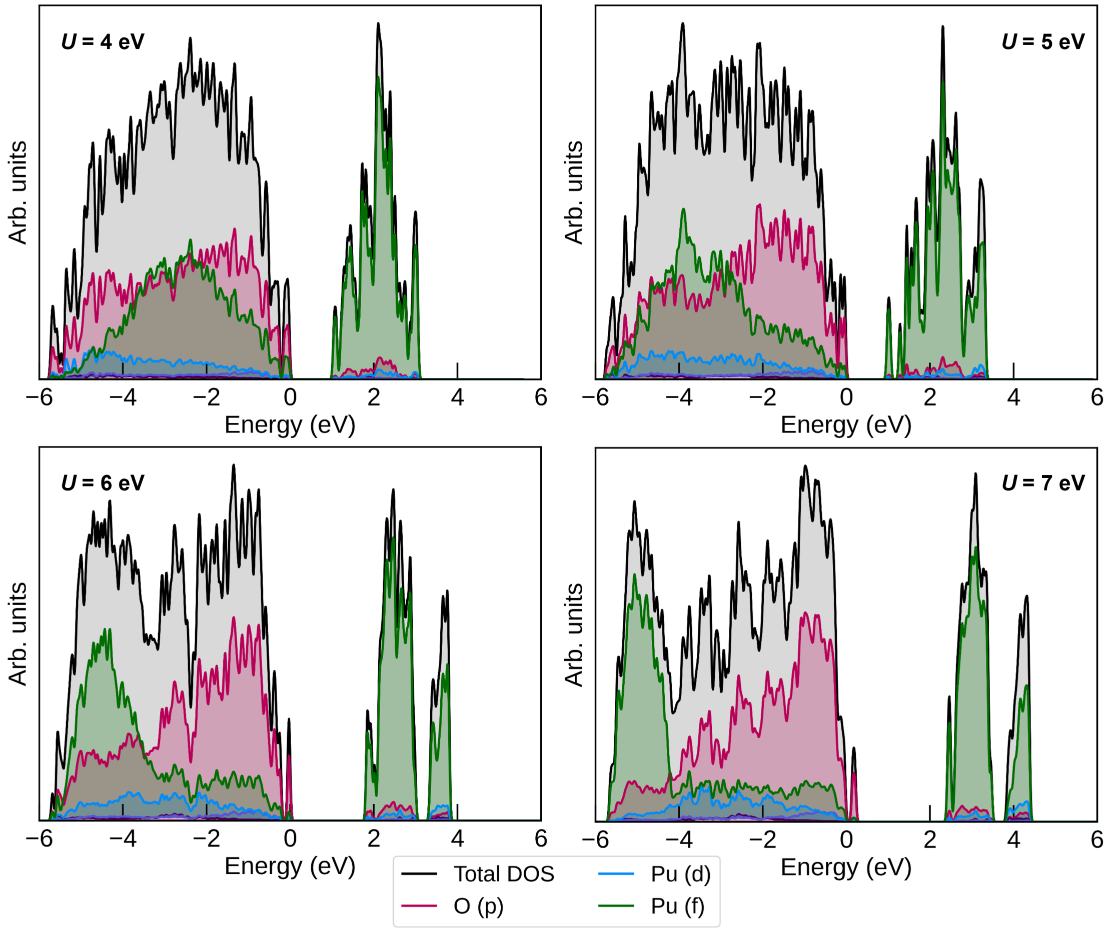

Figure 7.5: The density of states of $Pu_{40}O_{80}$ nanoparticles calculated at varying U values with the PBEsol + U functional.

adopted.

A comparison of the DOS for stoichiometric NPs of different sizes, as well as bulk PuO_2, is shown in Figure 7.6. Using DFT to simulate finite systems makes it challenging to discern the true band gap. Simply measuring the band gap as difference between the highest occupied molecular orbital (HOMO) and the lowest unoccupied molecular orbital (LUMO), ΔE_{H-L}, (see Table 7.2) results in a finding that the band gap of NPs are smaller than the bulk material. Due to quantum confinement effects it would be expected to observe the opposite phenomena: the band gap in NPs being larger than the bulk material. In order to better predict the band gaps in the simulated NPs the work of Selli *et al.* [176] is followed where a method to distinguish between states that are localised and delocalised was employed. The maximum squared coefficient of each eigenstate (Max. Coeff.) is calculated and plotted below each DOS in Figure 7.6. High or low values of Max. Coeff. correspond to localised or delocalised states, respectively; it can be seen that the bulk material consists of delocalised states which are used to set the threshold that must be exceeded for a state to be classified as localised. Applying this methodology results in the prediction of a new value for each NP's band gap: this is named $\Delta E_{delocal}$. The results are recorded in Table 7.2.

Several observations are made from Table 7.2. First, $\Delta E_{delocal}$ is larger than ΔE_{H-L} for each NP, as expected. Next, using $\Delta E_{delocal}$, the quantum confinement effect can be clearly observed for the stoichiometric NPs: for theses two NPs, $\Delta E_{delocal}$ is larger in the smaller NP and both exhibit a $\Delta E_{delocal}$ larger than the bulk. It is also observed that for the three smallest NPs, $Pu_{44}O_{80}$, $Pu_{40}O_{80}$, and $Pu_{38}O_{80}$, $\Delta E_{delocal}$ increases with decreasing size.

Unfortunately, issues remain in the band gap description. For the hypo-stoichiometric NPs, $\Delta E_{delocal}$ decreases with decreasing size, and whilst the hyper-stoichiometric NPs display the correct trend, $\Delta E_{delocal}$ of $Pu_{79}O_{160}$ is below that of the bulk. It is therefore concluded that whilst the employed method of distinguishing between states that are localised and delocalised has improved the description of band gaps in PuO_2 NPs, determining the true band gap of NPs using DFT requires further attention. The DFT study of Puigdollars *et al.* [177] discuss similar issues when investigating the electronic structure of zirconia NPs.

7.3.3 Local structure

Analysis of the relaxed NPs indicates that their local structure varies with both the size of the NPs and their surface structure. The oxidation states of Pu and O are

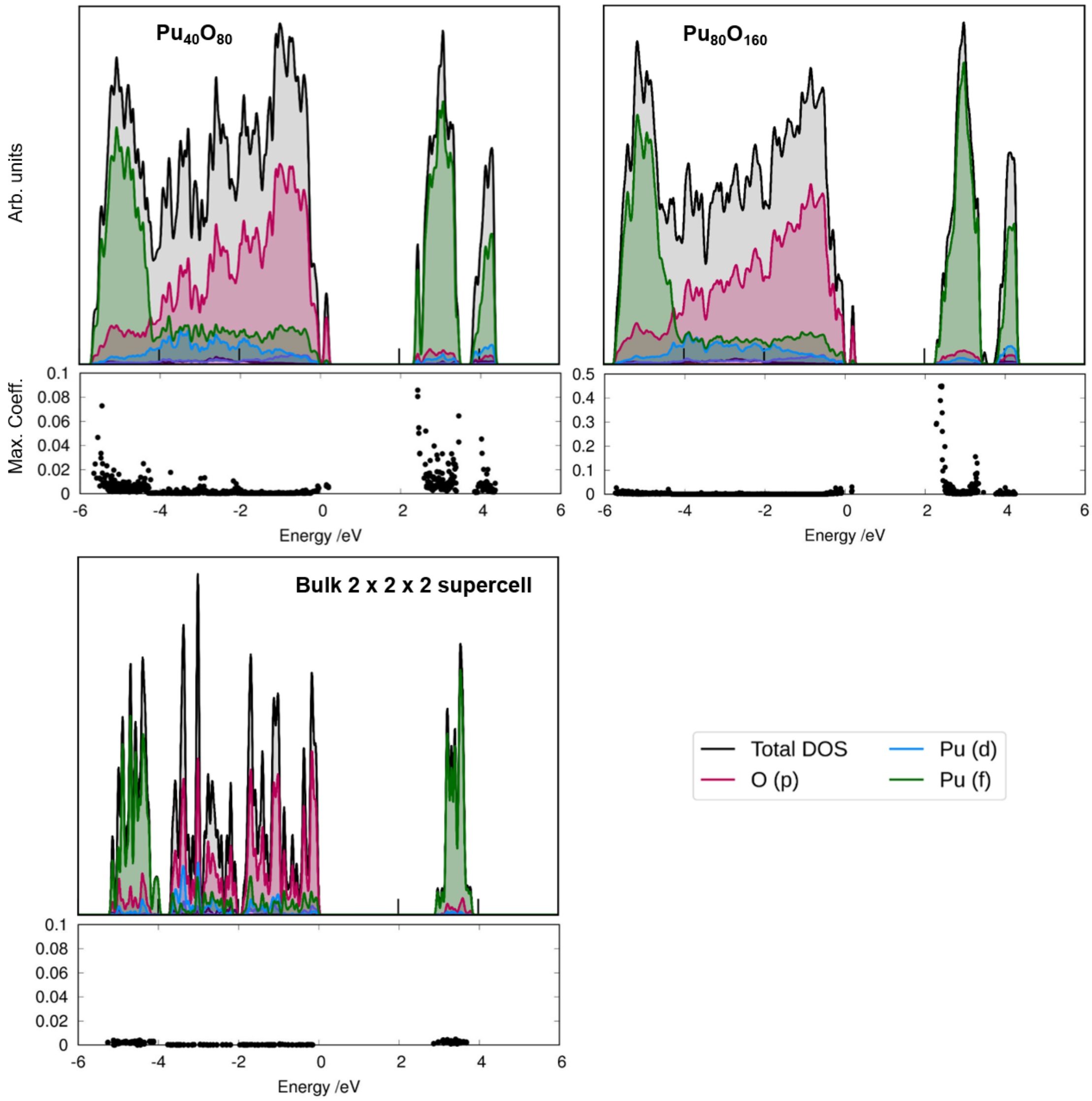

Figure 7.6: The density of states for two differently sized nanoparticles (Pu$_{40}$O$_{80}$, ∽ 1.6 nm and Pu$_{80}$O$_{160}$, ∽ 2.2 nm), compared to the density of states of bulk PuO$_2$. The calculated maximum squared coefficient of each eigenstate accompanies each density of states plot.

seen to be impacted by the surface structure, or stoichiometry, of the NPs. The hypo-stoichiometric NPs (Pu$_{44}$O$_{80}$ & Pu$_{85}$O$_{160}$) include Pu atoms at their corners with a very low CN of 4. Bader charge analysis indicates that all six of these corner atoms are reduced to Pu(III); in addition, a portion of the edge atoms with a CN of 6 are also reduced to Pu(III). The remaining Pu atoms, including all bulk and

Table 7.2: HOMO-LUMO band gap (ΔE_{H-L}), estimated delocalised states band gap ($\Delta E_{delocal}$), and average Pu-Pu distance ($|d_{\mathrm{Pu-Pu}}|$) of PuO_2 nanoparticles of varying size and stoichiometry (S), with comparison to bulk PuO_2. Calculated with PBEsol + U (U = 7 eV).

		ΔE_{H-L} (eV)	$\Delta E_{delocal}$ (eV)	$\|d_{\mathrm{Pu-Pu}}\|$ (Å)
Hypo-S	$Pu_{44}O_{80}$	2.34	2.99	3.73
	$Pu_{85}O_{160}$	1.85	3.07	3.75
Perfect-S	$Pu_{40}O_{80}$	2.26	3.95	3.73
	$Pu_{80}O_{160}$	2.10	3.20	3.76
Hyper-S	$Pu_{38}O_{80}$	2.30	4.09	3.74
	$Pu_{79}O_{160}$	2.18	2.78	3.76
Bulk PuO_2		3.03	3.03	3.83
Experiment		1.8 [56], 2.8 [57], 3.92 [58], 4.1 [59]		

facet atoms, remain Pu(IV). In the hyper-stoichiometric NPs ($Pu_{38}O_{80}$ & $Pu_{79}O_{160}$) containing excess O, only the Pu(IV) oxidation state is seen. Rather than oxidation of Pu, the response in these NPs appears to be a significant loss in charge density, although not enough to be fully oxidised to O^{1-}. The contrast between reduced ionicity and changes in formal oxidation states is discussed by Walsh *et al.* [178]. These anions are exclusively located at the $\{100\}$ facets as shown in Fig. 7.7. As described by Huang and Beck [179], an under-coordinated surface O atom with unfilled p orbitals is highly reactive. One reaction path would be the formation of O_x^q groups ($-2 \leq q \leq 0, x \leq 3$) on the NP surface due to the reaction of O^- with other O atoms.

To discuss the Pu-O interaction in the first coordination sphere, the Pu-O distance is first categorised as either short (2.17-2.23 Å), or medium (2.23-2.50 Å). These boundaries encompass all the Pu-O distances in the relaxed NP's first coordination sphere; for reference, the Pu-O distance in bulk PuO_2 is 2.34 Å. A clear pattern is observed in the relaxed NPs: short Pu-O bonds are observed at edge Pu atoms (CN=6) that have not been reduced to Pu(III), as well as corner Pu atoms (CN=4).

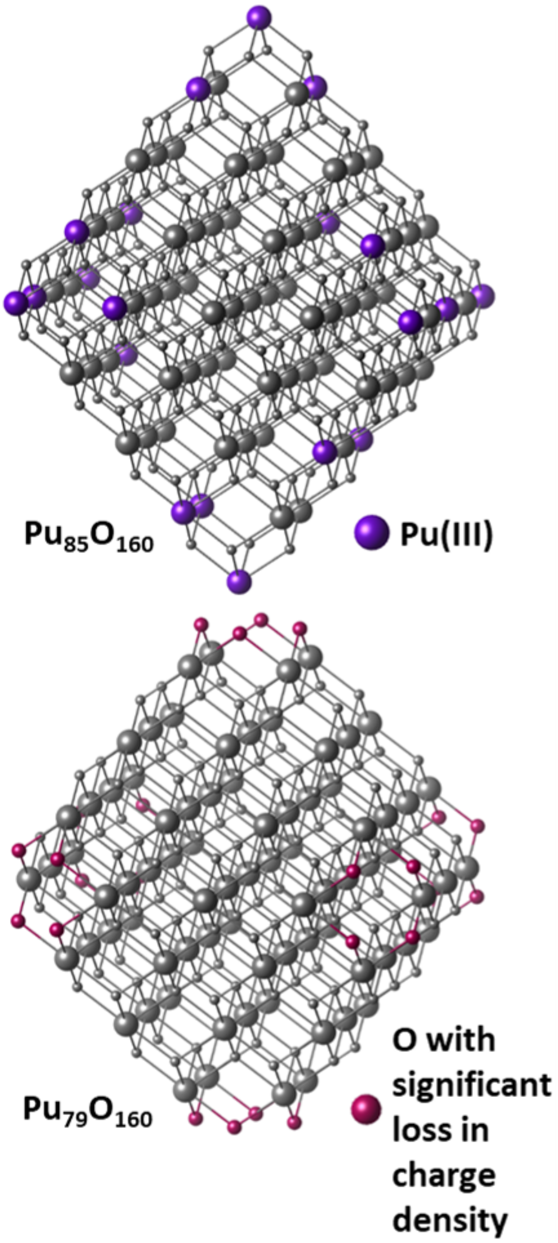

Figure 7.7: Illustration of the predicted oxidation states of Pu and O atoms in simulated PuO_2 NPs. Atoms not predicted to be oxidised or reduced (i.e. Pu(IV)/ O^{2-}) are coloured grey.

Aside from this, the remaining Pu-O bonds are classified as medium. This includes all bulk (CN=8), facet (CN=7), and edge Pu(III) (CN=6) atoms.

The average Pu-Pu distance for each relaxed NP (reported in Table 7.2), indicates that PuO_2 NP's lattice parameters contract with decreasing NP size. The results of Bonato *et al.* [171] and Dalodière *et al.* [180] contrast, reporting either a slightly increasing or slightly decreasing lattice parameter, respectively, as their PuO_2 nanocrystals/colloids decreased in size. Lattice expansion with decreasing NP size has previously been observed in some oxides, e.g. CeO_2 [181], and has been attributed to electrostatic effects induced by the decreasing NP size [182]. The opposite has been seen in ZrO_2 where experiment [183], as well as DFT [177], indicate contraction with decreasing NP size. Monticone *et al.* [184] suggest there is no general rule to describe lattice constant changes in small crystalline clusters. Here, the DFT prediction that PuO_2 retains bulk-character when in NP form, in particular, a dominance of the Pu(IV) oxidation state, can help describe the observed absence of PuO_2 lattice constant expansion with decreasing NP size: the under-coordinated Pu(IV) atoms at the NP surface exhibit a stronger Pu-O electrostatic attraction than their fully coordinated counterparts. This results in the shortening of these Pu-O bonds. This impacts upon the remaining Pu-O bonds in the particle, a particle size effect, where, on average, these remaining Pu-O bonds are also reduced in magnitude with respect to the bulk. This effect is increased with an increased surface-to-volume ratio, i.e. decreasing particle size.

An accurate description of the Pu-O interaction in the first coordination sphere has provoked much discussion and contrasting theories. Gerber *et al.* [170] report a single interaction, whilst others report distortion. The proposed cause of this distortion has differed, with short Pu-O bonds previously attributed to hydroxyl groups [33, 185], the formation of Pu(V)/Pu(VI) [33], or surface effects correlated to reduction in the size of the NP, with the surface μ^3-O bonds an important factor [171, 172, 180]. The DFT results presented here would best support the latter explanation; short Pu-O bonds (2.17-2.23 Å) have been predicted in the absence of hydrogen and without oxidation of Pu. DFT predicts that these short Pu-O bonds are located at edge/corner Pu atoms and are not exclusive to μ^3-O atoms: short bonds to μ^4-O atoms in the second layer are also predicted.

7.3.4 Probing the favourable surface configuration

Analysis of the local structure of the relaxed NPs in Section 7.3.3 has indicated a variable surface chemistry, with Pu(III) and oxidised oxygen ions predicted to be found in hypo- and hyper-stoichiometric PuO_2 NPs, respectively. Here, the environmental conditions that may promote or favour a particular surface configuration are investigated. Using the thermodynamic relationships introduced in the methodology (Section 7.2.1), a phase diagram is created, predicting the favoured surface structure, or stoichiometry, as a function of O_2 partial pressure and temperature for the PuO_2 NPs with a diameter of $\backsim 2.2$ nm (Figure 7.8). Strong similarities are observed between this calculated phase diagram and the phase diagram predicted by Moxon *et al.* [173] for the reduction of PuO_2 surfaces. According to the phase diagram, under an O_2 partial pressure of 10^{-10} atm the hypo-stoichiometric NP becomes more favourable than the stoichiometric NP at $\backsim$ 450 K. At the same O_2 partial pressure, Moxon *et al.* [173] predict reduction of the {100} surface via oxygen vacancy formation at $\backsim$ 475 K. Reduction in the NPs is regulated by the corner termini, where hypo-stoichiometric {111} corner termini are produced when the oxidised anions at the {100} surfaces are reduced to O^{2-} (see Figure 7.7). Therefore despite different reduction processes, the environmental conditions that reduction of the {100} surface is predicted to be thermodynamically favourable are in close agreement.

The phase diagram implies that high temperatures favour a reduced NP surface: PuO_2 subject to calcination/ thermal stabilisation would therefore be expected to form such surfaces. Meanwhile, atmospheric or storage conditions (dependent on the amount of O_2 present) favour an oxidised surface. This is a significant result implying a PuO_{2+x} surface is thermodynamically favoured under conditions that PuO_2 could reasonably be exposed to. Crucially, it is the small NP size, specifically the chemistry at the corner termini, that is responsible for a PuO_{2+x} surface to be favoured under some conditions. A mechanism that could exist to avoid a

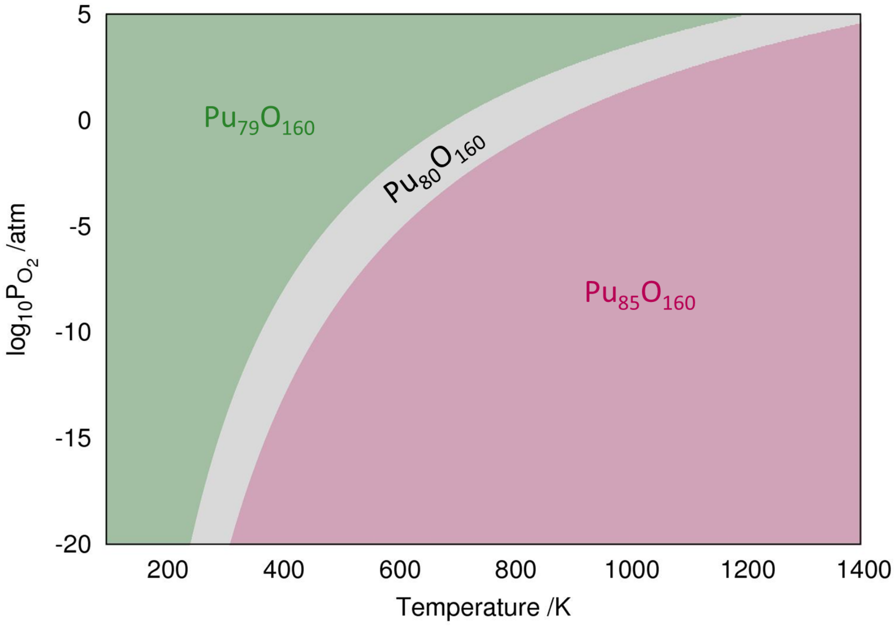

Figure 7.8: Phase diagram calculated for plutonium oxide nanoparticles at a size of ∽ 2.2 nm. The grey region denotes the stoichiometric surface, the red region denotes an oxygen-deficient surface, and the green region signifies a oxygen-excess surface.

net-oxidised NP would be the formation of oxygen vacancies in the bulk; however, under the conditions that Figure 7.8 predict a PuO_{2+x} surface to be favourable, Chapter 4 has shown that oxygen vacancies are not present in the bulk material. As discussed earlier, these oxidised surfaces are predicted by this DFT study to have oxygen ions with reduced charge denisties located at {100} facets. These reactive ions are likely to react with, or adsorb, atmospheric molecular species and organic molecules, depending upon the process environment. This could explain the preferential adsorption of O_2 gas from the head space of interim storage canisters onto PuO_2 surfaces.

7.4 Summary

In this chapter PuO_2 NPs varying in size between 1.6 and 2.2 nm have been studied using the PBEsol + U functional within DFT. It is found that the NPs largely resemble bulk PuO_2: they are predominantly composed of the Pu(IV) oxidation state and are predicted to retain the same magnetic ground state and many of the DOS characteristics. However, alternations in the chemistry are observed, a consequence of the under-coordinated atoms, present at the NP's facets, edges, and corners. Most notably a variation in the oxidation state of a small number of surface Pu and O atoms is seen, with a predicted dependence on environmental conditions. The results are in agreement with previous work ruling out PuO_{2+x} NPs on the basis of no Pu(V)/Pu(VI) being present, but instead detect a new mechanism: reduction of charge density of oxygen ions on the surface. This study implies that the surface chemistry of PuO_2 NPs is influenced by their synthesis conditions and the conditions they then reside, helping advance the understanding of PuO_2 in both storage and contaminated sites.

Chapter 8

Conclusions and further work

8.1 Defect chemistry

This thesis has presented the results of a comprehensive investigation of plutonium dioxide's defect chemistry. Using a well-considered DFT model coupled to our post-processing tool DefAP, the material's intrinsic defects and important extrinsic defects, the radiogenic impurities Am and He, have been studied.

In Chapter 4 the foundations for the investigation of the defect chemistry were laid by tuning the DFT methodology and building the defect formalism, as appropriate for PuO_2. The results in this chapter conformed to the expectation that oxygen-type defects are responsible for x deviating in $PuO_{2\pm x}$ — that is, oxygen vacancies accommodate PuO_{2-x} and oxygen interstitials accommodate PuO_{2+x}. However, whilst it was found that oxygen interstitials accommodate PuO_{2+x}, the value of x in PuO_{2+x} was not predicted to be anything more than negligible in the bulk, impurity-free material. In the modelling, PuO_2 was simulated in a very oxidising environment, but invariably there is a reluctance for PuO_2 to oxidise. This result strengthens the validity of the model as experiment has also shown PuO_2 is resistant to oxidation by high pressure oxygen, and other oxidants such as ozone and nitrogen dioxide [186]. Korzhavyi *et al.* [32] have also previously reported that reaction of PuO_2 with oxygen to form PuO_{2+x} is endothermic.

Hypo-stoichiometric PuO_{2-x} is, in contrast, much more favourable — the Pu-O phase diagram describes the existence of these phases. The modelling agrees that PuO_{2-x} is thermodynamically favourable under reducing conditions, with x in PuO_{2-x} being accommodated at both low and relatively high magnitudes by the neutrally charged oxygen vacancy. The accommodation mechanism is in disagreement with multiple experimental measurements (highlighted by Ref. [124]) that have indicated that charged oxygen vacancies are responsible. The work in subsequent chapters investigating the impact of Am has provided a feasible explanation.

The impact of radiogenic Am on the defect chemistry, studied in Chapter 5, is significant. Radiogenic Am occupies Pu sites in $(Pu,Am)O_{2\pm x}$ with an evolving ratio of the +III and +IV oxidation states, dependent upon temperature, oxygen partial pressure, and the concentration of the Am itself. The presence of Am(III) is the pivotal factor that alters the defect chemistry relative to impurity-free PuO_2. Am(III) occupies a formally charged Pu vacancy with the net result being the charged Am_{Pu}^{1-} extrinsic defect; the charge of this defect necessitates adjustment in the electronic chemistry. The response is predicted to be a drop in the Fermi level which results in the concentration of holes in the material rising by orders of magnitude compared to Am-free PuO_2: a p-type dopant behaviour. The p-type dopant response has a significant impact on the material's intrinsic defect chemistry. This can be understood by studying Figure 4.7 where it is shown that only a small fall in the Fermi level from the midpoint will result in a change in both the charge state, and elevated concentrations, of the oxygen vacancy in PuO_{2-x}. This provides a likely explanation for the inability in Chapter 4 to observe the charged oxygen vacancies in PuO_{2-x} that is reported in experiment: it is the presence of Am that is responsible for their presence. All experimental measurements of "pure" PuO_2 will contain quantities of Am and our modelling has predicted that this effect is present even when the quantity of Am in PuO_2 is very low. This results in one of the major conclusions of this thesis: analysis of the defect chemistry, and properties of PuO_2 such as the oxygen potential, must consider the impact of the radiogenic Am.

The model was found to very accurately predict the value of x in $(Pu_{1\text{-}y}Am_y)O_{2\text{-}x}$, agreeing very favourably with past experimental results (see Figure 5.4). This indicates that the model is successful and can be used to predict properties of the material that the defect chemistry contributes to: the electrical conductivity, oxygen potential, oxygen diffusion, heat capacity, and thermal conductivity are some examples. In Chapter 5 equations were constructed based on our findings that describe the evolving dependence of x in $(Pu_{1\text{-}y}Am_y)O_{2\text{-}x}$: the proportional relationships to the oxygen partial pressure and the concentration of Am are described.

In Chapter 6 another, albeit very different, radiogenic impurity was studied: He. To study this light element, the methodology was revised to account for van der Waals dispersion interactions. Unsurprisingly, as a noble gas with a small atomic radii, He was preferentially accommodated in $PuO_{2\pm x}$ on the interstitial site. The conclusions of Chapter 5, that Am significantly impacts the defect chemistry, prompted an analysis of the impact of Am on the accommodation of He. The reducing environment promoted by Am results in an inclination for He to be accommodated on oxygen vacancies in $(Pu_{1\text{-}y}Am_y)O_{2\text{-}x}$. Future work will use these findings to empirically model the migration of He in PuO_2 enabling prediction of the material's capability to retain radiogenic He.

Altogether, these results provide new insight into the aging behavior of PuO_2 and thus have implications for the interim storage of the material. Critically, once the modelling considered Am, it was able to reproduce the available experimental values; this lends confidence in the ability of these results to inform future disposition programmes. Industry itself best describes the benefits of the work: the research will "minimise and focus future experimental work on plutonium evolution, which will reduce the risk to operators and researchers, cost and time" (Sellafield Ltd, 2021 [39]). With an improved scientific understanding — that this work can contribute to — some of the pessimistic assumptions built into the safety cases regulating the methods and procedures of PuO_2 storage can be reduced. This can provide an array of benefits such as extending the lifetime of the storage packages or reducing, with confidence, the extent of redundancy built into the package design.

As the DFT-DefAP methodology developed in this thesis to study defects in bulk $PuO_{2\pm x}$ is concluded to be successful at repeating experimental observations, confidence is provided in the model's predictive capabilities. Further work is underway to use the model to study the interaction of additional extrinsic species with PuO_2 during storage. Two of these extrinsic species are nitrogen and chlorine. N_2 will be present in significant quantities in any storage canister sealed in an air atmosphere; Cl_2 is present in a selection of canisters where the decomposition of polymeric material within the cans has been observed (as discussed in Chapter 2). The DefAP methodology introduced in this thesis enables the study of a material's defect chemistry as a function of the partial pressure of a volatile element present in the host material, i.e. O_2 in PuO_2. An updated methodology will enable the impact of the partial pressure of an extrinsic volatile element to be studied. This is important as unlike Am and He, which are radiogenic products, interaction of N and Cl with PuO_2 occurs via exposure to external N_2 and Cl_2.

8.2 Nanoparticles

In a change of direction, the penultimate chapter of this thesis studied PuO_2 in nanoparticle form aiming to better understand the powder form that PuO_2 widely exists in. When investigating the magnetic, local, and electronic structure of the DFT-simulated particles, bulk-PuO_2 characteristics were observed in the immediate vicinity of the particle's surface; meanwhile the under-coordinated atoms located at the surface were observed to possess more unique characteristics.

Most notably, the Pu-O stoichiometry at the surface of the particles, which varies due to the NP morphology, has been predicted to impact the surface chemistry of the NPs. Particles with hypo-stoichiometric surfaces were found to respond by reducing a select number of Pu ions to Pu(III). A hyper-stoichiometric surface was predicted to be accommodated by oxidising oxygen anions, another demonstration of the reluctance of Pu to oxidise to Pu(V) in PuO_2. Using thermodynamic relationships, the environmental conditions where these differing surface configurations become favourable were tested, predicting that each configuration could reasonably be attained (by becoming thermodynamically favourable) in the conditions PuO_2 is exposed to in its lifetime.

This study also provides potential insight into the behavior of PuO_2 in storage. As a hyper-stoichiometric PuO_2 surface was shown to be thermodynamically favourable at conditions experienced in storage, it could explain the preferential adsorption of O_2 gas from the head space of interim storage canisters onto PuO_2 surfaces.

Future work should extend the search for favourable surface configurations. In Chapter 7 two stoichiometric NPs were studied that differed by size, $Pu_{40}O_{80}$ and $Pu_{80}O_{160}$. For each size, hyper-stoichiometric ($Pu_{38}O_{80}$ and $Pu_{79}O_{160}$) and hypo-stoichiometric ($Pu_{44}O_{80}$ and $Pu_{85}O_{160}$) NPs were also built and studied. A more comprehensive investigation of NP stability versus O concentration at the facets, edges, and corners could build upon the conclusions of this thesis. In particular, a deeper study of PuO_{2+x} surfaces should add an additional oxygen layer to the NP to create a super-saturated oxygen surface. This could be a stable configuration when considering the existence of oxidised oxygen anions, predicted in this thesis in hyper-stoichiometric NPs, that would be stabilised by forming O_2 molecular groups.

The interactions between water and PuO_2 surfaces has been intensively studied to further the understanding of the observed gas generation in a number of storage canisters (discussed in Chapter 2). Computational studies have yet to consider the role the NP-morphology may have: in this thesis it has been seen that the under-coordinated edge and corner atoms introduce their own behavior. Future work would benefit in taking this into consideration.

This thesis has extensively discussed the significant impact that radiogenic Am has on the defect chemistry of PuO_2. The future work studying PuO_2 NPs must consider this finding, and will introduce Am-extrinsic defects into the constructed NPs.

8.3 DefAP

The Defect Analysis Package, introduced in Chapter 3, has been built to combine the output of DFT calculations with thermodynamic relationships in order to explore the defect chemistry of PuO_2. As emphasised in the chapter using the examples Si, $YBa_2Cu_3O_7$, and Li_2TiO_3, DefAP has been softcoded, that is, the package obtains its input parameters from user-created input files, allowing the defect chemistry of any crystalline material to be studied.

Future work is underway to update and enhance DefAP's methodologies and capabilities. Section 3.2.3 detailed the option available in DefAP to implement a vibrational entropy contribution to the DFT-calculated internal energies of constituent compounds. This option was used throughout this thesis; for PuO_2 the modification can be summarised as: $\mu_{\mathrm{PuO}_{2(\mathrm{s})}}(T) = \mu^{\mathrm{DFT}}_{\mathrm{PuO}_{2(\mathrm{s})}} - TS_{\mathrm{PuO}_{2(\mathrm{s})}}(T)$. The vibrational entropy of PuO_2 at temperature T, $S_{\mathrm{PuO}_{2(\mathrm{s})}}(T)$ was calculated using empirical potentials.

As an alternative, future work will look at the impact of calculating the temperature-dependent energies (i.e. the Gibbs free energy) of the constituent compounds directly. This could improve the methodology implemented in this thesis as it will not rely on the combination of different computation techniques (e.g. DFT and empirical methods). Calculation of the Gibbs free energy of a compound is made possible by DFPT packages such as Phonopy.

In Section 3.2.1 the concept of competing phases was introduced, i.e. under certain conditions it could become thermodynamically favourable for a host compound to decompose to a secondary phase, or phases. DefAP offers the capability to predict the stability of the system with respect to any number of compounds under the range of conditions investigated. This was used to study the thermodynamic stability of PuO_2 with respect to AmO_2 and Am_2O_3 in Chapter 5. Conditions were found where these two phases were stable with respect to PuO_2, but as the discussion concluded, the conditions this occurred at were not favourable to overcome the kinetic barriers needed to decompose.

In many materials, conditions will be favourable for secondary phase formation. For example, this is prominently observed in uranium dioxide nuclear fuel where some fission product species precipitate as components of a separate oxide phase known as the grey-phase (e.g. Ba, Sr and Zr). Predicting the conditions when a secondary phase becomes stable and studying the resulting point defect equilibria between the separated phases would offer beneficial insight into material behavior and will be a challenging future endeavor.

The concept of this future work is illustrated in Figure 8.1. Here, the defect chemistry of a host material is studied as a function of time. This would necessitate an understanding of how the environmental conditions and impurities vary with time. At some point in time, t, DefAP predicts that a secondary phase has become stable with respect to the host. This secondary phase is now removed from the host material: the quantity removed is determined such that the host returns to stability. The removed secondary phase now possesses its own defect chemistry which is studied *in situ* to the defect chemistry of the host material. As shown in Figure 8.1 it should also be possible to investigate the phase that additional

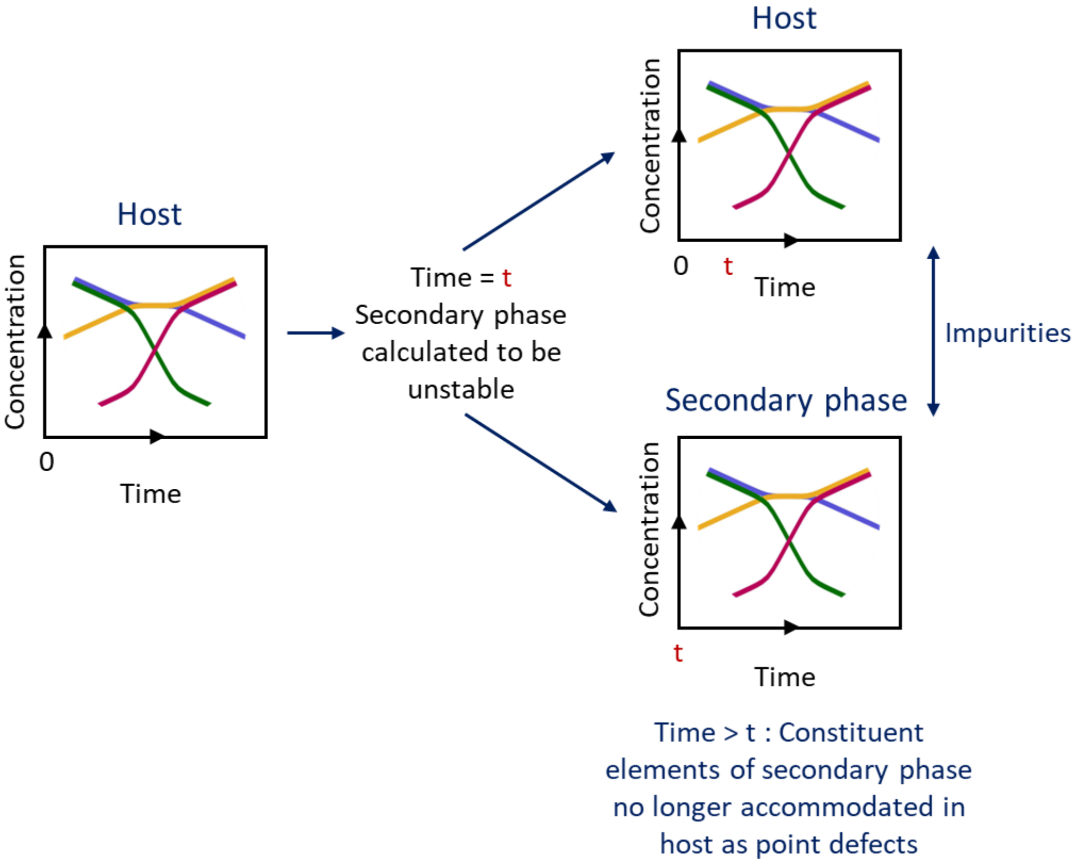

Figure 8.1: Conceptualisation of method to study the defect chemistry of competing phases in a host material.

impurities are favoured thermodynamically to be accommodated in.

Bibliography

[1] Z. Lovasic, "Nuclear management of spent fuel from power reactors," in *Nuclear fuel cycle science and engineering* (I. Crossland, ed.), pp. 427–458, Woodhead Publishing, 2012.

[2] J. W. Dawson and M. Phillips, "Gas-cooled nuclear reactor designs, operation and fuel cycle," in *Nuclear fuel cycle science and engineering* (I. Crossland, ed.), pp. 300–332, Woodhead Publishing, 2012.

[3] "Progress on Plutonium Consolidation, Storage and Disposition," tech. rep., Nuclear Decommissioning Authority, 2019.

[4] W. Walker and M. Lonnroth, *Nuclear Power Struggles: Industrial Competition and Proliferation Control*. London: Allen & Unwin, 1983.

[5] W. Walker, *Nuclear Entrapment: THORP and the politics of commitment*. Institute for Public Policy Research, 1999.

[6] T. Cochran, H. Feiveson, W. Patterson, G. Pshakin, M. Ramana, M.V. Schneider, T. Suzuki, and F. von Hippel, "Fast Breeder Reactor Programs: History and Status, Report 8 in the International Panel on Fissile Material (IPFM)," tech. rep., Princeton University, Princeton, NJ, USA, 2010.

[7] "Office of Nuclear Regulation, 2014. Annual Civil Plutonium and Uranium Figures as of 31 December 2014."

[8] N. C. Hyatt, "Plutonium management policy in the United Kingdom: The need for a dual track strategy," *Energy Policy*, vol. 101, pp. 303–309, 2017.

[9] A. J. Kuperman, "Challenges of plutonium fuel fabrication: explaining the decline of spent fuel recycling," *International Journal of Nuclear Governance, Economy and Ecology*, vol. 4, pp. 302–316, 2019.

[10] N. C. Hyatt, "Safe management of the UK separated plutonium inventory: a challenge of materials degradation," *npj Materials Degradation*, vol. 4, p. 28, 2020.

[11] R. C. O'Brien, R. M. Ambrosi, N. P. Bannister, S. D. Howe, and H. V. Atkinson, "Safe radioisotope thermoelectric generators and heat sources for space applications," *Journal of Nuclear Materials*, vol. 377, pp. 506–521, 2008.

[12] T. Folger, "Record-Breaking Voyager Spacecraft Begin to Power Down," *Scientific American*, 2022.

[13] S. S. Hecker and J. C. Martz, "Aging of Plutonium and Its Alloys," *Los Alamos Science*, vol. 26, pp. 238–243, 2000.

[14] P. Hohenberg and W. Kohn, "Inhomogeneous Electron Gas," *Physical Review*, vol. 136, pp. B864–B871, 1964.

[15] D. S. Sholl and J. A. Steckel, *Density Functional Theory: A Practical Introduction*. John Wiley Sons, Inc, 2009.

[16] A. M. Boring and J. L. Smith, "Plutonium Condensed-Matter Physics," *Los Alamos Science*, vol. 26, pp. 91–127, 2000.

[17] "NDA Plutonium Options," tech. rep., Nuclear Decommissioning Authority, 2008.

[18] M. Janoschek, P. Das, B. Chakrabarti, D. L. Abernathy, M. D. Lumsden, J. M. Lawrence, J. D. Thompson, G. H. Lander, J. N. Mitchell, S. Richmond, M. Ramos, F. Trouw, J.-X. Zhu, K. Haule, G. Kotliar, and E. D. Bauer, "The valence-fluctuating ground state of plutonium," *Science Advances*, vol. 1, no. 6, p. e1500188, 2015.

[19] R. C. Albers, "An expanding view of plutonium," *Nature*, vol. 410, no. 6830, pp. 759–761, 2001.

[20] C. J. Windorff, G. P. Chen, J. N. Cross, W. J. Evans, F. Furche, A. J. Gaunt, M. T. Janicke, S. A. Kozimor, and B. L. Scott, "Identification of the Formal +2 Oxidation State of Plutonium: Synthesis and Characterization of $\{\mathrm{Pu}^{\mathrm{II}}[\mathrm{C}_5\mathrm{H}_3(\mathrm{SiMe}_3)_2]_3\}^-$," *Journal of the American Chemical Society*, vol. 139, no. 11, pp. 3970–3973, 2017.

[21] P. Söderlind, F. Zhou, A. Landa, and J. E. Klepeis, "Phonon and magnetic structure in δ-plutonium from density-functional theory," *Scientific Reports*, vol. 5, no. 1, p. 15958, 2015.

[22] D. Young, *Phase Diagrams of the Elements.* Univ. of California Press, Berkeley, 1991.

[23] H. A. Wriedt, "The O-Pu (Oxygen-Plutonium) system," *Bulletin of Alloy Phase Diagrams*, vol. 11, no. 2, pp. 184–202, 1990.

[24] B. J. Lewis, "Prediction of the oxygen potential in the fuel-to-clad gap of defective fuel rods during severe accident conditions," *Journal of Nuclear Materials*, vol. 270, no. 1, pp. 221–232, 1999.

[25] L. M. Atlas and G. J. Schlehman, *Defect Equilibria of* PuO_{2-x}*, 1100 to 1600°C*. International Atomic Energy Agency (IAEA), 1966.

[26] G. C. Swanson, “Oxygen Potential of Uranium-Plutonium Oxide as Determined by Controlled-Atmosphere Thermogravimetry,” Tech. Rep. LA-6083-T, Hanford Engineering Development Laboratory, Richland, WA, 1975.

[27] R. E. Woodley, “Oxygen potentials of plutonia and urania-plutonia solid solutions,” *Journal of Nuclear Materials*, vol. 96, no. 1, pp. 5–14, 1981.

[28] A. Komeno, M. Kato, S. Hirooka, and T. Sunaoshi, “Oxygen potentials of PuO_{2-x},” *MRS Online Proceedings Library*, vol. 1444, no. 1, pp. 85–89, 2012.

[29] J. M. Haschke, T. H. Allen, and L. A. Morales, “Reaction of Plutonium Dioxide with Water: Formation and Properties of PuO_{2+x},” *Science*, vol. 287, pp. 285–287, 2000.

[30] L. Petit, A. Svane, Z. Szotek, and W. M. Temmerman, “First-Principles Calculations of $PuO_{2\pm x}$,” *Science*, vol. 301, no. 5632, pp. 498–501, 2003.

[31] I. D. Prodan, G. E. Scuseria, J. A. Sordo, K. N. Kudin, and R. L. Martin, “Lattice defects and magnetic ordering in plutonium oxides: A hybrid density-functional-theory study of strongly correlated materials,” *Journal of Chemical Physics*, vol. 123, p. 014703, 2005.

[32] P. A. Korzhavyi, L. Vitos, D. A. Andersson, and B. Johansson, “Oxidation of plutonium dioxide,” *Nature Materials*, vol. 3, no. 4, pp. 225–228, 2004.

[33] S. D. Conradson, B. D. Begg, D. L. Clark, C. den Auwer, M. Ding, P. K. Dorhout, F. J. Espinosa-Faller, P. L. Gordon, R. G. Haire, N. J. Hess, R. F. Hess, D. W. Keogh, L. A. Morales, M. P. Neu, P. Paviet-Hartmann, W. Runde, C. D. Tait, D. K. Veirs, and P. M. Villella, “Local and Nanoscale Structure and Speciation in the $PuO_{2+x-y}(OH)_{2y}{\cdot}zH_2O$ System,” *Journal of the American Chemical Society*, vol. 126, no. 41, pp. 13443–13458, 2004.

[34] R. H. Penneman and M. T. Paffet, “Proposing a hydroxide ion, rather than a central oxide ion,” in *Actinide Research Quarterly*, no. 2nd Quarter, pp. 9–13, 2004.

[35] B. Ao, R. Qiu, H. Lu, X. Ye, P. Shi, P. Chen, and X. Wang, “New Insights into the Formation of Hyperstoichiometric Plutonium Oxides,” *The Journal of Physical Chemistry C*, vol. 119, no. 1, pp. 101–108, 2015.

[36] “Strategy options for the UK’s separated plutonium,” Tech. Rep. Policy document 24/07, The Royal Society, 2007.

[37] G. Bailey, E. Bluhm, J. Lyman, R. Mason, M. Paffett, G. Polansky, G. D. Roberson, M. Sherman, K. Veirs, and L. Worl, “Gas Generation from Actinide Oxide Materials,” Tech. Rep. LA-13781-MS, Los Alamos National Laboratory, Los Alamos, NM, 2000.

[38] L. A. Morales, J. M. Haschke, and T. H. Allen, “Kinetics of Reaction Between Plutonium Dioxide and Water at 25°C to 350°C: Formation and Properties of the PuO_{2+x} Phase,” Tech. Rep. LA-13597-MS, Los Alamos National Laboratory, Los Alamos, NM, 1999.

[39] “Annual Research and Development Review 2020/21,” tech. rep., Sellafield Ltd., 2021.

[40] H. E. Sims, K. J. Webb, J. Brown, D. Morris, and R. J. Taylor, “Hydrogen yields from water on the surface of plutonium dioxide,” *Journal of Nuclear Materials*, vol. 437, no. 1, pp. 359–364, 2013.

[41] “DOE Standard: Stabilization, Packaging, and Storage of Plutonium-Bearing Materials,” Tech. Rep. DOE-STD-3013-2018, U.S. Department of Energy, Washington, D.C., 2018.

[42] W. Kohn and L. J. Sham, “Self-Consistent Equations Including Exchange and Correlation Effects,” *Physical Review*, vol. 140, no. 4A, pp. A1133—-A1138, 1965.

[43] P. A. M. Dirac, “Note on Exchange Phenomena in the Thomas Atom,” *Mathematical Proceedings of the Cambridge Philosophical Society*, vol. 26, no. 3, pp. 376–385, 1930.

[44] D. M. Ceperley and B. J. Alder, “Ground State of the Electron Gas by a Stochastic Method,” *Physical Review Letters*, vol. 45, no. 7, pp. 566–569, 1980.

[45] S. H. Vosko, L. Wilk, and M. Nusair, “Accurate spin-dependent electron liquid correlation energies for local spin density calculations: a critical analysis,” *Canadian Journal of Physics*, vol. 58, no. 8, pp. 1200–1211, 1980.

[46] X. D. Wen, R. L. Martin, T. M. Henderson, and G. E. Scuseria, “Density functional theory studies of the electronic structure of solid state actinide oxides,” *Chemical Reviews*, vol. 113, pp. 1063–1096, 2013.

[47] A. J. Garza and G. E. Scuseria, “Predicting Band Gaps with Hybrid Density Functionals,” *The Journal of Physical Chemistry Letters*, vol. 7, no. 20, pp. 4165–4170, 2016.

[48] J. T. Pegg, A. E. Shields, M. T. Storr, A. S. Wills, D. O. Scanlon, and N. H. De Leeuw, “Hidden magnetic order in plutonium dioxide nuclear fuel,” *Physical Chemistry Chemical Physics*, vol. 492, pp. 269–278, 2018.

[49] J. T. Pegg, X. Aparicio-Anglès, M. Storr, and N. H. de Leeuw, “DFT+U study of the structures and properties of the actinide dioxides,” *Journal of Nuclear Materials*, vol. 492, pp. 269–278, 2017.

[50] A. I. Liechtenstein, V. I. Anisimov, and J. Zaanen, "Density-functional theory and strong interactions: Orbital ordering in Mott-Hubbard insulators," *Physical Review B*, vol. 52, pp. R5467–R5470, 1995.

[51] S. L. Dudarev, G. A. Botton, S. Y. Savrasov, C. J. Humphreys, and A. P. Sutton, "Electron-energy-loss spectra and the structural stability of nickel oxide: An LSDA+U study," *Physical Review B*, vol. 57, no. 3, pp. 1505–1509, 1998.

[52] P. S. Ghosh and A. Arya, "First-principles study of phase stability, electronic and mechanical properties of plutonium sub-oxides," *Physical Chemistry Chemical Physics*, vol. 21, pp. 16818–16829, 2019.

[53] H. Nakamura, M. Machida, and M. Kato, "LDA+U Study on Plutonium Dioxide with Spin-Orbit Couplings," *Progress in Nuclear Science and Technology*, vol. 2, pp. 16–19, 2011.

[54] P. Zhang, B. T. Wang, and X. G. Zhao, "Ground-state properties and high-pressure behavior of plutonium dioxide: Density functional theory calculations," *Physical Review B - Condensed Matter and Materials Physics*, vol. 82, pp. 1–14, 2010.

[55] B. Sun, P. Zhang, and X. G. Zhao, "First-principles local density approximation+U and generalized gradient approximation+U study of plutonium oxides," *Journal of Chemical Physics*, vol. 128, p. 084705, 2008.

[56] C. E. McNeilly, "The electrical properties of plutonium oxides," *Journal of Nuclear Materials*, vol. 11, pp. 53–58, 1964.

[57] T. Mark McCleskey, E. Bauer, Q. Jia, A. K. Burrell, B. L. Scott, S. D. Conradson, A. Mueller, L. Roy, X. Wen, G. E. Scuseria, and R. L. Martin, "Optical band gap of NpO_2 and PuO_2 from optical absorbance of epitaxial films," *Journal of Applied Physics*, vol. 113, p. 013515, 2013.

[58] P. Roussel, K. S. Graham, S. C. Hernandez, J. J. Joyce, A. J. Nelson, R. Sykes, T. Venhaus, and K. White, "Electronic and optical properties of plutonium metal and oxides from Reflection Electron Energy Loss Spectroscopy," *Applied Surface Science*, vol. 553, p. 149559, 2021.

[59] P. Roussel, "Inverse photoemission measurements of plutonium metal and oxides," *Journal of Electron Spectroscopy and Related Phenomena*, vol. 246, p. 147030, 2021.

[60] S. Grimme, "Density functional theory with London dispersion corrections," *WIREs Computational Molecular Science*, vol. 1, no. 2, pp. 211–228, 2011.

[61] S. Grimme, J. Antony, S. Ehrlich, and H. Krieg, "A consistent and accurate ab initio parametrization of density functional dispersion correction (DFT-D) for the 94 elements H-Pu," *The Journal of Chemical Physics*, vol. 132, no. 15, p. 154104, 2010.

[62] L. Goerigk, "A Comprehensive Overview of the DFT-D3 London-Dispersion Correction," in *Non-Covalent Interactions in Quantum Chemistry and Physics* (A. Otero de la Roza and G. A. DiLabio, eds.), pp. 195–219, Elsevier, 2017.

[63] H. J. Monkhorst and J. D. Pack, "Special points for Brillouin-zone integrations," *Physical Review B*, vol. 13, pp. 5188–5192, 1976.

[64] J. P. Perdew, K. Burke, and M. Ernzerhof, "Generalized Gradient Approximation Made Simple," *Physical Review Letters*, vol. 77, no. 18, pp. 3865–3868, 1996.

[65] J. P. Perdew, A. Ruzsinszky, G. I. Csonka, O. A. Vydrov, G. E. Scuseria, L. A. Constantin, X. Zhou, and K. Burke, "Restoring the Density-Gradient Expansion for Exchange in Solids and Surfaces," *Physical Review Letters*, vol. 100, no. 13, p. 136406, 2008.

[66] G. I. Csonka, J. P. Perdew, A. Ruzsinszky, P. H. T. Philipsen, S. Lebègue, J. Paier, O. A. Vydrov, and J. G. Ángyán, “Assessing the performance of recent density functionals for bulk solids,” *Physical Review B*, vol. 79, no. 15, p. 155107, 2009.

[67] G. Jomard, B. Amadon, F. m. ç. Bottin, and M. Torrent, “Structural, thermodynamic, and electronic properties of plutonium oxides from first principles,” *Physical Review B*, vol. 78, no. 7, p. 75125, 2008.

[68] B. Meredig, A. Thompson, H. A. Hansen, C. Wolverton, and A. van de Walle, “Method for locating low-energy solutions within DFT$+U$,” *Physical Review B*, vol. 82, no. 19, p. 195128, 2010.

[69] B. Dorado, B. Amadon, M. Freyss, and M. Bertolus, “DFT+U calculations of the ground state and metastable states of uranium dioxide,” *Physical Review B*, vol. 79, no. 23, p. 235125, 2009.

[70] G. Kresse and J. Hafner, “*Ab initio* molecular dynamics for liquid metals,” *Physical Review B*, vol. 47, pp. 558–561, 1993.

[71] G. Kresse and J. Hafner, “*Ab initio* molecular-dynamics simulation of the liquid-metal–amorphous-semiconductor transition in germanium,” *Physical Review B*, vol. 49, pp. 14251–14269, 1994.

[72] G. Kresse and J. Furthmüller, “Efficiency of *ab-initio* total energy calculations for metals and semiconductors using a plane-wave basis set,” *Computational Materials Science*, vol. 6, pp. 15–50, 1996.

[73] G. Kresse and J. Furthmüller, “Efficient iterative schemes for *ab initio* total-energy calculations using a plane-wave basis set,” *Physical Review B*, vol. 54, pp. 11169–11186, 1996.

[74] Y. Yang, Y. Lu, and P. Zhang, “Optical properties of PuO_2 and α-Pu_2O_3 by GGA+U+QA studies,” *Journal of Nuclear Materials*, vol. 452, no. 1, pp. 414–418, 2014.

[75] I. D. Prodan, G. E. Scuseria, and R. L. Martin, “Assessment of metageneralized gradient approximation and screened Coulomb hybrid density functionals on bulk actinide oxides,” *Physical Review B*, vol. 73, no. 4, p. 45104, 2006.

[76] Y. Tokunaga, H. Sakai, T. Fujimoto, S. Kambe, R. E. Walstedt, K. Ikushima, H. Yasuoka, D. Aoki, Y. Homma, Y. Haga, T. D. Matsuda, S. Ikeda, E. Yamamoto, A. Nakamura, Y. Shiokawa, K. Nakajima, Y. Arai, and Y. Ōnuki, “NMR studies of actinide dioxides,” *Journal of Alloys and Compounds*, vol. 444-445, pp. 241–245, 2007.

[77] J. T. Pegg, A. E. Shields, M. T. Storr, D. O. Scanlon, and N. H. de Leeuw, “Noncollinear Relativistic DFT + U Calculations of Actinide Dioxide Surfaces,” *The Journal of Physical Chemistry C*, vol. 123, no. 1, pp. 356–366, 2019.

[78] D. Gryaznov, S. Rashkeev, E. A. Kotomin, E. Heifets, and Y. Zhukovskii, “Helium behavior in oxide nuclear fuels: First principles modeling,” *Nuclear Instruments and Methods in Physics Research Section B: Beam Interactions with Materials and Atoms*, vol. 268, no. 19, pp. 3090–3094, 2010.

[79] Y. Lu, Y. Yang, and P. Zhang, “Charge states of point defects in plutonium oxide: A first-principles study,” *Journal of Alloys and Compounds*, vol. 649, pp. 544–552, 2015.

[80] S. C. Hernandez and E. F. Holby, “DFT+U Study of Chemical Impurities in PuO2,” *The Journal of Physical Chemistry C*, vol. 120, pp. 13095–13102, 2016.

[81] D. L. Clark, S. S. Hecker, G. D. Jarvinen, and M. P. Neu, *Plutonium*, pp. 813–1264. Dordrecht: Springer Netherlands, 2008.

[82] J. P. W. Wellington, A. Kerridge, J. Austin, and N. Kaltsoyannis, "Electronic structure of bulk AnO_2 (An = U, Np, Pu) and water adsorption on the (111) and (110) surfaces of UO_2 and PuO_2 from hybrid density functional theory within the periodic electrostatic embedded cluster method," *Journal of Nuclear Materials*, vol. 482, pp. 124–134, 2016.

[83] J.-L. Chen and N. Kaltsoyannis, "Hybrid functional/embedded cluster study of uranium and actinide (actinide = Np, Pu, Am or Cm) mixed dioxides bulk and $\{110\}$ surfaces," *Journal of Nuclear Materials*, vol. 560, p. 153490, 2022.

[84] M. T. Butterfield, T. Durakiewicz, E. Guziewicz, J. J. Joyce, A. J. Arko, K. S. Graham, D. P. Moore, and L. A. Morales, "Photoemission of surface oxides and hydrides of delta plutonium," *Surface Science*, vol. 571, no. 1, pp. 74–82, 2004.

[85] F. A. Kröger and H. J. Vink, "Relations between the Concentrations of Imperfections in Crystalline Solids," vol. 3 of *Solid State Physics*, pp. 307–435, Academic Press, 1956.

[86] M. W. Cooper, S. T. Murphy, and D. A. Andersson, "The defect chemistry of $UO_{2\pm x}$ from atomistic simulations," *Journal of Nuclear Materials*, vol. 504, pp. 251–260, 2018.

[87] A. Soulié, F. Bruneval, M.-C. Marinica, S. Murphy, and J.-P. Crocombette, "Influence of vibrational entropy on the concentrations of oxygen interstitial clusters and uranium vacancies in nonstoichiometric UO_2," *Physical Review Materials*, vol. 2, p. 083607, 2018.

[88] J.-P. Crocombette, D. Torumba, and A. Chartier, "Charge states of point defects in uranium oxide calculated with a local hybrid functional for correlated electrons," *Physical Review B*, vol. 83, no. 18, p. 184107, 2011.

[89] Y. Mishin, M. R. Sørensen, and A. F. Voter, "Calculation of point-defect entropy in metals," *Philosophical Magazine A*, vol. 81, pp. 2591–2612, 2001.

[90] D. A. Andersson, P. Garcia, X.-Y. Liu, G. Pastore, M. Tonks, P. Millett, B. Dorado, D. R. Gaston, D. Andrs, R. L. Williamson, R. C. Martineau, B. P. Uberuaga, and C. R. Stanek, "Atomistic modeling of intrinsic and radiation-enhanced fission gas (Xe) diffusion in $UO_{2\pm x}$: Implications for nuclear fuel performance modeling," *Journal of Nuclear Materials*, vol. 451, pp. 225–242, 2014.

[91] W. D. Neilson and S. T. Murphy, "DefAP: A Python code for the analysis of point defects in crystalline solids," *Computational Materials Science*, vol. 210, p. 111434, 2022.

[92] C. G. de Walle and A. Janotti, "Advances in electronic structure methods for defects and impurities in solids," *physica status solidi (b)*, vol. 248, no. 1, pp. 19–27, 2011.

[93] S. Kim, S. N. Hood, J.-S. Park, L. D. Whalley, and A. Walsh, "Quick-start guide for first-principles modelling of point defects in crystalline materials," *Journal of Physics: Energy*, vol. 2, no. 3, p. 36001, 2020.

[94] A. Goyal, P. Gorai, H. Peng, S. Lany, and V. Stevanović, "A computational framework for automation of point defect calculations," *Computational Materials Science*, vol. 130, pp. 1–9, 2017.

[95] D. Broberg, B. Medasani, N. E. R. Zimmermann, G. Yu, A. Canning, M. Haranczyk, M. Asta, and G. Hautier, "PyCDT: A Python toolkit for modeling point defects in semiconductors and insulators," *Computer Physics Communications*, vol. 226, pp. 165–179, 2018.

[96] M. Arrigoni and G. K. H. Madsen, "Spinney: Post-processing of first-principles calculations of point defects in semiconductors with Python," *Computer Physics Communications*, vol. 264, p. 107946, 2021.

[97] A. Stoliaroff, S. Jobic, and C. Latouche, "PyDEF 2.0: An Easy to Use Post-treatment Software for Publishable Charts Featuring a Graphical User Interface," *Journal of Computational Chemistry*, vol. 39, no. 26, pp. 2251–2261, 2018.

[98] J. Buckeridge, "Equilibrium point defect and charge carrier concentrations in a material determined through calculation of the self-consistent Fermi energy," *Computer Physics Communications*, vol. 244, pp. 329–342, 2019.

[99] M. Leslie and N. J. Gillan, "The energy and elastic dipole tensor of defects in ionic crystals calculated by the supercell method," *Journal of Physics C: Solid State Physics*, vol. 18, pp. 973–982, 1985.

[100] G. Makov and M. C. Payne, "Periodic boundary conditions in ab initio calculations," *Physical Review B*, vol. 51, no. 7, pp. 4014–4022, 1995.

[101] S. Lany and A. Zunger, "Assessment of correction methods for the band-gap problem and for finite-size effects in supercell defect calculations: Case studies for ZnO and GaAs," *Physical Review B*, vol. 78, no. 23, p. 235104, 2008.

[102] C. Freysoldt, J. Neugebauer, and C. G. Van de Walle, "Fully *Ab Initio* Finite-Size Corrections for Charged-Defect Supercell Calculations," *Physical Review Letters*, vol. 102, p. 016402, 2009.

[103] S. E. Taylor and F. Bruneval, "Understanding and correcting the spurious interactions in charged supercells," *Physical Review B*, vol. 84, no. 7, p. 75155, 2011.

[104] S. T. Murphy and N. D. M. Hine, "Anisotropic charge screening and supercell size convergence of defect formation energies," *Physical Review B*, vol. 87, no. 9, p. 94111, 2013.

[105] Y. Kumagai and F. Oba, "Electrostatics-based finite-size corrections for first-principles point defect calculations," *Physical Review B*, vol. 89, p. 195205, 2014.

[106] S. Kasamatsu, T. Tada, and S. Watanabe, "Theoretical analysis of space charge layer formation at metal/ionic conductor interfaces," *Solid State Ionics*, vol. 183, no. 1, pp. 20–25, 2011.

[107] M. W. Finnis, A. Y. Lozovoi, and A. Alavi, "The Oxidation Of NiAl: What Can We Learn from Ab Initio Calculations?," *Annual Review of Materials Research*, vol. 35, pp. 167–207, 2005.

[108] P. Linstrom and W. Mallard, eds., *NIST Chemistry WebBook, NIST Standard Reference Database Number 69*.

[109] K. Johnston, M. R. Castell, A. T. Paxton, and M. W. Finnis, "$SrTiO_3$ (001) (2×1) reconstructions: First-principles calculations of surface energy and atomic structure compared with scanning tunneling microscopy images," *Physical Review B*, vol. 70, p. 085415, 2004.

[110] T. R. Durrant, S. T. Murphy, M. B. Watkins, and A. L. Shluger, "Relation between image charge and potential alignment corrections for charged defects in periodic boundary conditions," *The Journal of Chemical Physics*, vol. 149, p. 024103, 2018.

[111] M. A. Green, "Intrinsic concentration, effective densities of states, and effective mass in silicon," *Journal of Applied Physics*, vol. 67, no. 6, pp. 2944–2954, 1990.

[112] S. M. Sze, *Physics of semiconductor devices*. Wiley-Interscience, 3rd ed. ed., 2007.

[113] S. A. Centoni, B. Sadigh, G. H. Gilmer, T. J. Lenosky, T. de la Rubia, and C. B. Musgrave, “First-principles calculation of intrinsic defect formation volumes in silicon,” *Physical Review B*, vol. 72, no. 19, p. 195206, 2005.

[114] S. T. Murphy, “A point defect model for $YBa_2Cu_3O_7$ from density functional theory,” *Journal of Physics Communications*, vol. 4, no. 11, p. 115003, 2020.

[115] S. T. Murphy and N. D. M. Hine, “Point Defects and Non-stoichiometry in Li_2TiO_3,” *Chemistry of Materials*, vol. 26, pp. 1629–1638, 2014.

[116] S. T. Murphy, “Mechanisms of helium accommodation in lithium metatitanate,” *Fusion Engineering and Design*, vol. 101, pp. 94–100, 2015.

[117] W. D. Neilson, J. T. Pegg, H. Steele, and S. T. Murphy, “The defect chemistry of non-stoichiometric $PuO_{2\pm x}$,” *Physical Chemistry Chemical Physics*, vol. 23, no. 8, pp. 4544–4554, 2021.

[118] L.-F. Wang, B. Sun, H.-F. Liu, D.-Y. Lin, and H.-F. Song, “Thermodynamics and kinetics of intrinsic point defects in plutonium dioxides,” *Journal of Nuclear Materials*, vol. 526, p. 151762, 2019.

[119] M. S. D. Read, S. R. Walker, and R. A. Jackson, “Derivation of enhanced potentials for plutonium dioxide and the calculation of lattice and intrinsic defect properties,” *Journal of Nuclear Materials*, vol. 448, no. 1, pp. 20–25, 2014.

[120] H. Nakamura and M. Machida, “A first-principles study on point defects in plutonium dioxide,” *Progress in Nuclear Science and Technology*, pp. 132–135, 2018.

[121] X. Tian, T. Gao, C. Lu, J. Shang, and H. Xiao, “First principle study of the behavior of helium in plutonium dioxide,” *The European Physical Journal B*, vol. 86, no. 4, p. 179, 2013.

[122] P. Tiwary, A. van de Walle, B. Jeon, and N. Gr-Jensen, “Interatomic potentials for mixed oxide and advanced nuclear fuels,” *Physical Review B*, vol. 83, no. 9, p. 94104, 2011.

[123] M. Stan and P. Cristea, “Defects and oxygen diffusion in PuO_{2x},” *Journal of Nuclear Materials*, vol. 344, no. 1, pp. 213–218, 2005.

[124] M. Kato, H. Nakamura, M. Watanabe, T. Matsumoto, and M. Machida, “Defect chemistry and basic properties of non-stoichiometric PuO_2,” in *Defect and Diffusion Forum*, vol. 375, pp. 57–70, Trans Tech Publ, 2017.

[125] P. E. Blöchl, “Projector augmented-wave method,” *Physical Review B*, vol. 50, pp. 17953–17979, 1994.

[126] G. Kresse and D. Joubert, “From ultrasoft pseudopotentials to the projector augmented-wave method,” *Physical Review B*, vol. 59, pp. 1758–1775, 1999.

[127] S. Steiner, S. Khmelevskyi, M. Marsmann, and G. Kresse, “Calculation of the magnetic anisotropy with projected-augmented-wave methodology and the case study of disordered $Fe_{1-x}Co_x$ alloys,” *Physical Review B*, vol. 93, p. 224425, 2016.

[128] J. Heyd, G. E. Scuseria, and M. Ernzerhof, “Hybrid functionals based on a screened Coulomb potential,” *The Journal of Chemical Physics*, vol. 118, no. 18, pp. 8207–8215, 2003.

[129] J. Heyd and G. E. Scuseria, “Efficient hybrid density functional calculations in solids: Assessment of the Heyd–Scuseria–Ernzerhof screened

Coulomb hybrid functional," *The Journal of Chemical Physics*, vol. 121, no. 3, pp. 1187–1192, 2004.

[130] J. Heyd, G. E. Scuseria, and M. Ernzerhof, "Hybrid functionals based on a screened Coulomb potential," *The Journal of Chemical Physics*, vol. 118, no. 18, pp. 8207–8215, 2003.

[131] A. V. Krukau, O. A. Vydrov, A. F. Izmaylov, and G. E. Scuseria, "Influence of the exchange screening parameter on the performance of screened hybrid functionals," *The Journal of Chemical Physics*, vol. 125, no. 22, p. 224106, 2006.

[132] A. B. Shick, J. Kolorenč, L. Havela, T. Gouder, and R. Caciuffo, "Nonmagnetic ground state of PuO_2," *Physical Review B*, vol. 89, no. 4, p. 41109, 2014.

[133] J. M. Haschke and T. H. Allen, "Equilibrium and thermodynamic properties of the PuO_{2+x} solid solution," *Journal of Alloys and Compounds*, vol. 336, pp. 124–131, 2002.

[134] J. D. Gale, "GULP: A computer program for the symmetry-adapted simulation of solids," *Journal of the Chemical Society, Faraday Transactions*, vol. 93, pp. 629–637, 1997.

[135] M. W. D. Cooper, M. J. D. Rushton, and R. W. Grimes, "A many-body potential approach to modelling the thermomechanical properties of actinide oxides," *Journal of Physics: Condensed Matter*, vol. 26, p. 105401, 2014.

[136] M. W. D. Cooper, S. T. Murphy, M. J. D. Rushton, and R. W. Grimes, "Thermophysical properties and oxygen transport in the $(U_x,Pu_{1-x})O_2$ lattice," *Journal of Nuclear Materials*, vol. 461, pp. 206–214, 2015.

[137] M. E. Manley, J. R. Jeffries, A. H. Said, C. A. Marianetti, H. Cynn, B. M. Leu, and M. A. Wall, "Measurement of the phonon density of states of PuO_2

(+2% Ga): A critical test of theory," *Physical Review B*, vol. 85, p. 132301, 2012.

[138] L. Manes and A. Barisich, "Dielectric Response and Infrared Spectrum of Stoichiometric Plutonium Dioxide by Optical Reflection and Absorption Spectroscopy," *physica status solidi (a)*, vol. 3, no. 4, pp. 971–981, 1970.

[139] N. Hampton, G. A. Saunders, J. H. Harding, and A. M. Stoneham, "The dielectric constant of UO_2 below the Ne´el point," *Journal of Nuclear Materials*, vol. 149, no. 1, pp. 18–20, 1987.

[140] M. S. Talla Noutack, G. Geneste, G. Jomard, and M. Freyss, "First-principles investigation of the bulk properties of americium dioxide and sesquioxides," *Physical Review Materials*, vol. 3, p. 35001, 2019.

[141] H.-P. Komsa, T. T. Rantala, and A. Pasquarello, "Finite-size supercell correction schemes for charged defect calculations," *Physical Review B*, vol. 86, no. 4, p. 45112, 2012.

[142] P. Söderlind, A. Landa, and B. Sadigh, "Density-functional theory for plutonium," *Advances in Physics*, vol. 68, pp. 1–47, 2019.

[143] G. K. Johnson, E. H. Van Deventer, O. L. Kruger, and W. N. Hubbard, "The enthalpies of formation of plutonium dioxide and plutonium mononitride," *The Journal of Chemical Thermodynamics*, vol. 1, pp. 89–98, 1969.

[144] G. E. Murch and C. R. A. Catlow, "Oxygen diffusion in UO_2, ThO_2 and PuO_2. A review," *Journal of the Chemical Society, Faraday Transactions 2: Molecular and Chemical Physics*, vol. 83, no. 7, pp. 1157–1169, 1987.

[145] C. Guéneau, C. Chatillon, and B. Sundman, "Thermodynamic modelling of the plutonium–oxygen system," *Journal of Nuclear Materials*, vol. 378, no. 3, pp. 257–272, 2008.

[146] W. D. Neilson, H. Steele, and S. T. Murphy, “Evolving Defect Chemistry of (Pu,Am)$O_{2\pm x}$,” *The Journal of Physical Chemistry C*, vol. 125, no. 28, pp. 15560–15568, 2021.

[147] V. Peterson, “Reference computations of public dose and cancer risk from airborne releases of plutonium. Nuclear safety technical report,” Tech. Rep. RFP–4910, EG and G Rocky Flats, Inc., Golden, CO, 1993.

[148] J. L. Chen and N. Kaltsoyannis, “Computational Study of Plutonium-Americium Mixed Oxides ($Pu_{0.92}Am_{0.08}O_{2-x}$); Water Adsorption on {111}, {110}, and {100} Surfaces,” *Journal of Physical Chemistry C*, vol. 124, pp. 6646–6658, 2020.

[149] M. Osaka, K. Kurosaki, and S. Yamanaka, “Oxygen potential of ($Pu_{0.91}Am_{0.09}$)O_{2-x},” *Journal of Nuclear Materials*, vol. 357, pp. 69–76, 2006.

[150] T. Matsumoto, T. Arima, Y. Inagaki, K. Idemitsu, M. Kato, K. Morimoto, and T. Sunaoshi, “Oxygen potential measurement of ($Pu_{0.928}Am_{0.072}$)O_{2-x} at high temperatures,” *Journal of Nuclear Science and Technology*, vol. 52, pp. 1296–1302, 2015.

[151] R. C. Belin, P. M. Martin, J. Lechelle, M. Reynaud, and A. C. Scheinost, “Role of cation interactions in the reduction process in plutonium-americium mixed oxides,” *Inorganic Chemistry*, vol. 52, pp. 2966–2972, 2013.

[152] H. P. Emerson, C. I. Pearce, C. H. Delegard, K. J. Cantrell, M. M. V. Snyder, M.-L. Thomas, B. N. Gartman, M. D. Miller, C. T. Resch, S. M. Heald, A. E. Plymale, D. D. Reilly, S. A. Saslow, W. Neilson, S. Murphy, M. Zavarin, A. B. Kersting, and V. L. Freedman, “Influences on Subsurface Plutonium and Americium Migration,” *ACS Earth and Space Chemistry*, vol. 5, no. 2, pp. 279–294, 2021.

[153] K. J. Cantrell and A. R. Felmy, "Plutonium and Americium Geochemistry at Hanford: A Site Wide Review," Tech. Rep. PNNL-21651, Pacific Northwest National Lab. (PNNL), Richland, WA, 2012.

[154] D. Taylor, "Thermal expansion data," *Transactions and Journal of the British Ceramic Society*, vol. 83, pp. 32–37, 1984.

[155] C. Suzuki, T. Nishi, M. Nakada, M. Akabori, M. Hirata, and Y. Kaji, "Core-hole effect on XANES and electronic structure of minor actinide dioxides with fluorite structure," *Journal of Physics and Chemistry of Solids*, vol. 73, pp. 209–216, 2012.

[156] T. D. Chikalla and L. Eyring, "Phase relationships in the americium-oxygen system," *Journal of Inorganic and Nuclear Chemistry*, vol. 30, pp. 133–145, 1968.

[157] G. Henkelman, A. Arnaldsson, and H. Jónsson, "A fast and robust algorithm for Bader decomposition of charge density," *Computational Materials Science*, vol. 36, pp. 354–360, 2006.

[158] R. D. Shannon, "Revised effective ionic radii and systematic studies of interatomic distances in halides and chalcogenides," *Acta Crystallographica Section A*, vol. 32, no. 5, pp. 751–767, 1976.

[159] E. Epifano, D. Prieur, P. M. Martin, C. Guéneau, K. Dardenne, J. Rothe, T. Vitova, O. Dieste, T. Wiss, R. J. M. Konings, and D. Manara, "Melting behaviour of uranium-americium mixed oxides under different atmospheres," *The Journal of Chemical Thermodynamics*, vol. 140, p. 105896, 2020.

[160] W. D. Neilson, H. Steele, N. Kaltsoyannis, and S. T. Murphy, "Accommodation of helium in $PuO_{2\pm x}$ and the role of americium," *Physical Chemistry Chemical Physics*, vol. 24, no. 14, pp. 8245–8250, 2022.

[161] T. Wiss, J.-P. Hiernaut, D. Roudil, J.-Y. Colle, E. Maugeri, Z. Talip, A. Janssen, V. Rondinella, R. J. M. Konings, H.-J. Matzke, and W. J. Weber, "Evolution of spent nuclear fuel in dry storage conditions for millennia and beyond," *Journal of Nuclear Materials*, vol. 451, no. 1, pp. 198–206, 2014.

[162] M. S. El-Genk and J.-M. Tournier, "Estimates of helium gas release in $^{238}PuO_2$ fuel particles for radioisotope heat sources and heater units," *Journal of Nuclear Materials*, vol. 280, no. 1, pp. 1–17, 2000.

[163] C. Ronchi and J. P. Hiernaut, "Helium diffusion in uranium and plutonium oxides," *Journal of Nuclear Materials*, vol. 325, no. 1, pp. 1–12, 2004.

[164] R. Mulford, "Helium Transport in PuO2 as a Function of Temperature and Heating Rate," in *INMM 55th Annual Meeting*, no. LA-UR-25325, (Los Alamos National Laboratory, Los Alamos, NM), 2014.

[165] M. Freyss, N. Vergnet, and T. Petit, "Ab initio modeling of the behavior of helium and xenon in actinide dioxide nuclear fuels," *Journal of Nuclear Materials*, vol. 352, no. 1, pp. 144–150, 2006.

[166] M. Freyss and T. Petit, "Ab initio modelling of the behaviour of helium in americium and plutonium oxides," Tech. Rep. INIS-FR–3001, CEA-Cadarache, 13108 Saint-Paul-lez-Durance, France, 2004.

[167] B. A. Powell, Z. Dai, M. Zavarin, P. Zhao, and A. B. Kersting, "Stabilization of Plutonium Nano-Colloids by Epitaxial Distortion on Mineral Surfaces," *Environmental Science Technology*, vol. 45, no. 7, pp. 2698–2703, 2011.

[168] A. Y. Romanchuk, S. N. Kalmykov, A. V. Egorov, Y. V. Zubavichus, A. A. Shiryaev, O. N. Batuk, S. D. Conradson, D. A. Pankratov, and I. A. Presnyakov, "Formation of crystalline $PuO_{2+x}{\cdot}nH_2O$ nanoparticles upon sorption of Pu(V,VI) onto hematite," *Geochimica et Cosmochimica Acta*, vol. 121, pp. 29–40, 2013.

[169] A. Y. Romanchuk, T. V. Plakhova, A. V. Egorov, T. B. Egorova, P. V. Dorovatovskii, Y. V. Zubavichus, A. A. Shiryaev, and S. N. Kalmykov, “Redox-mediated formation of plutonium oxide nanoparticles,” *Dalton Transactions*, vol. 47, no. 32, pp. 11239–11244, 2018.

[170] E. Gerber, A. Y. Romanchuk, I. Pidchenko, L. Amidani, A. Rossberg, C. Hennig, G. B. M. Vaughan, A. Trigub, T. Egorova, S. Bauters, T. Plakhova, M. O. J. Y. Hunault, S. Weiss, S. M. Butorin, A. C. Scheinost, S. N. Kalmykov, and K. O. Kvashnina, “The missing pieces of the PuO_2 nanoparticle puzzle,” *Nanoscale*, vol. 12, no. 35, pp. 18039–18048, 2020.

[171] L. Bonato, M. Virot, T. Dumas, A. Mesbah, E. Dalodière, O. Dieste Blanco, T. Wiss, X. Le Goff, M. Odorico, D. Prieur, A. Rossberg, L. Venault, N. Dacheux, P. Moisy, and S. I. Nikitenko, “Probing the local structure of nanoscale actinide oxides: a comparison between PuO_2 and ThO_2 nanoparticles rules out PuO_{2+x} hypothesis,” *Nanoscale Advances*, vol. 2, no. 1, pp. 214–224, 2020.

[172] C. Micheau, M. Virot, S. Dourdain, T. Dumas, D. Menut, P. L. Solari, L. Venault, O. Diat, P. Moisy, and S. I. Nikitenko, “Relevance of formation conditions to the size, morphology and local structure of intrinsic plutonium colloids,” *Environmental Science: Nano*, vol. 7, no. 8, pp. 2252–2266, 2020.

[173] S. Moxon, A. R. Symington, J. S. Tse, J. Dawson, J. M. Flitcroft, S. C. Parker, D. J. Cooke, R. M. Harker, and M. Molinari, “The energetics of carbonated PuO_2 surfaces affects nanoparticle morphology: a DFT+U study,” *Physical Chemistry Chemical Physics*, vol. 22, no. 15, pp. 7728–7737, 2020.

[174] G. Jomard and F. Bottin, “Thermodynamic stability of PuO_2 surfaces: Influence of electronic correlations,” *Physical Review B*, vol. 84, no. 19, p. 195469, 2011.

[175] B. Sun, H. Liu, H. Song, G. Zhang, H. Zheng, X. Zhao, and P. Zhang, “First-principles study of surface properties of PuO_2: Effects of thickness and O-vacancy on surface stability and chemical activity,” *Journal of Nuclear Materials*, vol. 426, no. 1, pp. 139–147, 2012.

[176] D. Selli, G. Fazio, and C. Di Valentin, “Using Density Functional Theory to Model Realistic TiO_2 Nanoparticles, Their Photoactivation and Interaction with Water,” *Catalysts*, vol. 7, no. 12, 2017.

[177] A. R. Puigdollers, F. Illas, and G. Pacchioni, “Structure and Properties of Zirconia Nanoparticles from Density Functional Theory Calculations,” *The Journal of Physical Chemistry C*, vol. 120, no. 8, pp. 4392–4402, 2016.

[178] A. Walsh, A. A. Sokol, J. Buckeridge, D. O. Scanlon, and C. R. A. Catlow, “Oxidation states and ionicity,” *Nature Materials*, vol. 17, no. 11, pp. 958–964, 2018.

[179] X. Huang and M. J. Beck, “Surface structure of catalytically-active ceria nanoparticles,” *Computational Materials Science*, vol. 91, pp. 122–133, 2014.

[180] E. Dalodière, M. Virot, V. Morosini, T. Chave, T. Dumas, C. Hennig, T. Wiss, O. Dieste Blanco, D. K. Shuh, T. Tyliszcak, L. Venault, P. Moisy, and S. I. Nikitenko, “Insights into the sonochemical synthesis and properties of salt-free intrinsic plutonium colloids,” *Scientific Reports*, vol. 7, no. 1, p. 43514, 2017.

[181] D. Prieur, W. Bonani, K. Popa, O. Walter, K. W. Kriegsman, M. H. Engelhard, X. Guo, R. Eloirdi, T. Gouder, A. Beck, T. Vitova, A. C. Scheinost, K. Kvashnina, and P. Martin, “Size Dependence of Lattice Parameter and Electronic Structure in CeO_2 Nanoparticles,” *Inorganic Chemistry*, vol. 59, no. 8, pp. 5760–5767, 2020.

[182] S. Tsunekawa, K. Ishikawa, Z.-Q. Li, Y. Kawazoe, and A. Kasuya, "Origin of Anomalous Lattice Expansion in Oxide Nanoparticles," *Physical Review Letters*, vol. 85, no. 16, pp. 3440–3443, 2000.

[183] L. Chen, T. Mashimo, E. Omurzak, H. Okudera, C. Iwamoto, and A. Yoshiasa, "Pure Tetragonal ZrO_2 Nanoparticles Synthesized by Pulsed Plasma in Liquid," *The Journal of Physical Chemistry C*, vol. 115, no. 19, pp. 9370–9375, 2011.

[184] S. Monticone, R. Tufeu, A. V. Kanaev, E. Scolan, and C. Sanchez, "Quantum size effect in TiO_2 nanoparticles: does it exist?," *Applied Surface Science*, vol. 162-163, pp. 565–570, 2000.

[185] J. Rothe, C. Walther, M. A. Denecke, and T. Fanghänel, "XAFS and LIBD Investigation of the Formation and Structure of Colloidal Pu(IV) Hydrolysis Products," *Inorganic Chemistry*, vol. 43, no. 15, pp. 4708–4718, 2004.

[186] L. Morales, "The path to PuO_{2+x}," in *Actinide Research Quarterly*, pp. 3–8, 2004.

Appendix A

DFT simulation parameters for Si, $YBa_2Cu_3O_7$ and Li_2TiO_3

Table A.1: DFT parameters for simulated systems

	Si	$YBa_2Cu_3O_7$	Li_2TiO_3
Simulation package	VASP	CASTEP	CASTEP
Exchange correlation functional	PBE	PBE	PBE
Pseudopotential	Projector augmented wave	Ultra-soft	Ultra-soft

Valence electrons	Si : 3s, 3p P : 3s, 3p	Y : 4s, 4p, 5s, 4d Ba : 5s, 5p, 6s Cu : 3d, 4s O : 2s, 2p	Li : 1s, 2s Ti : 3s, 3p, 4s O : 2s, 2p
Supercell size	$3 \times 3 \times 3$ (216 atoms)	$4 \times 4 \times 1$ (208 atoms)	$2 \times 2 \times 2$ (384 atoms)
k-point grid	$2 \times 2 \times 2$	$4 \times 4 \times 1$	$2 \times 1 \times 1$
Cutoff energy	500 eV	600 eV	550 eV
Convergence criteria	0.01 eV Å^{-1}	0.01 eV Å^{-1}	0.08 eV Å^{-1}

Appendix B

Nanoparticle's magnetic configuration testing

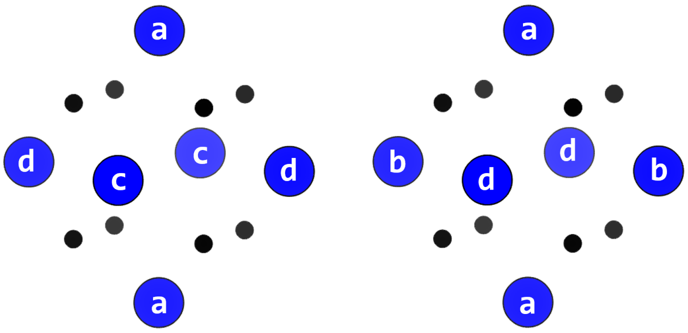
Longitudinal 3k AFM:

Transverse 3k AFM:

Atom	μ
1	(1, 1, 1)
2	(-1, -1, 1)
3	(-1, 1, -1)
4	(1, -1, -1)

Figure B.1: Key for Table B.1.

Table B.1: The relative energy (eV per atom) for non-collinear 3k antiferromagnetic magnetic configurations assigned to $Pu_{44}O_{80}$, differing based upon domain and the initial effective magnetic moment assignment (see Figure B.1), calculated with PBEsol + U (U = 6 eV).

Magnetic configuration	Atom assignment (See figure 1)				Relative energy
	a	b	c	d	
Longitudinal	1	2	4	3	0.001
	2	1	3	4	0.000
	3	4	2	1	0.027
	4	3	1	2	0.002
Transverse	1	2	4	3	0.028
	2	1	3	4	0.004
	3	4	2	1	0.013
	4	3	1	2	0.018